STANFORD UNIVERSITY

Guidance and Control Laboratory

PRECISION TETHERED SATELLITE ATTITUDE CONTROL

Final Report for NCC 2-389

A DISSERTATION
SUBMITTED TO THE DEPARTMENT OF MECHANICAL ENGINEERING
AND THE COMMITTEE ON GRADUATE STUDIES
OF STANFORD UNIVERSITY
IN PARTIAL FULFILLMENT OF THE REQUIREMENTS
FOR THE DEGREE OF
DOCTOR OF PHILOSOPHY

By
Robert J. Kline-Schoder
March 1990

This research was supported under Grant NCC 2-389

PRECISION TETHERED SATELLITE ATTITUDE CONTROL

A DISSERTATION
SUBMITTED TO THE DEPARTMENT OF MECHANICAL ENGINEERING
AND THE COMMITTEE ON GRADUATE STUDIES
OF STANFORD UNIVERSITY
IN PARTIAL FULFILLMENT OF THE REQUIREMENTS
FOR THE DEGREE OF
DOCTOR OF PHILOSOPHY

By
Robert J. Kline-Schoder
March 1990

Abstract

Tethered spacecraft possess unique dynamic characteristics which make them advantageous for certain classes of experiments. One use for which tethers are particularly well suited is to provide an isolated platform for space-borne observatories. The advantages of tethering a pointing platform 1 or 2 km from a space shuttle or space station are that, compared to placing the observatory on the parent spacecraft, vibrational disturbances are attenuated and contamination is eliminated.

In practice, all satellites have some requirement on the attitude control of the spacecraft, and tethered satellites are no exception. It has previously been shown that conventional means of performing attitude control for tethered satellites are insufficient for any mission with pointing requirements more stringent than about 1 deg. This is due mainly to the relatively large force applied by the tether to the spacecraft. A particularly effective method of implementing attitude control for tethered satellites is to use this tether tension force to generate control torques by moving the tether attach point relative to the sub-satellite center of mass. A demonstration of this attitude control technique on an astrophysical pointing platform has been proposed for a Space Shuttle flight test project and is referred to as the Kinetic Isolation Tether Experiment (KITE).

The current work is concerned with the theoretical development of both a large angle slew and long term, precision pointing control algorithm for tethered satellites, and the simulation of the KITE mission in an Earth laboratory environment. To that end, a scaled, one-dimensional, air-bearing supported laboratory simulator of the KITE satellite configuration has been constructed and is described in detail. The system equations are derived and a suitable control law is described. The precision

control algorithm consists of a Linear Quadratic Gaussian, full-state feedback control law in conjunction with a multi-variable Kalman filter. The control algorithm has been shown to regulate the vehicle orientation to within 0.60 arcsec RMS. This level of precision was achieved only after including a mass center estimator and accurately modeling the effects that the nonlinear actuator added to the system model.

In addition, a tether dynamics simulator has been constructed in order to implement the natural dynamic behavior of a 2 km long tether in the earth laboratory environment. The tether simulator is used to test the ability of the control algorithm to regulate the air-bearing vehicle orientation in the presence of variations in the tether tension magnitude and direction. Results of experiments show that, for the level of variation in tension magnitude and direction expected on orbit, neither longitudinal nor in-plane lateral tether dynamics will prevent the control algorithm from achieving long term, precision attitude control on the order of 1 arcsec.

Acknowledgements

The completion of this dissertation marks the end of my career as a student. My years in student life have been fruitful, thanks to the labor and dedication of numerous individuals, whose efforts I'd like to take this opportunity to acknowledge.

I will begin by thanking my principal advisor, Prof. J. David Powell. His guidance and advice through my years as a Ph. D. student served both to broaden my technical background and to build self confidence in my technical ability. Without his efforts, much of my work would have gone unrecognized. Secondly, I must thank Mr. Lawrence Lemke of NASA Ames Research Center. He has been instrumental in the development of technologies associated with tethered satellites and has been the sole source of funding for my work, as well as the source of the original concept to generate control torques by varying the sub-satellite tether attach point. Without him, this dissertation would not exist. In addition, I would like to thank the second and third readers of this dissertation, Professors Daniel DeBra and Thomas Kane. While reading graduate student dissertations is not the most exciting part of being a professor, their comments and suggestions have been extremely worthwhile and have significantly improved the documentation of my work.

When building a hardware experiment, having the necessary resources to facilitate the design and construction are of utmost importance. To that end, Stanford University and its graduate student population deserve great thanks. In particular, Mr. Russ Hacker deserves credit for the mechanical design of many of the component parts which went into the assembly of the air-bearing vehicle used in my work. Former graduate student and now Prof. Harold Alexander and fellow graduate student Mr.

Marc Ullman were instrumental in the development of the distributed computer system used to implement the control on the vehicle. Also, fellow graduate student, Mr. Xiaohua He, through numerous conversations, has aided in the development of some of the theory used in my work and through his own work, provided the justification for some of the experiments I ran with the laboratory simulator.

When undertaking a long and sometimes difficult task, those people closest to you tend to provide support in ways which are not always acknowledged and sometimes taken for granted. In light of this, I'd like to thank my wife, Barbara, for all of her moral support over the years of my graduate education. Without her understanding, confidence in me, and sense of shared purpose, I would have not been able to dedicate the time and effort necessary to complete my work. Finally, I thank my parents. Without their trust and sacrifice, my education would have been unthinkable. I dedicate this dissertation to them.

Contents

List of Tables

List of Figures

Chapter 1

Introduction

The generic problem of the precision orientation control of space-borne objects has been the concern of mission planners and engineers since the dawn of the space-age. Practically all space missions have some attitude control specification associated with the desired mission design. Whether the entire space vehicle or simply a sub-system (e.g., a camera or antenna) is of interest, the angular orientation of the constellation must be regulated. In some instances, small angular tolerances are required in order to achieve the desired mission. Over the years, a vast body of knowledge has been accumulated which sufficiently solves the attitude control problem for conventional spacecraft. As new, more complex, and less conventional satellite designs are explored for their potential uses, new methods of performing the orientation control for these new satellites must be developed. For new satellite designs, the conventional attitude control methods can become too costly, too heavy, or too inefficient to implement in an effective manner.

Tethered satellites are an excellent example of a potentially more complex, less conventional satellite design. A tethered satellite constellation consists of two distinct satellites (end masses) connected by a long (1-100 km), flexible cable (or tether). The very long tether is responsible for unique dynamic characteristics which make tethered satellites advantageous for certain classes of experiments. One use for which tethers are particularly well suited is to provide an isolated platform for space-borne

observatories. Typical space-based observatories will require a significant level of orientation regulation. Previous authors have described a concept to generate attitude control torques by varying the attachment of the tether on the sub-satellite. The purpose of the current research is to construct a laboratory simulator (using components similar to those expected in an orbital application) to test the control concept, and to determine the effect variations of mission requirements, linearity assumptions, and parameter variations will have on the ultimate performance of a tethered satellite attitude control system based on a movable tether attach point.

The following sections will provide a detailed description of tethered satellites and their proposed uses, the detailed discussion of the attitude control problem for a tethered, space-based observatory, a summary of previous work with related results, a description of the contributions the current research adds to the body of knowledge for tethered spacecraft, and a brief reader's guide to summarize the following chapters.

1.1 Description of Tethered Satellites

The basic concept of a tethered satellite is close to 100 years old. In 1895, Tsiolkovsky, a Russian scientist, first proposed a tower at Earth's equator which would reach beyond geo-synchronous orbit [1]. The purpose of the proposed tower was to provide access to a weightless environment. This "Jack-in-the-Beanstalk" concept remained relatively untouched until about 25 years ago when Sutton and Diederich [2] performed a simple analysis of the required cable mass and strength to connect one orbiting satellite above synchronous altitude and one orbiting satellite below synchronous altitude. This concept is the fundamental configuration of most modern tethered satellite constellations (except for the synchronous altitude requirement). The configuration consists of two end masses (i.e., satellites) connected with a long (1-100 km), flexible cable. The nominal configuration is such that the tether is aligned with the local vertical direction for the orbiting system. In this orientation, the configuration is nominally stable due to gravity gradient forces. The gravity gradient forces manifest themselves as a relative acceleration away from the mass center of the combined system of the two end masses. Since the tether is holding the two end masses

together, tension force is generated in the tether. This configuration and dynamic environment is the basis for many of the proposed uses of tethered spacecraft.

The advantages of and proposed uses for satellites tethered from the Space Shuttle and Space Station have been well documented by Bekey [3][4]. The advantages of using tethered satellites arise from the unique dynamic characteristics associated with their deployed configuration (e.g., the micro-gravity acceleration experienced on each end mass, the tension in the tether, and the station-keeping gravity gradient forces). The list of proposed uses includes:

- micro-gravity experiments,
- momentum transfer,
- electrodynamic conversion of energy,
- upper atmospheric research, and
- astrophysical pointing platforms.

Micro-gravity experiments can be performed relatively easily because of the micro-gravity acceleration experienced by each of the end masses. The level of gravitational field can be adjusted by varying the tether length or by crawling from one end mass to the other along the tether. The possibility of momentum transfer arises due to the fact that the upper end mass experiences a greater centrifugal than gravitational force and the lower mass experiences a greater gravitational than centrifugal force. The tether acts to hold the end masses in (relatively) close proximity and if the tether would be cut, the upper mass would be boosted to a higher energy elliptic orbit and the lower mass would be transferred to a lower energy elliptic orbit. Tether electrodynamics arise when conducting material is used as the tether. The interaction of the conducting tether with the Earth's magnetic field can generate electricity or thrust for the tethered satellite. Upper atmospheric research can be easily conducted with tethered satellites by placing the upper end mass in a 'normal' orbit and placing the lower end mass in an orbit which penetrates the upper reaches of the Earth's atmosphere (which is currently accessible only for short periods of time with sounding

rockets). Finally, tethered satellites are well suited to serve as astrophysical pointing platforms because the tether provides vibration and contamination isolation from the parent spacecraft, while maintaining a relatively close working proximity. In addition, the (relatively) lightweight configuration of tethered spacecraft can be exploited to generate artificial gravity. For man to spend long periods of time in a weightless environment, it is generally agreed that some form of artificial gravity will be necessary. Connecting two end modules with a long tether and spinning the system currently affords the most promising method to implement an artificial gravity spacecraft.

All of the above proposed uses of tethered satellites will have some requirement on the attitude control of the end masses. Due to the high stability requirements, the astrophysical pointing platform likely presents the smallest attitude control tolerances from the list of the proposed uses. As a result, it will serve as the motivating application for the design of a precision attitude control algorithm and laboratory simulator, both of which are the focus of this dissertation.

1.2 Astrophysical Observatory Control Problem

Recently, much interest has been shown in the concept of tethering space-borne observatories from the Space Shuttle or Space Station. The basic concept of tethering astrophysical pointing platforms is presented by Lemke [5]. He qualitatively discusses the fact that tethered observatories will provide contamination isolation from the parent spacecraft and quantitatively designs a closed-loop attitude control system and comments to the effectiveness of the vibration isolation provided by a typical tether. The control algorithm he suggests makes use of a variable position tether attach point in order to generate control torques. He also discusses a proposed Space Shuttle flight test mission, called the Kinetic Isolation Tether Experiment (KITE), and presents a preliminary design and mission plan.

In order to determine the exact level of orientation control necessary for an astrophysical observatory, Lemke, Powell, and He [6] present an analysis of these requirements for a typical 1 m class astrophysical pointing platform. Based on optical stability requirements, they determine that such a mission would require orientation

control on the order of 1 arcsec. They also provide an analysis of different methods to generate control torques and conclude that in order to achieve orientation control on the order of 1 arcsec for a tethered satellite, conventional means are insufficient and the control system must generate torques by varying the tether attach point on the platform. This result arises because the force that the tether applies to the sub-satellite is at least one order of magnitude greater than any other environmental disturbing force. If the tether is not attached exactly at the sub-satellite mass center, a conventional control algorithm will expend too much energy fighting this disturbance torque. In addition, it is virtually impossible to a priori determine the center of mass location to arbitrary precision for any satellite, and tethered sub-satellites will likely not be exceptions to this rule. These considerations lead directly to the need to vary the tether attach point on the observatory platform. Further, the authors also discuss the KITE flight test configuration and hardware. They suggest that the mission include large angle slew maneuvers on the order of 30 deg and inertially fixed pointing, to exhibit long term attitude regulation on the order of 1 arcsec.

The current research is designed to simulate the KITE flight test mission in a laboratory environment. The goals of the research are to construct a laboratory simulator suitable for extensive testing, to design a control algorithm which can exhibit both large angle slew and long term, high accuracy pointing maneuvers with the laboratory simulator, to construct a tether dynamics simulator to determine the effect that natural tether dynamics will have on the control algorithm, and to vary linearity assumptions and system models to determine the robustness of the control design. Finally, it should be noted that any future reference to the orbital case or orbital conditions refers to the proposed Space Shuttle flight test of KITE and the conditions expected throughout that mission.

1.3 Previous Work and Related Results

Interest in tethered satellites remained relatively subdued until the the 1960's. The reason for the lack of interest is mainly that available materials did not possess sufficient structural characteristics (they were either too heavy or too weak) to warrant

the construction of long space tethers. Since then, however, numerous studies of tethered satellite uses and dynamics have been presented in the open literature. The focus of the studies concentrate on the analysis of station-keeping, the analysis of tether materials, the analysis of deployment and retrieval, the description of experiments with tethered satellites, and the detailed analysis of proposed uses. The following section will provide a brief review of previous work on tethers and a description of related results.

The studies which focus on the station-keeping phase of tethered satellite missions typically involve a dynamic analysis of the specific system and some conclusions based on an analytic solution or computer simulation. Misra and Modi [7] compiled an extensive survey of numerous dynamic analyses and their results. Many past studies can be classified by their treatment of the model used for the tether. The most simple studies model the tether as massless and inextensible [8][9]. Including tether mass adds one level of complexity and was discussed in relation to tether activities on the Space Shuttle [10][11]. The most popular tether model consists of a massless spring/damper and has been studied in great detail [12]-[19]. These studies consider everything from simple, extensible dumbbell satellites to more complex orbiting, tethered antennas. The general conclusions are that care must be taken when designing tethered satellites because of the interaction between the flexible tether and orbital perturbations. Massive, flexible cable models contain longitudinal as well as transverse tether dynamics and have garnered a fair amount of research interest [20]-[24]. These research efforts concentrated on subjects related purely to the behavior of the tether material, sub-satellite maneuverability by the use of transverse waves, and the orbital stability of satellites with flexible tethers. Finally, the case of general, flexible appendages has been studied in the context of the influence of spacecraft flexibility and orbital motion [25]-[27]. Other dynamic complications can be added by including extended end masses, as was performed to study the effect of damping which arises from relative motion between the end masses and the tether [15][16]. Adding damping mechanisms between the tether and end masses helped reduce undesirable end mass rotations. The effects of orbit eccentricity on tethered satellite station-keeping have been studied in numerous contexts [13][17][21] [11][28]. In general, these studies

found that orbit eccentricity will pump the pendular modes of the spacecraft, but not significantly enough to be destabilizing. Finally, a number of studies included coupling between motions which occur out-of-plane and in-plane (see, for example, [17][21] and [27]). These researchers conclude that for motions which occur in the linear region, out-of-plane dynamics are decoupled from in-plane dynamics.

Recently, a number of studies have considered the tether as a continuum, the authors have employed various models to describe damping [29][30][31]. These studies have determined the natural frequencies and damping properties expected of long space tethers. Most tether missions will have both a deployment and a retrieval phase and considerable analysis has been performed to determine stable methods to perform both tasks. Some of the station-keeping studies considered deployment in addition to station-keeping [16][8][9][10][11]. Other studies have been solely devoted to the question of deployment, which is a dynamically stable process [32][26][21][33]. The unstable retrieval phase has been studied less frequently, however, a number of authors have presented various methods to perform the retrieval. The methods can be generally split into two groups: those that depend on tether length rate laws [9][10][11][34] and those that depend on some sort of thruster augmentation alone [35] or in combination with a rate law [36]. Kane [37] suggests a novel approach which leaves the tether deployed while the sub-satellite crawls back to the parent.

The first (and only) flight experiments with tethered satellites were performed during two Gemini missions in 1966 [1][38]. The mission plans for Gemini XI and XII contained provisions to exhibit tethered satellite constellations. Both missions connected a spent, unmanned Atlas-Agena rocket stage to the Gemini capsule with approximately a 30 m polyester cable. The first mission exhibited a rotating concept (as would be used to generate artificial gravity) and the second mission was deployed in the gravity gradient stabilized configuration. In 1970, Austin and Bauer [39] report on a series of experiments they performed with a laboratory simulator of a rotating, cable-connected space station. Their hardware consisted of a rigid frame which suspended a flexible cable and two end modules. The suspension system allows three degrees of rotational freedom for each end mass and the frame can be rotated about the system center of mass. Other than the current research and above examples, no

flight test or laboratory work has been performed to exhibit any aspect of tethered satellite behavior.

There have been numerous descriptions of proposed tethered satellite uses in the open literature. A summary of proposed and continuing research projects has been compiled by the NASA Office of Space Flight in the form of two handbooks related to tethers in space [40][41]. Both handbooks serve as excellent references for all aspects of tether fundamentals. A number of studies relate directly to KITE. As mentioned previously (see Section 1.2) Lemke [5] and Lemke, Powell, and He [6] discuss the advantages of tethered observatories, the need for sub-satellite tether attach point motion to generate attitude control torques, a sample attitude control algorithm, and results related to vibration isolation from the parent spacecraft. Lemke [42] reviews and strengthens the previous derivations of the KITE project, this time related to Space Station deployment, and adds a quantitative analysis of contamination isolation for a tethered observatory. In support of the KITE project, two reports to NASA Ames Research Center were prepared by Powell, Lemke, and He [43] and Powell, He, and Schoder [44]. These reports summarize the findings of the researchers and introduce many of the concepts and results contained in the other works. Also in support of KITE, Stephenson [45] performed a detailed computer simulation of the dynamics and control of a tethered observatory deployed from the Space Shuttle. The goals of his work were to exhibit the six degree of freedom behavior of the KITE sub-satellite along with a NASA model of the tether and Shuttle dynamics. He [31] presents results which provide a method to model the longitudinal and lateral dynamic behavior of long space-based tethers. In addition, He derives a three dimensional, six-degree of freedom computer model and control algorithm based on generating control moments by varying the tether attach point. Both researchers conclude that the movable attach point control mechanism will, in fact, achieve orientation control on the order of 1 arcsec.

1.4 Contributions of Current Research

The research described in this dissertation has extended the current body of knowledge surrounding tethered satellites in a number of areas. Most notably, the contributions include:

- The design and construction of an air-bearing supported, tethered satellite simulator suitable for laboratory testing, and the design and construction of a tether dynamics simulator which can be used to simulate the natural dynamics of long space tethers.
- The development of a large angle slew and long term, precision attitude control system (for the pitch axis) which generates control torques with a movable tether attach point for the laboratory simulator.
- The demonstration of both a large angle slew maneuver and long term, high accuracy attitude control in a disturbance-free environment with the laboratory simulator.
- The experimental testing of the effects of varying system parameters, linearity assumptions, and control algorithm complexity (i.e., system model) on the performance of the precision attitude control system (in the disturbance-free environment).
- The experimental determination of the effects that tether tension magnitude and in-plane (pitch) direction variations on the precision attitude control system.
- The derivation of the correspondence between the observed behavior in the laboratory and the expected flight test configuration.
- The experimental testing of the effect of control algorithm complexity (i.e., mass center estimation) and the effect of adding tension magnitude measurements to the control algorithm on the performance of the precision attitude control system (in the presence of tether tension variations).

1.5 Reader's Guide

This dissertation is organized into five chapters and an appendix. This first chapter provides an introduction to the concept and history of tethered satellites, a general description of their potential uses, and a detailed description of the astrophysical pointing platform control problem (which is the focus of the current work).

The second chapter provides a detailed summary of the hardware which was assembled in order to construct a laboratory simulation (pitch plane) of a typical tethered satellite. The information contained therein includes a system level (i.e., flotation, power, attach point positioning, computer, and sensor) description of the air-bearing supported vehicle which serves as the astrophysical pointing platform simulator. In addition, Chapter 2 contains the description of a tether dynamics simulator constructed to simulate the dynamics (longitudinal and in-plane lateral) of a long space tether. Finally, Chapter 2 describes the development of a number of key scaling parameters which make the laboratory results meaningful in an orbital context.

The third chapter derives all the necessary equations of motion and control equations which were used to implement the attitude control algorithm for the simulator. The general equations of motion for a tethered satellite end mass are derived with the following assumptions: in-plane motion is decoupled from out-of-plane motion, the parent spacecraft has a mass which is much greater than both the tether and sub-satellite, the parent moves in a circular orbit, and the tether is massless and extensible. The equations for the laboratory simulator are derived by setting the orbital rate to zero and including the effects of the micro-gravity acceleration experienced by the orbiting tethered satellite. The final sections of Chapter 3 contain the detailed derivation of the control algorithms used for pitch plane orientation control for both a large angle slew maneuver and a fine pointing attitude regulator.

The experimental program is described in the fourth chapter. The first section covers the experiments in a disturbance-free environment. A demonstration of both a large angle slew and a long term, high accuracy regulator are described. The following sub-sections contain descriptions of the experiments used to quantify the effects to the control of estimator gain magnitude, the mass center estimator, and variations in the

physical parameter used to model the stepper motor. The second section considers the effects of environmental and tether disturbances on the ability of the control system to regulate the sub-satellite orientation. Tether tension magnitude and direction variations are used as the basis of the experimental program related to determining the effects of natural tether dynamics on the control algorithm. Longitudinal and lateral in-plane dynamics are described and their effects quantified. The final sub-sections quantify the need for mass center estimation and tension feedback scaling in the case where tether dynamics can be significant.

The last chapter draws conclusions based on the analysis and experimental results presented in the previous three chapters. The appendix contains a sample FORTRAN program which was used to perform the interrupt driven control algorithm and a FORTRAN subroutine which was used to computer simulate the laboratory hardware.

Chapter 2

Experimental Hardware

An experimental facility was developed in order to test the proposed tethered satellite attitude control concept which generates control moments by tether attach point positioning relative to the vehicle mass center. The laboratory simulator possesses three degrees of freedom, one in rotation and two in translation. Therefore, the laboratory simulation reduces the six degree of freedom orbital case to motions which occur purely in the orbit plane. The purpose of the experimental facility is to verify analytic predictions of closed-loop attitude control, to gain a better understanding of the technological requirements (hardware and software) in order to implement the concept, and to determine the sensitivity of the design to variations in mission requirements, linearity assumptions, and design parameters. The experimental facility consists of two major subsystems: an air-bearing supported vehicle to simulate the satellite dynamics and a pair of positioning tables fitted with DC servo motors to simulate natural tether motions. A detailed description of the design of each of the subsystems follows. In addition, the configuration of the laboratory equipment as it is used to simulate the orbital dynamic conditions is described. Finally, the relationship between the results obtained in the laboratory and those expected on orbit are detailed with the derivation of important scaling parameters.

2.1 Air Bearing Vehicle

The air bearing vehicle consists of a flotation plate to provide friction-free suspension in the plane of motion and a chassis to provide a convenient mounting platform for the necessary hardware. A photograph of the vehicle is shown in Figure 2.1. The photograph shows that the vehicle floats on top of a very smooth granite table and that the tether is connected to the positioning mechanism at the nominal center of mass of the vehicle. Figure 2.2 shows an exaggerated schematic side view representation of the hardware. The granite table is tilted a small angle, β, with respect to the local gravity vector. To simulate a 2 km long tethered satellite, the table tilt has been adjusted so that $\beta \approx 2$ arcmin. This tilt angle results in the following micro-gravity acceleration:

$$g' = g\sin(\beta), \tag{2.1}$$

where g is the value of the local acceleration of gravity on Earth (9.81 m/sec^2). Therefore, $g' = 0.008$ m/sec^2. This value of micro-gravity acceleration is identical to that experienced by a 2 km long tethered satellite in a nominal 250 km altitude, circular orbit (see Chapter 3 for a detailed derivation of the micro-gravity acceleration for tethered satellites). In addition, Figure 2.1 shows each of the major components and related connections on board the air bearing vehicle. The on-board gas, power, positioning, computer, and sensor systems will be described separately.

2.1.1 Gas and Flotation System

A schematic diagram of the gas and flotation system is shown in Figure 2.3. The flotation plate is a 2.5 cm thick, 1 m diameter, circular aluminum disk. The underside of the plate is ground flat to approximately 25 μm, which provides a smooth surface on which the vehicle rides. The center of the plate is fitted with a small threaded hole which serves as a gas supply hook-up. The gas cylinders on the vehicle store the gas (dry nitrogen) which is used solely for flotation. From the cylinders, the gas passes through a pressure regulator, then through a needle valve, before passing through the gas hook-up in the flotation plate. After passing through the plate, the gas enters a 15 cm diameter plenum on the underside of the plate, and then flows

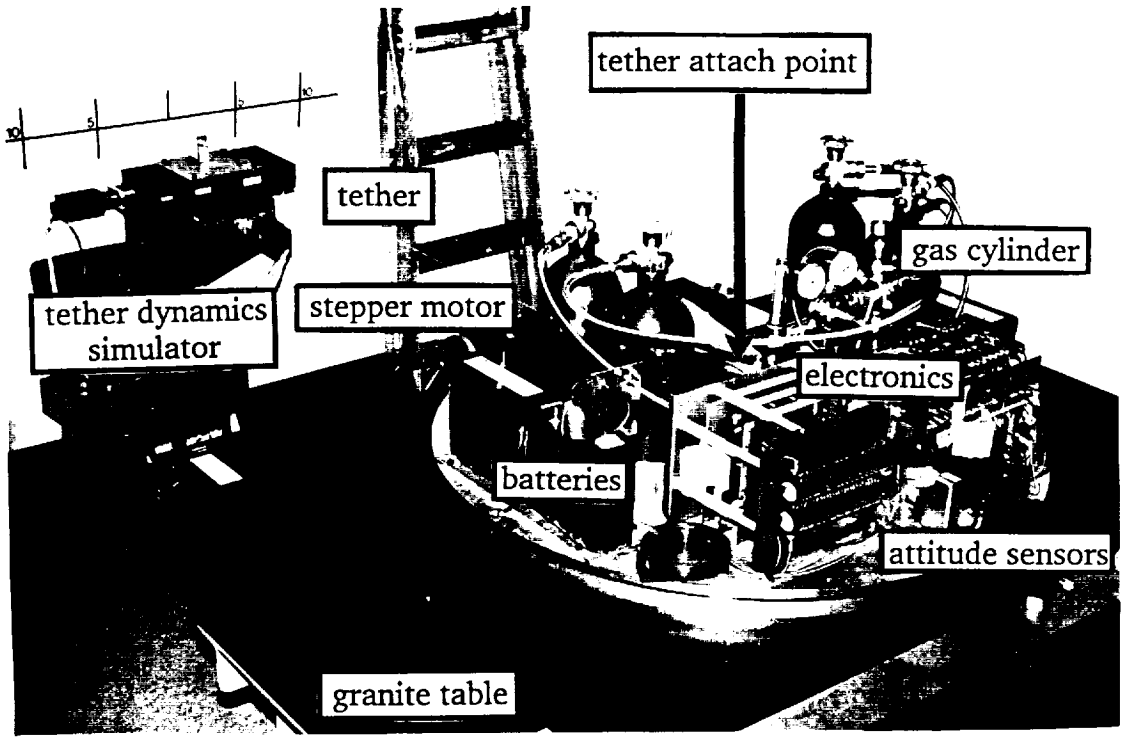

Figure 2.1: Photograph of Laboratory Simulator

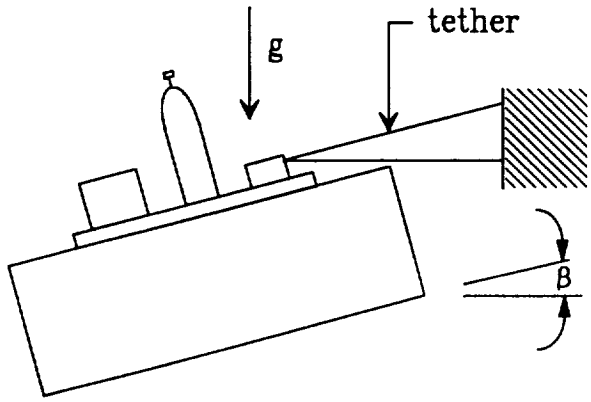

Figure 2.2: Schematic Side View of Experimental Setup

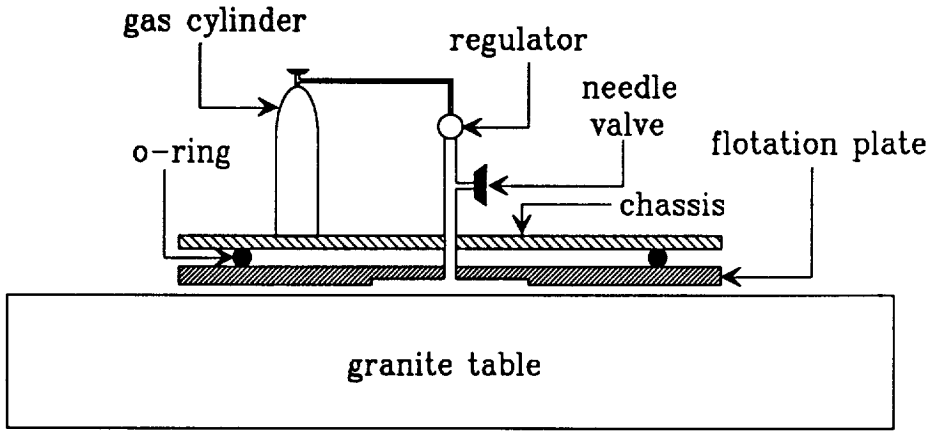

Figure 2.3: Schematic of Gas and Flotation System

out to the surrounding environment between the granite table and the flotation plate. The system was designed (see Majumdar [53] and Grassam and Powell [54]) such that the gas flow rate would be approximately 0.27 m^3/hr, the maximum mass to be lifted would be 1000 kg, and the nominal distance between the bottom of the plate and top of the granite table would be approximately 75 μm.

The chassis plate is a 1 m diameter disk made of 1.25 cm thick aluminum. The chassis is positioned and held in place on top of the flotation plate by means of two locating pins. The weight of the chassis is distributed on the air bearing with a 9.375 mm diameter solid o-ring positioned between the plates at two-thirds of the outer radius. This weight distribution scheme was chosen in order to minimize load variations from the chassis on the air bearing plate and to minimize the deflection of the air bearing due to the chassis loading. A top view of the position of the components mounted on the chassis is shown in Figure 2.4. The individual components are arranged in a symmetric fashion about the center of the plate. This mounting style helps to ensure that the center of the plate will nominally be the mass center of the entire vehicle. As discussed by previous authors [6], this center of mass configuration is advantageous because it minimizes both the necessary actuator size and control energy.

The air bearing vehicle is subjected to small forces which are a result of the suspension system and which arise from the viscous drag of the flotation gas. Rehsteiner [48] performed a detailed study of the properties of all types of gas bearings. The set of actual forces exerted by the suspension system on the vehicle can be replaced with a drag force, $\underline{\mathbf{D}}_{cm}$, applied at the vehicle center of mass and a drag torque, $\underline{\mathbf{T}}_{cm}$, (a couple) acting about a line perpendicular to the granite table top surface passing through the vehicle mass center. Rehsteiner derived the analytic expressions for both the drag force and torque. His results, for a circular bearing with an outer radius of r_0, show:

$$\underline{\mathbf{D}}_{cm} = -\frac{\mu \pi r_0^2}{H^*} I_0^* \underline{\mathbf{v}} \tag{2.2}$$

and

$$\underline{\mathbf{T}}_{cm} = -\frac{\mu \pi r_0^4}{H^*} I_2^* \underline{\Omega}. \tag{2.3}$$

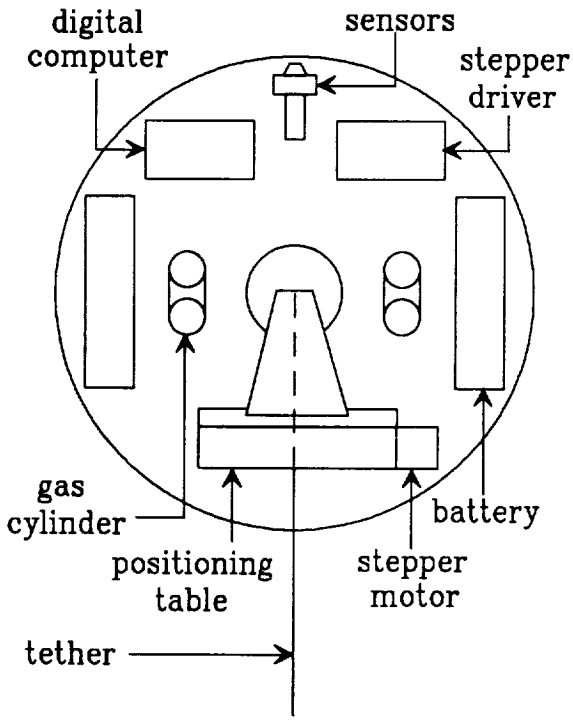

Figure 2.4: Component Layout of Chassis

In each of the above equations,

μ is the coefficient of viscosity of the gas,

H^* is the nominal height of the bearing above the table,

$\underline{\mathbf{v}}$ is the velocity vector of the vehicle mass center, and

$\underline{\Omega}$ is the angular velocity vector of the vehicle.

In addition,

$$I_0^* = \frac{(1 - r^*)^2}{H_c} \tag{2.4}$$

and

$$I_2^* = \frac{(1 - r^{*4})}{2H_c}, \tag{2.5}$$

where $H_c = 1$ (for a constant gap clearance) and r^* is the ratio of the plenum radius to plate radius. Substituting the values for the given laboratory equipment into Equations 2.2–2.5, the drag force and drag torque can be evaluated to be:

$$\underline{\mathbf{D}}_{cm} = -.186\,\underline{\mathbf{v}} \tag{2.6}$$

and

$$\underline{\mathbf{T}}_{cm} = -7.5 \times 10^{-7}\,\underline{\Omega}. \tag{2.7}$$

For a typical laboratory experiment, $|\underline{\mathbf{v}}| \leq 6 \times 10^{-4}$ m/sec and $|\underline{\Omega}| \leq 3 \times 10^{-3}$ rad/sec. Then, the magnitude of the drag force and drag torque can be computed to be approximately 1.1×10^{-4} N and 2.3×10^{-9} N-m, respectively. Clearly, both the drag force and drag torque due to the suspension system are extremely small and will have negligible effect on the dynamics of the simulator.

2.1.2 Power System

The power system consists of rechargeable batteries and DC-DC converters to condition the raw battery power to the required voltages for the on-board equipment. The battery pack consists of two 12 V, 25.0 A-H, Cyclon Monobloc Batteries, manufactured by Gates Energy Products. A full charge provides the vehicle with approximately 3 hours of continuous power. The two converters, manufactured by the

Stevens-Arnold Division of Computer Products, Inc., condition the 24 Volts of the batteries to provide 5 V @ 10.0 A and ±12 V @ 750 mA.

The following equipment requires power from the on-board batteries:

- the on-board computer requires 5 V and ±12 V,
- the stepper motor driver is rated at 24 V, the motor indexer needs a 5 V source, and
- the sensors require a ±12 V supply.

2.1.3 Positioning System

The hardware used to position the tether attachment with respect to the vehicle mass center consists of a high accuracy positioning table and a high torque stepper motor. The positioning table, manufactured by Design Components Inc., provides a single axis of travel with a maximum stroke of 15 cm. A typical large angle slew maneuver requires approximately ±1.5 cm (3 cm maximum stroke) of travel to generate the peak amount of control torque. The table is located on the chassis so that the vehicle mass center is aligned with the center of the positioning table travel (see Figure 2.4). As a result, the attachment point can be varied ±7.5 cm with respect to the vehicle center of mass. The table drive is geared such that one complete turn of the input shaft corresponds to 0.5 cm of linear travel. The linear travel has a resolution of 25 μm and is repeatable to 2.5 μm [55].

The stepper motor is manufactured by Sigma Instruments, Inc. and is used to turn the input shaft of the positioning table. Operated in full step mode, the motor realizes 200 steps/revolution, which corresponds to 25 μm of linear positioning table travel per step. The motor is operated at 2000 steps/second and provides a maximum torque value of 5.75 N-m, and the holding torque provided by the motor is 4.25 N-m [56]. The drive electronics for the motor consists of a driver and indexer board. The indexer generates the required pulses to each of the of the four motor phases and the driver provides the necessary current amplification in order to rotate the motor

shaft. These electronic boards are manufactured by Superior Electric Corp. and are interfaced directly into the computer system bus.

An important consideration when choosing the positioning table and stepper motor combination is the relationship between the motor shaft rotation of one step and the linear translation associated with the step. As discussed above, one step of the motor corresponds to 25 μm of linear positioning table travel. Since the position of the tether attach point with respect to the vehicle mass center is a discrete function (due to the discrete shaft positioning of the stepper motor), a limit cycle can occur. This limit cycle would result from a misalignment between the vehicle mass center location and one of the possible (discrete) positions of the attach point. In other words, in the steady state (when there should be zero control moment), if the vehicle mass center is not located directly at one of the discrete positions of the attach point, a torque will be applied to the vehicle. As the orientation of the vehicle changes due to the application of the torque, the control system will move the attach point to halt the angular motion. Since the new attach point position will not be located at the vehicle center of mass, a torque in the opposite direction will be applied until the sequence is repeated, resulting in a limit cycle.

To analyze the magnitude of this effect, it was assumed that the mass center of the vehicle falls directly half-way between two possible attach point locations. In this case, if it is assumed that the time it takes to move from one attach point location to another is negligible compared to the sample period, the magnitude of the torque applied to the vehicle at each attach point location is the magnitude of the tether tension multiplied by half of the positioning table accuracy. Further, if it is assumed that the control system functions such that the attach point is moved from one location to the other after each sample period, the torque applied to the vehicle will have a time history as shown in Figure 2.5. In the figure, F_0 is the nominal tether tension magnitude, x is the distance of linear travel associated with one step of the stepper motor, and T is the sample period. In the previously described scenario, the equations describing the dynamic behavior of the state of the vehicle can be expressed as:

$$\dot{x}_1 = x_2 \tag{2.8}$$

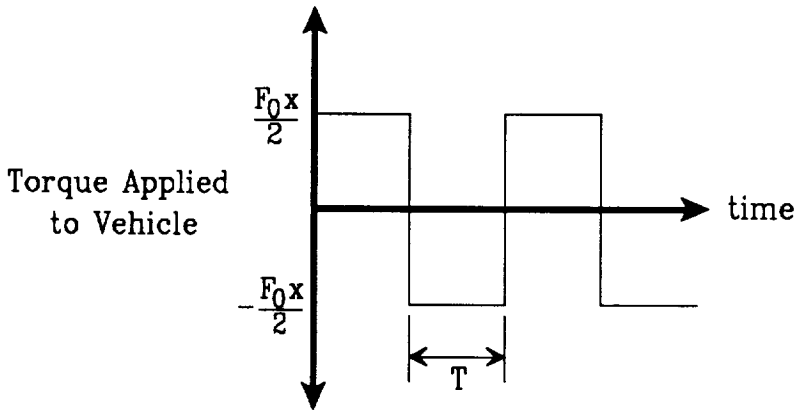

Figure 2.5: Time History of Torque for Limit Cycle Behavior

and

$$\dot{x}_2 = \pm\frac{F_0 x}{2I}, \tag{2.9}$$

where I is the vehicle moment of inertia for the mass center about an axis perpendicular to the granite table, x_1 represents the vehicle orientation (attitude), and x_2 represents the angular rate of the vehicle. Dividing Equation 2.8 by Equation 2.9 it can be shown that:

$$\frac{dx_1}{dx_2} = \pm\frac{2Ix_2}{F_0 x}. \tag{2.10}$$

Solving Equation 2.10 for the state variables (angle and angular rate) yields:

$$x_1 = \pm\frac{I}{F_0 x}x_2^2 + c_1, \tag{2.11}$$

where c_1 is a constant of integration. Equation 2.11 provides a convenient phase-plane description of the motion of the system and Figure 2.6 is a graphical representation of the equation. The vehicle traces the closed curve P_1-P_2-P_3-P_4, changing the value of the state vector between pure angular velocity (at P_1 and P_3) and pure angular displacement (at P_2 and P_4). In addition, Equation 2.9 can be integrated to yield:

$$x_2 = \pm\frac{F_0 x}{2I}t + c_2, \tag{2.12}$$

where t is the time, and c_2 is another constant of integration (which represents the value of x_2 at zero time). From Figure 2.6 it can be seen that the time for the vehicle

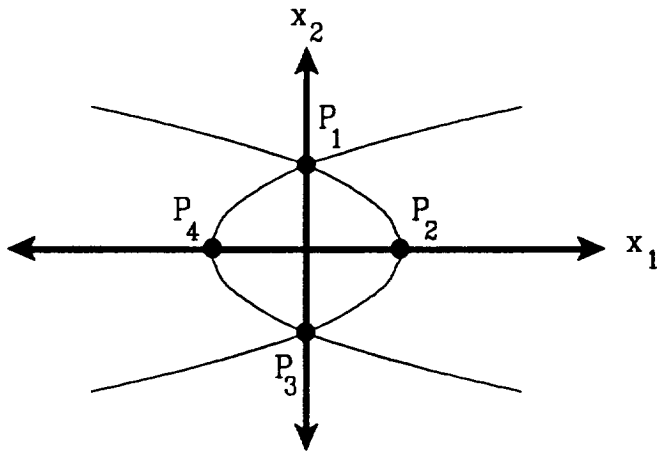

Figure 2.6: Phase-Plane Description of Possible Limit Cycle Motion

to change state from P_3 to state P_1 is given by the sample period, T. By symmetry, it can be shown that the time to change state from P_4 to P_1 is simply half the sample period. Therefore, at P_1,

$$x_2 = \frac{F_0 x T}{4I}. \tag{2.13}$$

Also, x_1 is zero at P_1. Combining this observation with Equations 2.11 and 2.13 it can be shown that:

$$c_1 = \mp \frac{F_0 x T^2}{16I}. \tag{2.14}$$

As a result of Equation 2.14 and the fact that at P_2, x_2 is zero, the maximum value of x_1 (at P_2) is:

$$x_1 = c_1 = \frac{F_0 x T^2}{16I}. \tag{2.15}$$

Therefore, the maximum value of the angular displacement during the limit cycle is directly proportional to the tether tension, the positioning table resolution, and the square of the sample period and inversely proportional to the vehicle moment of inertia. For the laboratory simulator as built (see Section 2.3), the maximum value of the angular displacement can be shown to be 5.5×10^{-3} arcsec, and for the proposed orbital flight test (see Section 2.3), the maximum displacement is 2.7×10^{-3} arcsec. These extremely small values show that to the accuracy required, the discrete nature of the positioning system should have no effect on system performance.

2.1.4 Computer System

The on-board computer system was chosen such that the unit would provide a free-standing computational environment which would be sufficient to implement the necessary digital control algorithms. The computer is practically identical to the system assembled by Alexander [58] used in his work on the control of satellite manipulators. The computer is an STD bus-based system, with an 8088 microprocessor and 8087 math co-processor. In addition, an 80130 utility chip has been programmed to perform interrupt-driven control loop calculations. As a result of the 8088 microprocessor, many of the software development tools which are available on an IBM PC-AT are compatible with the on-board system. Therefore, an IBM PC-AT was chosen for program development and to serve as a host for the on-board computer. The source code for a sample control program, written in FORTRAN, is shown in Appendix A.1. The software for downloading compiled high level control programs from the host IBM PC-AT, as well as the ULDOS operating system environment, is identical to that described by Alexander [58]. Once the control program has been loaded into the memory of the on-board computer, the downlink connection from the AT is broken and the on-board system is independent of the host. The major difference between the current system and Alexander's system is the implementation of a communication link with the AT host over a fiber optic cable and modem. The cable is attached at the tether attach point on the vehicle to minimize any possible torques generated by the connection. The communication link is not used in the real time control algorithms, it is merely convenient as a method of program control (starting, stopping, interrupting, etc.) and as a means of transferring data collected during an experiment to the host AT for analysis. To determine the effect of the cable on the experimental results, software was compiled which allowed the fiber optic cables to be disconnected during execution of the control algorithms. Since the results of these tests showed no effect on the behavior (for both the large angle slew and fine pointing algorithms) it was decided that the more convenient, always connected configuration, would be employed for the rest of the experiments.

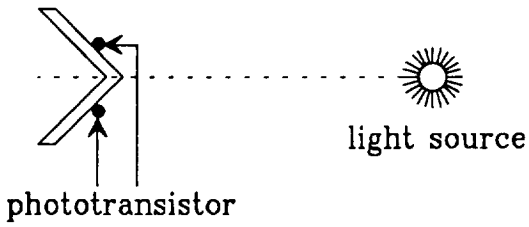

Figure 2.7: Schematic of Coarse Phototransistor Angle Sensor

2.1.5 Sensor Systems

The on-board angle sensors are used to measure the angular orientation of the vehicle with respect to an inertial reference in the laboratory. A combination of two sensors has been implemented: a coarse sensor with a large dynamic range and a relatively large noise level, and a high accuracy sensor which has a limited dynamic range and a very small noise level. The goals of the laboratory experiment, as stated previously, are to exhibit large angle slew capability on the order of 30 deg and to show long term, fine pointing stability on the order of 1 arcsec. Hence, the two sensors can be used in combination to provide the large angle sensing required for the slew and to provide high accuracy angle measurements for the long term stability tests.

A schematic diagram of the coarse sensor is shown in Figure 2.7. The sensor is constructed of two phototransistors mounted 90 deg relative to each other. Phototransistors operate in the same fashion as bipolar transistors, with one exception. The phototransistor emitter current is proportional to the light energy incident upon the radiation sensitive collector-base junction, whereas the bipolar transistor emitter current is proportional to the base current. Therefore, the current output of each phototransistor is proportional to the product of the source intensity and the cosine of the incidence angle. Assuming a constant source intensity, each phototransistor output represents the cosine of the incidence angle. In the nominal configuration shown in Figure 2.7, the incidence angle for each phototransistor is the same. As a result, the relative orientation of the mount with respect to the light source is zero. As the mount rotates about an axis perpendicular to the plane of the paper, the

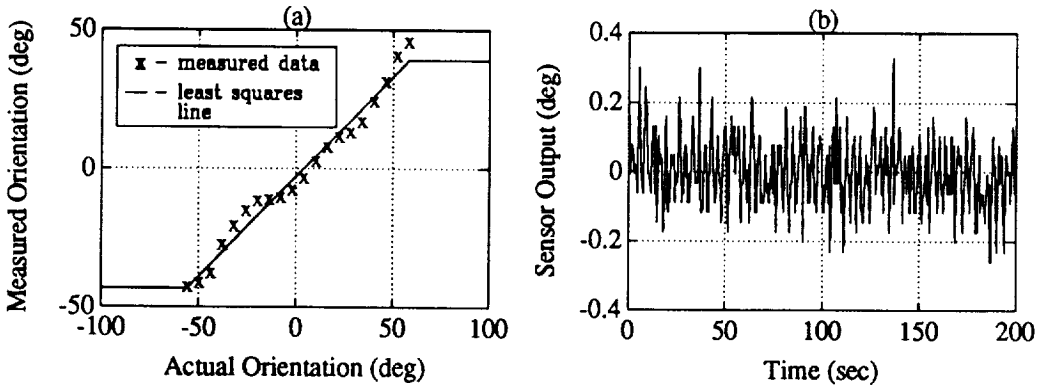

Figure 2.8: Static Coarse Angle Sensor Output

incidence angle of the light from the source is different for each phototransistor. Due to the rotation, then, the transistor outputs will be unequal and taking the difference of the outputs will yield a linear measure of the relative orientation of the phototransistor mount with respect to the light source. The static output of this sensor is shown in Figure 2.8. The figure shows both the static relationship between the actual and measured orientation of the vehicle and the noise characteristics of the sensor. In Figure 2.8(a), the x's correspond to actual measurements and the solid line represents a least squares fit of the data to a straight line. As you can see, the dynamic range is approximately ± 45 deg and the data follows a basically linear pattern. Figure 2.8(b) shows that the sensor possesses an RMS noise level of approximately 0.1 deg.

The high accuracy angle sensor takes the form of an autocollimator. A schematic diagram of the optical hardware for an autocollimator is shown in Figure 2.9. The figure shows a condenser lens which serves to collect and focus the light from the integral light source. The beam of collected light then bounces off of the reflecting surface of a beam splitter and lands on the objective lens. The objective lens serves as a collimating lens for the light traveling away from the beam splitter. If q, the angle of the external mirror with respect to the collimated light, is zero, the collimated beam is reflected back upon itself, passes through the objective lens heading back through the beam splitter (in the non-reflecting direction), and is focused as a point on the optical axis on the focal plane of the lens. If the mirror angle (q) is finite, the collimated beam is reflected from the mirror in an off-axis direction. The light

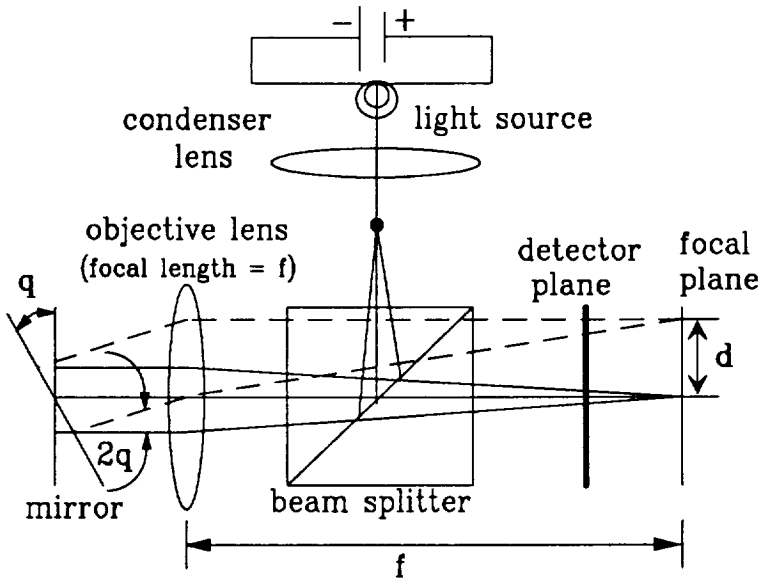

Figure 2.9: Schematic of Autocollimator Optics

then passes through the objective lens which focuses the beam on the focal plane at a distance, d, from the optical axis. The value of d can be shown to be:

$$d = (2q)f, \tag{2.16}$$

where f is the focal length of the objective lens. By placing two photosensitive transistors along a plane parallel to the focal plane (with one just above the optical axis and one just below the optical axis), a linear measure of the relative angular position of the mirror and the autocollimator can be derived by comparing the relative amounts of light energy which fall on each detector. The autocollimator used in this study was developed by Lorell [59] for the work he did in the precision attitude control of spinning bodies. Figure 2.10 shows a graph of the actual orientation change versus the measured change and a representative time history of the static output of the autocollimator. In Figure 2.10(a), the x's correspond to actual measured data points and the solid line represents a least squares fit line to the data. You can see that the autocollimator has a dynamic range of approximately ± 0.5 deg and that the measured orientation follows a very nearly linear correspondence with the actual

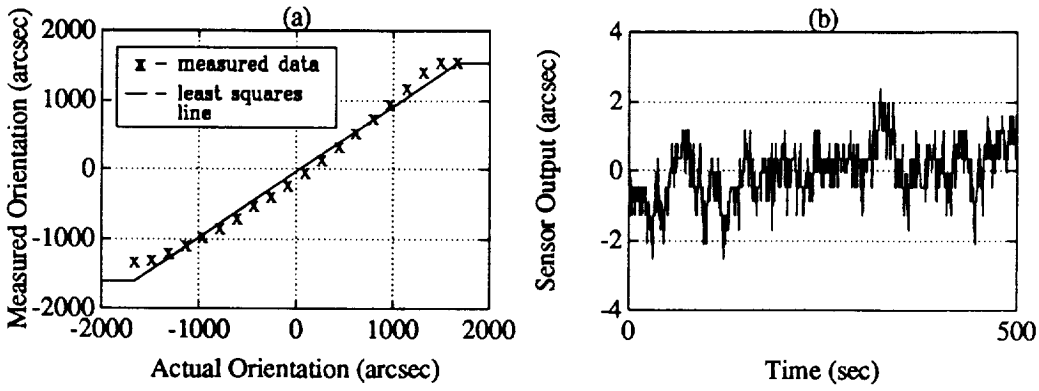

Figure 2.10: Static Autocollimator Output

vehicle orientation. Figure 2.10(b) shows that the static output of the autocollimator possesses an RMS noise level of 0.77 arcsec.

Finally, in order to closely monitor the value of the force present in the tether, it was decided to outfit the air-bearing vehicle with a force measuring device. A load cell has been placed at the attachment of the tether on the air-bearing vehicle. The load cell is a flatline model ELF-T1000-2, purchased from Entran Devices, Inc. The specifications show [57] a dynamic range of 0-2 lbs (0-8.9 N) with a sensitivity of 100 mV/lb (22.5 mV/N).

2.2 Tether Dynamics Simulator

The tether dynamics simulator was developed in order to provide a means of varying the magnitude and direction of the tether tension which is applied to the air-bearing vehicle. It is important to have this capacity in order to test the behavior of the fine pointing control algorithm when the satellite is subjected to tether force magnitude and direction variations. A complete theoretical analysis of the dynamic behavior of long tethers in space and their effect on the closed-loop attitude control of tethered spacecraft is presented by He [31]. The tether dynamics simulator was constructed in order to verify the theoretical pointing accuracies derived in this study.

A photograph of the tether dynamics simulator is shown in Figure 2.11 and a schematic diagram of the same system is shown in Figure 2.12. These figures show

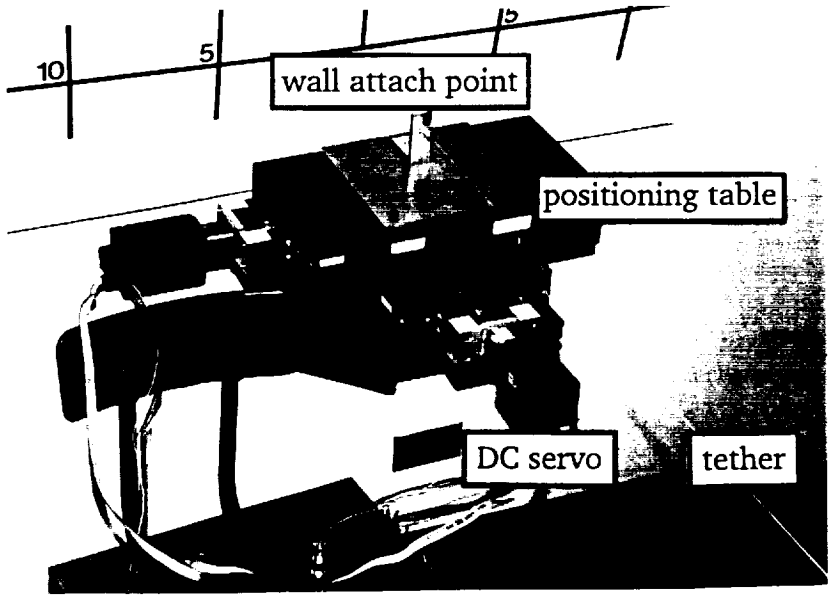

Figure 2.11: Photograph of Tether Dynamics Simulator

positioning tables which are mounted in a plane parallel to the granite table top. The tables were manufactured by Design Components, Inc. and possess the same positioning accuracy as the table used to perform the on-board positioning of the tether attach point [55]. Each table is fitted with a DC servo motor manufactured by Pittman. Both motors possess 200 count/revolution (CPR) optical shaft encoders and 24:1 planetary gearheads. These motors were chosen in order to drive the positioning tables at a maximum linear speed of 75 mm/sec. A closed-loop position control algorithm uses the shaft angle measurements of the motors to track sinusoidally varying reference shaft paths (in the directions parallel to and perpendicular to the nominal tether direction). The control algorithm is written in C and runs on an 8096 based computer on a card which plugs into one of the expansion slots of an IBM PC-AT. The card, which plugs into the AT, was manufactured by Integrated Motions Inc. and operates completely independently of the host AT. Control programs can be developed on the host AT, compiled with a special 8096 C compiler, and then loaded into the 8096 computer (with software provided by Integrated Motions). As a result,

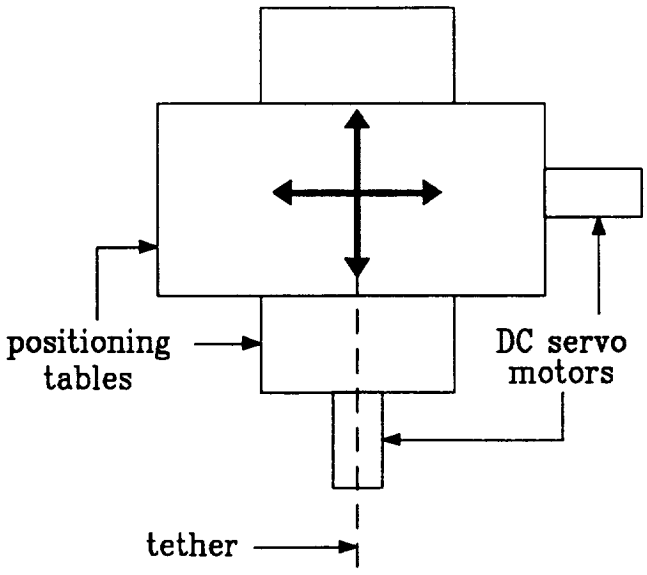

Figure 2.12: Schematic Diagram of Tether Dynamics Simulator

the position of the tether attachment at the wall (and, therefore, the magnitude and direction of the tether tension force) can be varied in parallel with the operation of the on-board control algorithm and the AT communication software discussed above.

The hardware is configured in the laboratory in such a way that the air-bearing vehicle and wall attach point mechanism provide a replication of the conditions that would exist in an orbital case. A schematic diagram of the air-bearing vehicle and tether dynamics simulator is shown in Figure 2.13. The figure shows that the vehicle is suspended on top of a granite table. The vehicle is connected to the tether dynamics simulator (which is mounted on a nearby wall) with a short piece of Spectra tether material and a linear spring. The wall attach point mechanism can be used to introduce tension variations (in both magnitude and direction) by simply sinusoidally varying the tether attachment position at the wall. Parallel to the nominal tether direction, the mass and spring behave like a lightly damped oscillator, and perpendicular to the nominal tether direction, the vehicle behaves like a pendulum. As a result, at each frequency of oscillation for the wall attach point (and in each

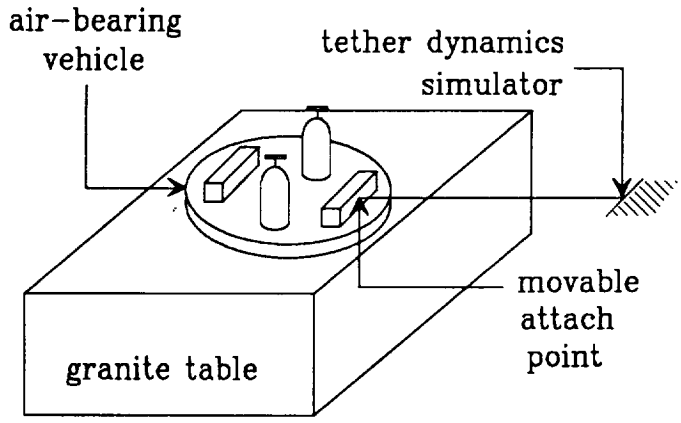

Figure 2.13: Schematic Diagram of Experimental Setup

direction), steady state motion is characterized by the oscillation frequency and the transfer function gain. From the transfer function gain, the amount of input disturbance can be calibrated for purposes of comparison to theoretical predictions (see Sections 4.2.3 and 4.2.4).

2.3 Laboratory Results and Orbital Performance

The laboratory simulator possesses physical characteristics which differ from the nominal design of the flight test vehicle. For example, the values of the total mass and moments of inertia for the laboratory vehicle are quite different from the values expected for the flight test configuration. In order to quantify how the dynamic behavior of the laboratory simulator will differ from that of the flight vehicle, important scaling parameters have been derived. These parameters include the tether length, the frequency of oscillation of the mass-spring mode of the tether and vehicle, the microgravity field, and the closed-loop system bandwidth. Table 2.1 is a summary of the values of these scaling parameters for the laboratory vehicle and the expected flight test design.

The nominal design tether length for the flight test configuration is 2000 m. Obviously, there are physical constraints which prohibit the implementation of this long a

Quantity	On Orbit	In Lab
tether length, L (m)	2000	2
mass-spring mode, f_m (Hz)	0.025	0.034
micro-gravity, g' (m/sec^2)	0.0082	0.008
bandwidth, f_n (Hz)	0.12	0.16

Table 2.1: KITE Scaling Parameters

tether in a laboratory environment. A 2 m long tether is attached from the laboratory simulator to the tether dynamics simulator. In order to make this length of tether less stiff (so that unacceptably large tension variations are not generated by very small attach point motions), a linear spring has been inserted between the tether and the tether dynamics simulator. In addition, "softening" the laboratory tether (with the spring) is useful when varying the magnitude and direction of the tether force (see Sections 4.2.3 and 4.2.4). The spring constant of the linear spring inserted in the tether is approximately 11.4 N/m.

The frequency of oscillation of the mass-spring mode of the vehicle and tether is given by:

$$f_m = \frac{1}{2\pi}\sqrt{\frac{k}{m}}, \tag{2.17}$$

where k is the tether spring constant and m is the vehicle mass. For the orbital case, the spring constant is:

$$k = \frac{EA}{L}, \tag{2.18}$$

where E is Young's modulus for the tether material, A is the tether cross sectional area, and L is the tether length. For the tether discussed by He [31], $EA = 5.3 \times 10^4$ N and with a sub-satellite mass of 1000 kg, the frequency of oscillation of the mass-spring mode for the orbital case is 0.025 Hz. In the laboratory, the value of the spring constant is 11.4 N/m and the vehicle mass is approximately 250 kg. Then, the frequency of oscillation is 0.034 Hz. The discrepancy in these values is related to the simulation of tether tension magnitude variations and will be explained further in Section 4.2.3.

The value of the micro-gravity field for the flight test and laboratory situations is

well known and will be derived in Chapter 3. For the orbital case, the micro-gravity acceleration is given by the acceleration generated by the gravity gradient force. As derived in Section 3.1.1, Equation 3.56 shows that the gravity gradient acceleration is:

$$g' = 3Ln^2. \tag{2.19}$$

For a 2000 m tether length and a nominal orbital rate (n) of 0.0012 rad/sec, the micro-gravity acceleration is 0.0082 m/sec^2. In the laboratory, the micro-gravity acceleration is simply the product of the sine of the table tilt angle and the value of the local acceleration of gravity. Equation 2.1 shows that the laboratory micro-gravity acceleration is equal to 0.008 m/sec^2. As a result, the micro-gravity field in the laboratory is approximately equal to the value of the orbital case.

The final scaling parameter introduced in Table 2.1 is the closed-loop system bandwidth. In the discussion of a one dimensional model, He [31] derives an estimate of the peak time (t_p) for a typical step response. He shows the peak time to be approximately:

$$t_p \cong 2\left(\frac{R_g^2\theta_r}{n^2LV_{max}}\right)^{1/3}, \tag{2.20}$$

where $R_g = \sqrt{\frac{I}{m}}$ is the radius of gyration for the vehicle, θ_r is the step size, and V_{max} is the slew rate limit of the attachment point. For a damped, second order system, it can be shown that:

$$t_p = \frac{\pi}{\omega_d}, \tag{2.21}$$

where $\omega_d = \omega_n\sqrt{1-\zeta^2}$ is the damped natural frequency, ω_n is the undamped natural frequency, and ζ is the damping ratio of the system. For $\zeta = \frac{2}{3}$,

$$\omega_n \approx \frac{4\omega_d}{3}. \tag{2.22}$$

Combining and rewriting Equations 2.20–2.22, it can be shown that:

$$\omega_n \cong \frac{2\pi}{3}\left(\frac{Ln^2mV_{max}}{I\theta_r}\right)^{1/3}. \tag{2.23}$$

Since $g' = 3Ln^2$ and $\omega_n = 2\pi f_n$, Equation 2.23 can be used to derive the approximate closed-loop system bandwidth (f_n) to be:

$$f_n \cong \frac{1}{3}\left(\frac{g' m V_{max}}{3I\theta_r}\right)^{1/3}. \tag{2.24}$$

For both the orbital and laboratory cases, $g' \approx 0.008$ m/sec^2, $\theta_r \approx 0.01$ rad (0.57 deg), and $V_{max} \approx 0.05$ m/sec. The mass for the orbital case is approximately 1000 kg and the central, principal moment of inertia for the vehicle is approximately 300 kg-m^2. Substituting these numbers into Equation 2.24 yields a closed-loop bandwidth of 0.12 Hz. In the laboratory, the vehicle mass is approximately 250 kg and the central, principal moment of inertia is 30 kg-m^2. These values yield an approximate closed-loop bandwidth of 0.16 Hz. These bandwidth values suggest that the response time of the current flight test configuration will be 33% slower than the laboratory simulator response time. As a result, when drawing conclusions about the flight test vehicle based on performance of the laboratory simulator, the above time scaling must be kept in mind. Also, in the simulation of tether tension variations, this bandwidth difference will result in laboratory frequencies (of the tension magnitude and direction variations) which are scaled relative to the expected orbital values (see Sections 4.2.3 and 4.2.4).

Chapter 3

Dynamic Equations and Control Algorithm

The development of an attitude control system for a generic satellite is dependent on the formulation of an accurate mathematical model which describes the significant dynamic behavior of the system. With this model in hand, the important natural dynamic characteristics can be derived and then an appropriate control algorithm can be designed. This chapter provides the detailed formulation of the system dynamic equations and attitude control algorithm as applied to the precision attitude control of tethered spacecraft. A brief discussion of the three dimensional (six degree of freedom) motion of a tethered satellite configuration will be followed by a detailed derivation of the in-plane orbital equations of motion. The equations of motion of the laboratory simulator will then be derived by exploring the effects of gravity and centrifugal gradients on orbiting spacecraft and setting the orbital rate to zero in the equations for the in-plane orbital case. Finally, the equations will be linearized and the control algorithm will be derived for the large angle slew maneuver and the long term, fine pointing control exercise.

3.1 Dynamic Equations

There are many discussions of the dynamics of tethered satellites in the open literature. The content of each of the studies ranges from the study of a relatively simple dumbbell with a massless, inextensible tether (see Stuiver [8] and Bainum and Kumar [9]), to studies of an extensible dumbbell (see, for instance, Paul [12], Pringle [14], Bainum, Harkness, and Stuiver [15], Stuiver and Bainum [16], and Singh [17]), to analysis of a massive extensible dumbbell (see Modi and Misra [18], Modi, Chang-Fu, Misra, and Xu [10], Beletskii and Levin [23], and Bainum, Diarra, and Kumar [24]), to the case of general spacecraft with flexible appendages (see Lips and Modi [26][27], and Misra and Modi [25]). Arnold [19] discusses many aspects of the behavior of long tethers in space and the two handbooks [40][41] published by the NASA Office of Space Flight provide an excellent reference for the basics of tethered satellite systems. Stephenson [45] discusses the computer simulation of a KITE implementation, including Space Shuttle and longitudinal tether dynamics. He [31] separately discusses the orbital dynamics, the attitude dynamics, and the dynamics of the tether, and then performs a computer simulation of the combined system. The conclusions that can be drawn based on these discussions are as follows:

1. For slow motions of the tether (ignoring the elastic properties of the tether) and for small oscillations about the nominal configuration (the tether aligned with the local vertical):

   (a) The out-of-plane pendular librations are decoupled from longitudinal motions and in-plane pendular librations.

   (b) The angular rate of in-plane and out-of-plane pendular librations are of the same order of magnitude as the orbital rate (i.e., $\sqrt{3}$ and 2 times orbital rate, respectively).

   (c) The in-plane and out-of-plane pendular libration modes have no natural damping.

   (d) The tether applies an external force to the sub-satellite which is much greater than other environmental disturbing forces (e.g., atmospheric drag).

2. For a tether modeled as a uniform continuum without bending resistance and assuming small perturbations from the nominal configuration:

   (a) Both the lowest order longitudinal oscillation frequency (mass-spring mode) and the lowest order lateral vibration frequency are much higher than the orbital rate.

   (b) The pendular libration modes are decoupled from the tether vibration modes.

   (c) The longitudinal tether oscillations are moderately well damped (due to stretching of the tether).

   (d) The lateral tether oscillations are not well damped and the only natural damping mechanism for lateral oscillations is the nonlinear coupling between lateral motion and longitudinal elongation.

3. For the rigid body rotation of a sub-satellite of a tethered satellite configuration:

   (a) Passively stabilized satellites with fixed tether attach points can provide undamped attitude regulation on the order of 1 deg.

   (b) Providing a mechanism to vary the tether attachment point with respect to the satellite mass center should be able to provide damped attitude regulation on the order of 1 arc-sec.

3.1.1 Orbit Plane Equations of Motion

The above conclusions suggest that a reasonable model for the planar dynamics of a tethered satellite can be derived by considering the motion in the orbit plane of the spacecraft. Therefore, the sub-satellite model will possess three degrees of freedom (two in translation and one in rotation). In addition, if it is assumed that the sub-satellite mass and the mass of the tether are much smaller than the mass of the parent spacecraft, then the center of mass of the complete constellation lies very close to the mass center of the parent spacecraft. Also, it can be assumed that the orbit of the parent and, therefore, the mass center of the constellation, is circular, with a constant

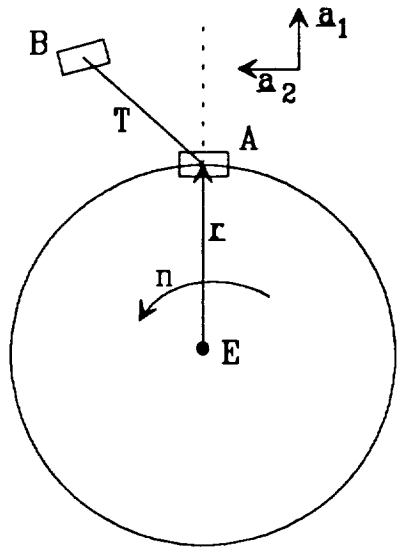

Figure 3.1: Schematic Diagram of Orbital Plane Motion

orbital rate. Finally, since the tether for an astrophysical pointing platform will be between 1-2 km long, the tether length is much smaller than the orbital radius (which will be on the order of 6500 km).

These assumptions serve as the starting point for the derivation of the orbit plane equations of motion for a tethered satellite, the derivation to be based upon Kane's Method of Formulating Dynamic Equations [46]. Figure 3.1 shows a schematic diagram of the system under consideration. Body **A** is the parent spacecraft, **T** is the tether, and body **B** represents the sub-satellite. The orbital rate is signified by n and is assumed constant for the shown circular orbit. The position vector from the attracting center, **E**, to the mass center, $\mathbf{A}^*$, of **A** is $\underline{\mathbf{r}}$. The magnitude of $\underline{\mathbf{r}}$ is constant and is represented by the equation

$$|\underline{\mathbf{r}}| = R_0. \tag{3.1}$$

The unit vectors $\underline{\mathbf{a}}_1$ and $\underline{\mathbf{a}}_2$ are mutually perpendicular and are fixed in body **A**. Vector $\underline{\mathbf{a}}_1$ is parallel to the local vertical axis and vector $\underline{\mathbf{a}}_2$ is parallel to the velocity vector of the mass center of body **A**. A unit vector, $\underline{\mathbf{a}}_3$, perpendicular to the orbit

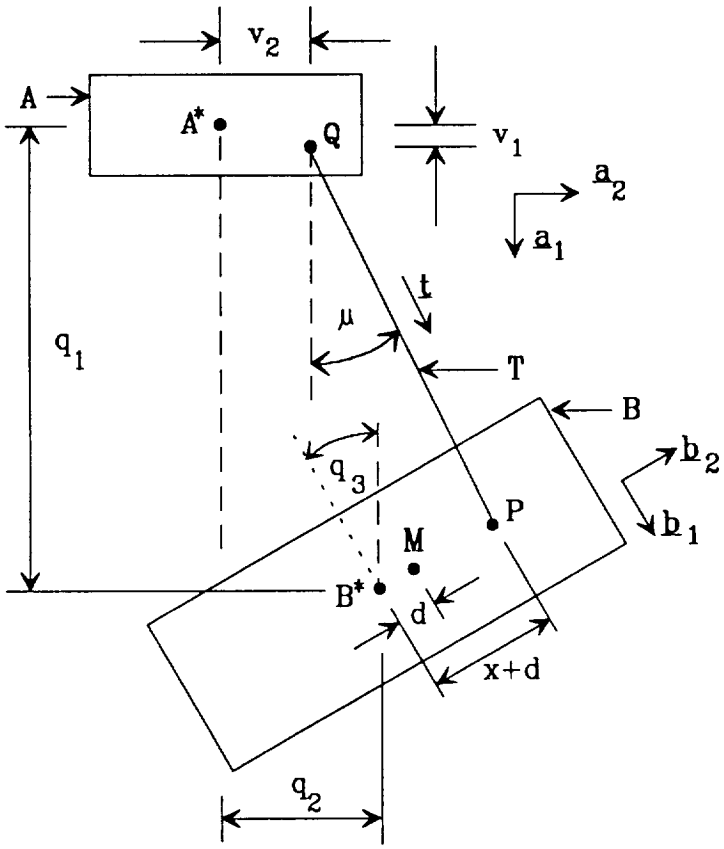

Figure 3.2: Geometry of Tethered Satellite Orbit Plane

plane, is given by

$$\underline{\mathbf{a}}_3 = \underline{\mathbf{a}}_1 \times \underline{\mathbf{a}}_2. \tag{3.2}$$

Figure 3.2 shows a close-up view of the tethered satellite. $\mathbf{B}^*$ is the center of mass of the sub-satellite, which has a mass of m_B. The position vector from $\mathbf{A}^*$ to $\mathbf{B}^*$ can be represented by (see Figure 3.2 for a graphical representation of q_1 and q_2)

$$\underline{r}^{A^*B^*} = q_1\underline{\mathbf{a}}_1 + q_2\underline{\mathbf{a}}_2. \tag{3.3}$$

The vectors $\underline{\mathbf{b}}_1$ and $\underline{\mathbf{b}}_2$ are mutually perpendicular unit vectors fixed in body $\mathbf{B}$, they are related to $\underline{\mathbf{a}}_1$ and $\underline{\mathbf{a}}_2$ by the values shown in Table 3.1, where $c_3 = \cos(q_3)$ and $s_3 = \sin(q_3)$. The angle q_3 characterizes the orientation of the sub-satellite, $\mathbf{B}$, relative to the parent spacecraft, $\mathbf{A}$.

	$\underline{\mathbf{a}}_1$	$\underline{\mathbf{a}}_2$
$\underline{\mathbf{b}}_1$	c_3	s_3
$\underline{\mathbf{b}}_2$	$-s_3$	c_3

Table 3.1: Relationship Between Unit Vectors Fixed in **A** and **B**

Kinematic Equations

The kinematic expressions of interest in the dynamic analysis include the inertial angular velocity and angular acceleration of **B**, the inertial velocity and acceleration of **B***, and the inertial velocity of point **P**, the attach point of the tether on the sub-satellite. The angular velocity of **B** is given by

$$\underline{\omega}^B = \underline{\omega}^A + {}^A\underline{\omega}^B, \tag{3.4}$$

where

$$\underline{\omega}^A = n\underline{\mathbf{a}}_3, \tag{3.5}$$

and

$${}^A\underline{\omega}^B = \dot{q}_3\underline{\mathbf{a}}_3. \tag{3.6}$$

If the generalized speed u_3 is introduced as

$$u_3 \equiv \dot{q}_3, \tag{3.7}$$

then Equation 3.4 can be rewritten (making use of Equations 3.5, 3.6, and 3.7) as

$$\underline{\omega}^B = (n + u_3)\underline{\mathbf{a}}_3. \tag{3.8}$$

The angular acceleration of **B** is

$$\underline{\alpha}^B = \frac{d}{dt}\underline{\omega}^B = \dot{u}_3\underline{\mathbf{a}}_3. \tag{3.9}$$

The velocity of **B*** is given by

$$\underline{v}^{B^*} = \underline{v}^{\overline{A}} + {}^A\underline{v}^{B^*}, \tag{3.10}$$

where ${}^A\underline{v}^{B^*}$ is the velocity of $\mathbf{B}^*$ in body $\mathbf{A}$, and $\underline{v}^{\overline{A}}$ is the velocity of point $\overline{A}$, the point of $\mathbf{A}$ which coincides with $\mathbf{B}^*$ at the instant under consideration. Further,

$$\underline{v}^{\overline{A}} = \underline{v}^{A^*} + \underline{\omega}^A \times \underline{r}^{A^*B^*}. \tag{3.11}$$

From the assumption of a circular orbit,

$$\underline{v}^{A^*} = nR_0\underline{\mathbf{a}}_2. \tag{3.12}$$

In addition, the velocity of $\mathbf{B}^*$ in $\mathbf{A}$ is

$${}^A\underline{v}^{B^*} = \dot{q}_1\underline{\mathbf{a}}_1 + \dot{q}_2\underline{\mathbf{a}}_2. \tag{3.13}$$

Introducing two additional generalized speeds u_1 and u_2 as

$$u_1 \equiv \dot{q}_1, \tag{3.14}$$

$$u_2 \equiv \dot{q}_2, \tag{3.15}$$

and combining Equations 3.10–3.13 and 3.3 with Equations 3.14 and 3.15, one finds that

$$\underline{v}^{B^*} = (u_1 - nq_2)\underline{\mathbf{a}}_1 + [u_2 + n(R_0 + q_1)]\underline{\mathbf{a}}_2. \tag{3.16}$$

The acceleration of $\mathbf{B}^*$ can be written

$$\underline{a}^{B^*} = \underline{a}^{\overline{A}} + {}^A\underline{a}^{B^*} + 2\underline{\omega}^A \times {}^A\underline{v}^{B^*}, \tag{3.17}$$

where ${}^A\underline{a}^{B^*}$ is the acceleration of $\mathbf{B}^*$ in $\mathbf{A}$ and

$$\underline{a}^{\overline{A}} = \underline{a}^{A^*} + \underline{\omega}^A \times (\underline{\omega}^A \times \underline{r}^{A^*B^*}). \tag{3.18}$$

Furthermore,

$$\underline{a}^{A^*} = -n^2R_0\underline{\mathbf{a}}_1. \tag{3.19}$$

From Equations 3.13, 3.14, and 3.15, the acceleration of $\mathbf{B}^*$ in $\mathbf{A}$ can be expressed as

$${}^A\underline{a}^{B^*} = \dot{u}_1\underline{\mathbf{a}}_1 + \dot{u}_2\underline{\mathbf{a}}_2. \tag{3.20}$$

Hence, from Equations 3.17–3.20,

$$\underline{a}^{B^*} = [\dot{u}_1 - 2nu_2 - n^2(R_0 + q_1)]\underline{\mathbf{a}}_1 + (\dot{u}_2 - n^2q_2 + 2nu_1)\underline{\mathbf{a}}_2. \tag{3.21}$$

i	$\underline{\omega}_i^B$	$\underline{v}_i^{B^*}$	$\underline{v}_i^P$
1	0	$\underline{\mathbf{a}}_1$	$\underline{\mathbf{a}}_1$
2	0	$\underline{\mathbf{a}}_2$	$\underline{\mathbf{a}}_2$
3	$\underline{\mathbf{a}}_3$	0	$-(x+d)(c_3\underline{\mathbf{a}}_1 + s_3\underline{\mathbf{a}}_2)$

Table 3.2: Partial Angular Velocities and Partial Velocities

The velocity of the tether attach point on the sub-satellite, $\underline{v}^P$, is given by

$$\underline{v}^P = \underline{v}^{B^*} + \underline{\omega}^B \times (x+d)\underline{\mathbf{b}}_2 + {}^B\underline{v}^P. \tag{3.22}$$

In Equation 3.22, ${}^B\underline{v}^P$ is the velocity of **P** with respect to the sub-satellite, and $(x+d)\underline{\mathbf{b}}_2$ is the position vector from $\mathbf{B}^*$ to **P**. The distance x represents the position of the tether attachment point with respect to the assumed mass center of **B**, point **M** in Figure 3.2, and d is the distance between the actual mass center, $\mathbf{B}^*$, and the assumed mass center, **M**. The distance x can be varied by the actuator mounted on board the sub-satellite (see Section 2.1.3) and is, therefore, the control input. The velocity of **P** in **B** is given by

$${}^B\underline{v}^P = \dot{x}\underline{\mathbf{b}}_2. \tag{3.23}$$

Equations 3.16, 3.22, and 3.23, yield

$$\begin{aligned} \underline{v}^P &= [u_1 - nq_2 - (n+u_3)(x+d)c_3 - \dot{x}s_3]\underline{\mathbf{a}}_1 + \\ &\quad [u_2 + n(R_0+q_1) - (n+u_3)(x+d)s_3 + \dot{x}c_3]\underline{\mathbf{a}}_2. \end{aligned} \tag{3.24}$$

Partial velocities and partial angular velocities associated with the generalized speeds u_i, $i = 1,2,3$, can be formed by inspection of Equations 3.8, 3.16, and 3.24. For convenience, the results are summarized in Table 3.2.

Generalized Inertia Forces

The generalized inertia forces for the sub-satellite can be found from the following expression

$$F_i^* = \underline{v}_i^{B^*} \cdot \underline{R}^B + \underline{\omega}_i^B \cdot {}^B\underline{T}^*, \quad i = 1,2,3. \tag{3.25}$$

$\underline{R}^B$ and ${}^B\underline{T}^*$ are the inertia force and inertia torque for **B**, respectively. The inertia force is given by

$$\underline{R}^B = -m_B \underline{a}^{B^*}, \tag{3.26}$$

and the inertia torque is

$${}^B\underline{T}^* = -\underline{\alpha}^B \cdot \underline{I} - \underline{\omega}^B \times \underline{I} \cdot \underline{\omega}^B, \tag{3.27}$$

where $\underline{I}$ is the central inertia dyadic of **B**. In view of Equations 3.8 and 3.9, Equation 3.27 reduces to

$${}^B\underline{T}^* = -I_3 \dot{u}_3 \underline{\mathbf{a}}_3, \tag{3.28}$$

where I_3 is the central principal moment of inertia of **B** for a line parallel to $\underline{\mathbf{a}}_3$. Therefore, combining the values of the partial velocities shown in Table 3.2 and the expressions in Equations 3.21, 3.25, and 3.28, one finds that the generalized inertia forces for the sub-satellite are

$$F_1^* = -m_B[\dot{u}_1 - 2nu_2 - n^2(R_0 + q_1)], \tag{3.29}$$

$$F_2^* = -m_B(\dot{u}_2 + 2nu_1 - n^2 q_2), \tag{3.30}$$

$$F_3^* = -I_3 \dot{u}_3. \tag{3.31}$$

Gravitational Forces

The set of gravitational forces acting on the sub-satellite of a tethered satellite constellation can be replaced with a force acting at the sub-satellite mass center and a couple Kane, Likins, and Levinson [47], have developed a convenient methodology for determining the magnitude and direction of the gravity force and the torque of the couple, called the gravity torque. The gravity force for body **B** is given by

$$\underline{F}_g = -G \frac{m_E m_B}{|\underline{r}^{EB^*}|^3} \underline{r}^{EB^*}, \tag{3.32}$$

where G is the universal gravitational constant, m_E is the mass of the Earth, and $\underline{r}^{EB^*}$ is the position vector from the center of the Earth to **B**. From Equations 3.1 and 3.3,

$$\underline{r}^{EB^*} = (R_0 + q_1)\underline{\mathbf{a}}_1 + q_2 \underline{\mathbf{a}}_2. \tag{3.33}$$

Consequently,

$$|\underline{r}^{EB^*}|^{-3} = R_0^{-3}\left[\left(1+\frac{q_1}{R_0}\right)^2+\left(\frac{q_2}{R_0}\right)^2\right]^{-3/2}. \tag{3.34}$$

Since,

$$R_0 \gg q_1, \tag{3.35}$$

$$R_0 \gg q_2, \tag{3.36}$$

Equation 3.34 can be replaced (by dropping terms nonlinear in q_1/R_0 and q_2/R_0) with

$$|\underline{r}^{EB^*}|^{-3} \approx R_0^{-3}\left(1-3\frac{q_1}{R_0}\right). \tag{3.37}$$

Combining Equations 3.32, 3.33, and 3.37 one finds that

$$\underline{F}_g \approx -G\frac{m_E m_B}{R_0^2}\left(1-3\frac{q_1}{R_0}\right)\left[\left(1+\frac{q_1}{R_0}\right)\underline{\mathbf{a}}_1+\frac{q_2}{R_0}\underline{\mathbf{a}}_2\right]. \tag{3.38}$$

For a circular orbit,

$$n^2 = G\frac{m_E}{R_0^3}, \tag{3.39}$$

and, linearizing once more, one obtains

$$\underline{F}_g \approx -m_B n^2\left[(R_0-2q_1)\underline{\mathbf{a}}_1+q_2\underline{\mathbf{a}}_2\right]. \tag{3.40}$$

The moment about $\mathbf{B}^*$ of the gravitational forces exerted on $\mathbf{B}$ by $\mathbf{E}$ can be approximated by [47]

$$\underline{M}_g \approx 3\frac{Gm_E}{|\underline{r}^{EB^*}|^3}\,\underline{\mathbf{d}}\times\underline{I}\cdot\underline{\mathbf{d}}, \tag{3.41}$$

where $\underline{\mathbf{d}}$ is a unit vector pointing from the center of the Earth to $\mathbf{B}^*$. The vector $\underline{\mathbf{d}}$ can be written

$$\underline{\mathbf{d}} = \frac{\underline{r}^{EB^*}}{|\underline{r}^{EB^*}|}, \tag{3.42}$$

or, after linearization,

$$\underline{\mathbf{d}} = \underline{\mathbf{a}}_1+\frac{q_2}{R_0}\underline{\mathbf{a}}_2. \tag{3.43}$$

Equations 3.41 and 3.34 lead to

$$\underline{M}_g = 3\,\frac{Gm_E}{R_0^3}\left(1-3\frac{q_1}{R_0}\right)(I_2-I_1)\,(\underline{\mathbf{d}}\cdot\underline{\mathbf{b}}_1)\,(\underline{\mathbf{d}}\cdot\underline{\mathbf{b}}_2)\,\underline{\mathbf{a}}_3, \tag{3.44}$$

where I_1 and I_2 are the central principal moments of inertia of **B** for lines parallel to $\underline{\mathbf{b}}_1$ and $\underline{\mathbf{b}}_2$, respectively. Combining Equations 3.39 and 3.44, one arrives at

$$\underline{M}_g = 3n^2 \left[\left(1 - 3\frac{q_1}{R_0} \right) c_3 s_3 + \frac{q_2}{R_0}(c_3^2 - s_3^2) \right] (I_2 - I_1)\underline{\mathbf{a}}_3. \tag{3.45}$$

Generalized Active Forces

The generalized active forces depend on gravitational forces discussed above and on the tether forces which act at the tether attach point. The latter forces are quite complicated, and their mathematical description is dependent on the model chosen to describe the dynamics of the tether. He [30] develops a mathematical model to describe the longitudinal and lateral motions of long tethers in space. For present purposes, it is sufficient to note that tether forces exist and that they can be represented by a force $\underline{F}_t$ applied at **P**. The generalized active forces then are given by

$$F_i = \underline{v}_i^{B^*} \cdot \underline{F}_g + \underline{\omega}_i^B \cdot \underline{M}_g + \underline{v}_i^P \cdot \underline{F}_t, \quad i = 1,2,3. \tag{3.46}$$

Making use of the partial velocities in Table 3.2 and Equations 3.40 and 3.45, one obtains

$$F_1 = -m_B n^2 [R_0 - 2(L + q_1)] + \underline{F}_t \cdot \underline{\mathbf{a}}_1 \tag{3.47}$$

$$F_2 = -m_B n^2 q_2 + \underline{F}_t \cdot \underline{\mathbf{a}}_2 \tag{3.48}$$

$$F_3 = 3n^2 \left[\left(1 - 3\frac{q_1}{R_0} \right) c_3 s_3 + \frac{q_2}{R_0}(c_3^2 - s_3^2) \right] (I_2 - I_1) - (x + d)\underline{F}_t \cdot \underline{\mathbf{b}}_1. \tag{3.49}$$

Orbital Equations of Motion

The equations of motion of the sub-satellite can be formualted by writing

$$F_i^* + F_i = 0, \quad i = 1,2,3, \tag{3.50}$$

where F_i^* and F_i are the previously derived generalized inertia forces and generalized active forces. Equations 3.29–3.31 and 3.47–3.49 yield

$$\dot{u}_1 = 2nu_2 + 3n^2 q_1 + \frac{1}{m_B}\underline{F}_t \cdot \underline{\mathbf{a}}_1 \tag{3.51}$$

$$\dot{u}_2 = -2nu_1 + \frac{1}{m_B}\underline{F}_t \cdot \underline{\mathbf{a}}_2 \tag{3.52}$$

$$\dot{u}_3 = 3n^2\left(\frac{I_2 - I_1}{I_3}\right)\left[\left(1 - 3\frac{q_1}{R_0}\right)c_3 s_3 + \frac{q_2}{R_0}(c_3^2 - s_3^2)\right] - \frac{x+d}{I_3}\underline{F}_t \cdot \underline{\mathbf{b}}_1. \tag{3.53}$$

Equations 3.51 and 3.52 can be recognized as the Euler-Hill Equations [31] governing the mass center motion of a spacecraft relative to an orbiting reference frame. The term $3n^2q_1$ in Equation 3.51, composed of two-thirds gravity and one-third centrifugal acceleration, as can be seen from Equations 3.21 and 3.40, is referred to as the micro-gravity acceleration and is commonly denoted by g'. In its nominal configuration, the sub-satellite will be positioned relative to the parent such that

$$q_1 \approx L, \tag{3.54}$$

and

$$q_2 = q_3 = 0. \tag{3.55}$$

Under these circumstances, expressed as

$$g' \approx 3n^2L. \tag{3.56}$$

Equation 3.53 shows that the effect of tether forces on the rotational motion of the sub-satellite vanishes unless there is an offset between the tether attachment and the center of mass of the satellite, i.e., unless $(x + d) \neq 0$. Equivalently, it reveals that one can affect the orientation of the sub-satellite by varying the position of the tether attachment point with respect to the mass center location of the sub-satellite. Therefore, with appropriate control logic, one can position the tether attach point relative to the sub-satellite mass center in real time, in such a way as to control the orientation of the sub-satellite.

3.1.2 Laboratory Simulator Equations of Motion

As discussed in Chapter 2, the laboratory simulator is an air-bearing supported vehicle. The vehicle consists of the hardware necessary to implement the attitude control

of the vehicle. The simulator possesses three degrees of freedom (one in rotation and two in translation) and it exhibits essentially friction-free motion in the plane of suspension. In addition, it is attached to a tether dynamics simulator, located in the laboratory, which is used to simulate the behavior of a long, space-based tether. As a result, save the orbital motion, the laboratory simulator possesses the same degrees of freedom and essentially the same dynamic characteristics as the orbital model of a tethered satellite discussed previously. The differences in the dynamic behavior of two systems, which arise from the air-bearing suspension and the shorter laboratory tether length, are negligible compared to the macroscopic behavior of the systems. The air-bearing suspension forces have been shown to be small (see Section 2.1.1), and the shorter tether length will only increase the pendular natural frequency. However, the increase in the natural frequency is so small that the laboratory pendular frequency is smaller than the expected closed-loop bandwidth of the system. Therefore, the kinematic equations for the simulator can be determined simply by setting the orbital rate to zero in the previously described development. The laboratory generalized active forces are a result of the simulated micro-gravity acceleration, the interaction of the air-bearing suspension with the vehicle, and the tether dynamics (which is the sum of the natural laboratory tether dynamics and the additional contribution due to the motion of the tether dynamics simulator).

Generalized Inertia Forces

The generalized inertia forces for the laboratory simulator can be determined simply by setting the orbital rate to zero in Equations 3.29–3.31. As a result, for the laboratory case

$$F_1^* = -m_B \dot{u}_1, \tag{3.57}$$

$$F_2^* = -m_B \dot{u}_2, \tag{3.58}$$

$$F_3^* = -I_3 \dot{u}_3. \tag{3.59}$$

Generalized Active Forces

The generalized active forces for the laboratory simulator result from the combination of forces applied to the air-bearing vehicle by the micro-gravity field, the air cushion, and the tether. Therefore, for the system in the laboratory, the generalized active forces result from the equations

$$F_i = \underline{v}_i^{B^*} \cdot (\underline{F}_g + \underline{F}_a) + \underline{\omega}_i^B \cdot \underline{T}_a + \underline{v}_i^P \cdot \underline{F}_t, \quad i = 1,2,3, \tag{3.60}$$

where $\underline{F}_g$ is the resultant force from the simulated micro-gravity field, $\underline{F}_a$ and $\underline{T}_a$ are the force applied at the mass center and a moment about the mass center of the forces exerted by the air cushion on the vehicle, and $\underline{F}_t$ is the force exerted by the tether acting on the sub-satellite at **P**.

The micro-gravity field is simulated in the laboratory by tilting the plane of suspension of the air-bearing vehicle so that it is not perpendicular to the local gravity vector (see Figure 2.2). The level of micro-gravity acceleration is adjusted by varying the tilt between the local gravity vector and the plane of the air cushion. The desired tilt angle is that angle which results in the same micro-gravity field as would be found in the orbital case (for the specific tether length and orbital rate). Therefore, the force on the laboratory sub-satellite due to the micro-gravity acceleration is

$$\underline{F}_g = m_B g' \underline{\mathbf{a}}_1. \tag{3.61}$$

The forces exerted on the sub-satellite by the air-bearing suspension system can be replaced with a single force acting at the mass center of the vehicle and a couple. The magnitude and direction of the force and the torque of the couple have been shown by Rehsteiner [48] to be proportional to the mass center velocity and vehicle angular velocity, respectively. As a consequence, the resultant force can be expressed as

$$\underline{F}_a = -b_l \underline{v}^{B^*} = -b_l(u_1 \underline{\mathbf{a}}_1 + u_2 \underline{\mathbf{a}}_2), \tag{3.62}$$

where b_l is the linear damping coefficient for the air cushion. In addition, the torque of the couple applied to the air-bearing vehicle can be expressed as

$$\underline{T}_a = -b_r \underline{\omega}^B = -b_r u_3 \underline{\mathbf{a}}_3, \tag{3.63}$$

where b_r is the rotational damping coefficient for the air cushion (see Section 2.1.1 for a detailed discussion and evaluation of b_l and b_r).

The tether in the laboratory consists of a short piece of Spectra tether material and a linear spring. The spring serves to make the short laboratory tether more compliant so that small tether attach point motions will not generate large tension variations. In addition, since a 2 km long tether will be considerably more compliant than a 2 m piece of the same material, the spring also serves to make the laboratory tether behave more like the expected orbital tether. As a result, a good, relatively simple model of the laboratory tether consists of a spring–damper system whose line of action is along the tether direction. This model ignores the longitudinal and lateral dynamics of the short tether material, which are negligible compared with the behavior of the spring. The line of action of the tether is given by the vector $\underline{t}$ shown in Figure 3.2 and is equal to

$$\underline{t} = \frac{\underline{p}^{QP}}{|\underline{p}^{QP}|} = c_\mu \underline{\mathbf{a}}_1 + s_\mu \underline{\mathbf{a}}_2, \tag{3.64}$$

where $\underline{p}^{QP}$ is the position vector from the tether attach point on the parent, $\mathbf{Q}$, to the tether attach point on the sub-satellite, $\mathbf{P}$, c_μ and s_μ represent $\cos(\mu)$ and $\sin(\mu)$, respectively, and μ is the angle between the tether and the local vertical. As shown in Figure 3.2, the vector $\underline{p}^{QP}$ is given by

$$\underline{p}^{QP} = [q_1 - v_1 - (x+d)s_3]\underline{\mathbf{a}}_1 + [q_2 - v_2 + (x+d)c_3]\underline{\mathbf{a}}_2, \tag{3.65}$$

where v_1 and v_2 are offsets from $\mathbf{Q}$ to the center of mass of $\mathbf{A}$, which is the nominal attach point on the parent spacecraft. These linear dimensions can be functions of time so as to impose variations in magnitude and direction of the tether force applied to the sub-satellite. These variations can be used to simulate the longitudinal and lateral dynamics of a long space tether in the laboratory (see Section 4.2.5). The magnitude of the tether tension is the sum of the effects of the linear spring and linear damper and can be expressed as

$$|\underline{F}_t| = k(|\underline{p}^{QP}| - L) + b_t \frac{d}{dt}\left(|\underline{p}^{QP}|\right), \tag{3.66}$$

where L is the unstretched length of the spring, k is the linear spring constant, and b_t is

the linear damping coefficient of the damper model. Therefore, from Equations 3.64–3.66, the tether force vector is given by

$$\underline{F}_t = -|\underline{F}_t|\underline{t}. \tag{3.67}$$

The generalized active forces for the laboratory simulator can be determined by using Equation 3.60 in addition to Equations 3.61–3.63, 3.67, and the partial velocity values shown in Table 3.2. The generalized active forces are given by

$$F_1 = -|\underline{F}_t|c_\mu + m_B g' - b_l u_1, \tag{3.68}$$

$$F_2 = -|\underline{F}_t|s_\mu - b_l u_2, \tag{3.69}$$

$$F_3 = (x+d)|\underline{F}_t|(c_\mu c_3 + s_\mu s_3) - b_r u_3. \tag{3.70}$$

Laboratory Equations of Motion

The equations of motion for the laboratory simulator can be derived by setting

$$F_i^* + F_i = 0, \quad i = 1,2,3, \tag{3.71}$$

and by making use of the previously derived laboratory simulator generalized inertia forces and laboratory simulator generalized active forces. Combining Equations 3.57–3.59, Equations 3.68–3.70, and Equations 3.71, one obtains the laboratory simulator equations of motion,

$$\dot{u}_1 = g' - \frac{1}{m_B}\left(|\underline{F}_t|c_\mu + b_l u_1\right), \tag{3.72}$$

$$\dot{u}_2 = -\frac{1}{m_B}\left(|\underline{F}_t|s_\mu + b_l u_2\right), \tag{3.73}$$

$$\dot{u}_3 = \frac{1}{I_3}\left[|\underline{F}_t|(x+d)(c_\mu c_3 + s_\mu s_3) - b_r u_3\right]. \tag{3.74}$$

Equations 3.72 and 3.73 are the differential equations which determine the linear motion of the laboratory simulator in the directions parallel to and perpendicular to the local vertical direction, respectively. Equation 3.74 is the differential equation which governs the rotational behavior of the laboratory vehicle. These three equations, along with the previously declared definitions

$$\dot{q}_i = u_i, \quad i = 1,2,3, \tag{3.75}$$

fully determine the motion of the generalized coordinates for the laboratory simulator. Appendix A.2 contains a FORTRAN subroutine which implements the six, first order, differential equations which describe the simulator motion and which can be used in conjunction with a numerical differential equation solver to numerically solve for the laboratory vehicle motion.

3.1.3 Linearized Equations for Laboratory Simulator

The equations, 3.72–3.74 and 3.75, are a set of six, coupled, nonlinear, first order differential equations which describe the motion of the laboratory simulator under the influence of the previously described modeled forces. In order to design a linear control law which makes use of the results of linear system theory, the nonlinear differential equations need to be converted to an approximate linear form. To that end, the angle, μ, that the tether makes with the local vertical is regarded as very small in the absence of large, unmodeled transverse forces. For present purposes, μ is assumed to be zero, so that the following relations become valid:

$$c_\mu = 1, \tag{3.76}$$

$$s_\mu = 0. \tag{3.77}$$

Furthermore, the tether tension magnitude can be split into a nominal, constant value and a small, zero mean variation superimposed on the nominal value. Therefore, the tension magnitude can be represented by

$$|\underline{F}_t| = F_0 + dF. \tag{3.78}$$

From Equation 3.72, the value of the nominal tether tension magnitude, F_0, is equal to the value of force necessary to balance the micro-gravity field. As a result,

$$F_0 = m_B g'. \tag{3.79}$$

In addition, it can be assumed that knowledge of the mass center location is sufficiently accurate that control torque generation will not be affected by any residual misalignment. As a result, it can be assumed (for now) that

$$d = 0. \tag{3.80}$$

Finally, it will be assumed that the torque applied to the simulator through the air-bearing suspension is very small in comparison to the control torque. Combining Equations 3.74–3.78 and 3.80, the rotational equation of motion can be shown to be

$$\ddot{q}_3 = \frac{F_0 x}{I_3}\left(1 + \frac{dF}{F_0}\right)\cos q_3. \tag{3.81}$$

For purposes of control law design, it is assumed that q_3 is small and that the tension variations are small compared with the nominal value of the tension magnitude (i.e., $F_0 \gg dF$). In addition, if q and I are defined as

$$q \equiv q_3, \tag{3.82}$$

$$I \equiv I_3, \tag{3.83}$$

in order to simplify notation, the following equation is the approximate, linear, differential equation of rotational motion for the laboratory sub-satellite:

$$\ddot{q} = \frac{F_0}{I}x. \tag{3.84}$$

Here x is the control input and q is the orientation angle of the vehicle (the variable to be controlled). For instances when either q is not small or when dF is on the same order of magnitude as F_0, the control algorithm can calculate the desired offset, x_d, and then obtain the actual offset, x, by scaling x_d as follows (see Lemke [42])

$$x = \frac{x_d}{\left(1 + \frac{dF}{F_0}\right)\cos q}. \tag{3.85}$$

The goal of the control algorithm will be to determine the position of the attach point with respect to the center of mass of the vehicle as a function of time. Equation 3.84 will serve as the model of the plant. Control algorithms for large angle slewing and high accuracy pointing will be developed in the following sections.

3.2 Control Law Development

The attitude control problem for a tethered astrophysical pointing platform can be broken down into two main tasks: large angle slew capability (on the order of ± 30 deg)

in order to quickly change from one target to another over the course of an orbit and long term, high accuracy (on the order of 1 arcsec) pointing in order to provide a stable platform for data collection. In order to exhibit large angle slew capability, the control system must show that sufficiently large and accurate control torques can be generated as required in order to drive the necessary attitude motion of the satellite. The task for long term, high accuracy pointing is to show that the control system can reject disturbances (both environmental and modeling errors) to the level that they will have a sufficiently small effect on the attitude of the satellite. Since these tasks are slightly different, two distinct control algorithms have been designed to handle the special needs of each task. In the case of the large angle slew maneuver, the control algorithm must provide sufficient phase lead while being careful not to amplify the sensor noise unnecessarily. For the high accuracy, long term pointing case, the DC gain of the control algorithm must be extremely high in order to reject the effects of disturbances. The current work considers the control law development for the pitch dynamics of a tethered sub-satellite. For a discussion and simulation of the full six degree of freedom attitude control algorithm for tethered satellites, the reader is referred to the work undertaken by He [31]. The current work serves to verify the simulation results obtained by He for tethered satellite pitch dynamics.

3.2.1 Large Angle Slew

In order to design a control law for the large angle slew maneuver, it is necessary to convert the model of the plant (Equation 3.84) into the equivalent Z-plane representation. Taking the Laplace Transform of Equation 3.84 yields (assuming zero initial conditions):

$$Q(s) = \frac{F_0}{Is^2} X(s), \tag{3.86}$$

where s is the Laplace Transform variable and $Q(s)$ and $X(s)$ are the Laplace Transforms of the vehicle orientation and attach point position, respectively. Taking the Z-transform of Equation 3.86 (see Franklin and Powell [50]) yields:

$$Q(z) = \frac{F_0 T^2}{2I} \frac{z+1}{(z-1)^2} X(z) = F_0 G(z) X(z), \tag{3.87}$$

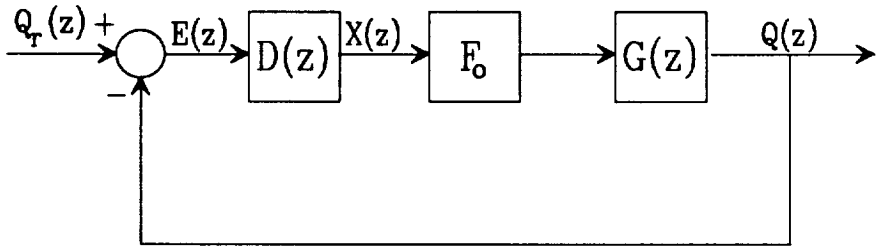

Figure 3.3: Large Angle Slew Control Block Diagram

where z is the Z-transform variable, T is the sample time, $G(z)$ is the Z-transform transfer function from applied control torque to vehicle orientation, and $Q(z)$ and $X(z)$ are the Z-transforms of the vehicle orientation and attach point position, respectively. The values of F_0 and I for the laboratory simulator are discussed in Section 2.3 and are equal to 2 N and 30 kg-m^2, respectively. The value of the sample time, T, for the candidate design is .5 sec which corresponds to a 2 Hz sample frequency.

The concept driving the control algorithm design is summarized in Figure 3.3. A measurement of the vehicle orientation is compared with a desired orientation and the error is formed. The control law, $D(z)$, takes this error and calculates the necessary attach point position in order that the vehicle orientation will follow the desired path. The digital compensator will take the form of a digital filter which will modify the open-loop dynamics in such a way as to affect satisfactory closed-loop performance.

The model of the rotational motion of the sub-satellite, $G(z)$, can be recognized as the digital equivalent to a continuous simple double integrator. As a result, it is clear that the compensator must provide phase lead in order to stabilize the open-loop system. In addition, to help in the rejection of unmodeled and environmental disturbances, it is fortuitous to include integral control. As a result, the control law which will make up the digital filter $D(z)$ will have the following form:

$$(1 - bz^{-1})X(z) = \left[K(1 - az^{-1}) + \frac{K_i}{1 - z^{-1}}\right] E(z), \tag{3.88}$$

where K is the control gain, K_i is the integral gain, and a and b are the zero and

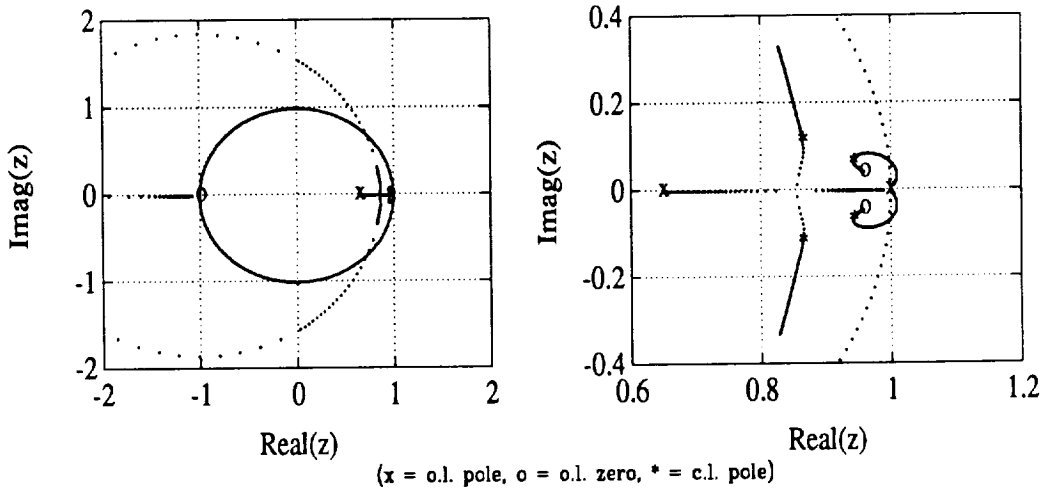

Figure 3.4: Large Angle Slew Root Locus

pole, respectively, associated with the lead compensator. Rearranging terms, the compensator transfer function can be shown to equal:

$$D(z) = K\frac{\left(1+\frac{K_i}{K}\right)z^2-(a+1)z+a}{(z-1)(z-b)}. \tag{3.89}$$

Choosing values for the lead compensator zero and pole and the integral gain which balance the speed of response of the system while filtering the noise in the measurement, yields the following values:

$$a = 0.925, \tag{3.90}$$

$$b = 0.65, \tag{3.91}$$

$$\frac{K_i}{K} = 0.0035. \tag{3.92}$$

With these values chosen, the effect that the gain K has on the location of the poles of the closed-loop system can be derived by drawing a root locus of the system for the following standard form:

$$1+K\left[\frac{1.0035(z-0.9591)^2+(0.0426)^2}{(z-1)(z-0.65)}\right]\left[\frac{0.00833(z+1)}{(z-1)^2}\right]=0. \tag{3.93}$$

Figure 3.4 shows the root locus versus K for the system description given by Equation 3.93. The root locus shows that, for zero gain, the closed-loop poles start at the open-loop poles of the system, $z = 1, 1, 1, 0.65$, and approach the open-loop

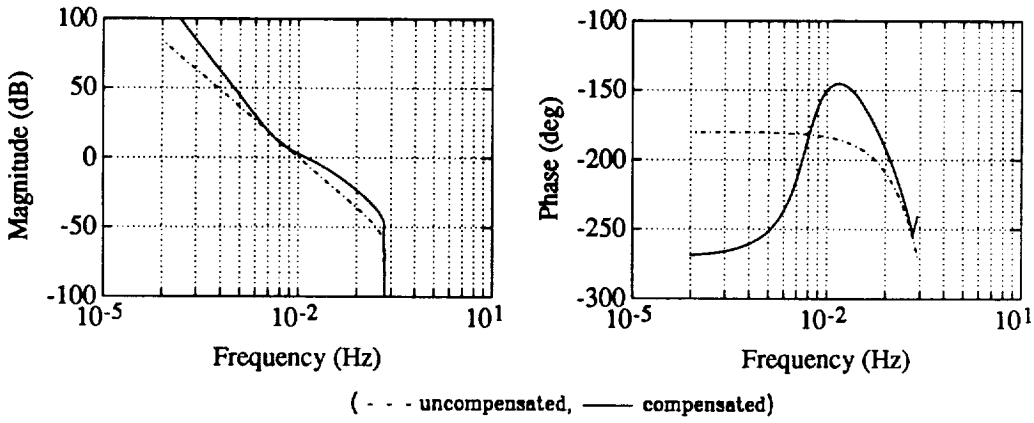

Figure 3.5: Large Angle Slew Open-Loop Bode Plot

zeros, $z = -1$, $0.9591 \pm 0.0426j$, as the gain is increased. Choosing the value of K to be 4, yields closed-loop pole locations (shown as asterisks in Figure 3.4) to be $z = 0.9431 \pm 0.0645j$, $0.8651 \pm 0.1155j$ (which correspond to poles with damping ratios of approximately 0.8 and 0.75, respectively). Figure 3.5 shows an open-loop Bode plot of both the uncompensated system dynamics as well as the compensated system. For both the magnitude and phase plots, the dashed line represents the uncompensated system and the solid line represents the compensated dynamics. These plots show that the compensator increased the low frequency gain, modified the slope of the 0 dB crossover from a slope of -40 dB/decade to approximately -20 dB/decade, increased the crossover frequency from 0.01 Hz to 0.018 Hz, and added a significant amount of phase lead near the crossover frequency (so that the phase margin is 35 deg). Therefore, the control law is shown to result in stable, well damped, closed-loop pole locations and to result in a desirable open-loop transfer function (as judged from the Bode plot) for the given system model. The bandwidth for this control algorithm is approximately 0.02 Hz.

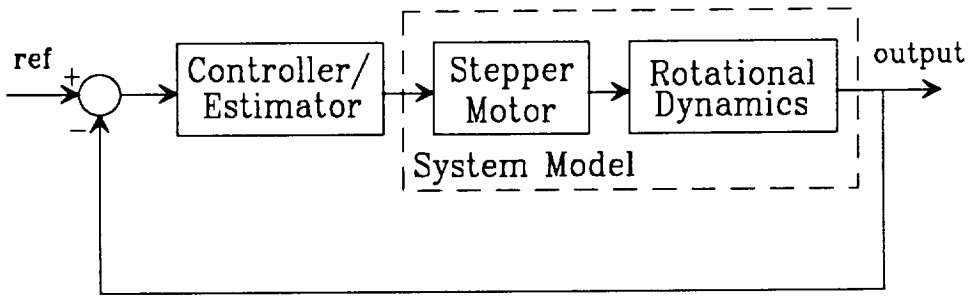

Figure 3.6: Fine Pointing Block Diagram

3.2.2 Fine Pointing

Control Law

As stated previously, in order to design a high accuracy, long term, fine pointing attitude regulation system, the DC gain of the control algorithm must be extremely high in order to reject disturbances. In order to design such a control law, a highly accurate system model must be available. A conceptual block diagram of the feedback control system is shown in Figure 3.6. The figure shows that the system model consists of both the rotational dynamics of the sub-satellite and the actuator dynamics (i.e., the stepper motor). In the laboratory, the linearized, differential equation which governs the rotational dynamics of the air-bearing vehicle has been derived previously and is shown in Equation 3.84 to be a simple, double integrator.

As shown in Figure 3.6, the actuator for the closed-loop system is a stepper motor which drives a positioning table. The stepper motor is a constant velocity device and is, therefore, nonlinear and difficult to model exactly. Figure 3.7 shows a typical closed-loop attach point position path. The position of the attach point may change during each sample period, but the magnitude of the attach point velocity is always the same. Because of the nature of the motion, a simple first order lag has been used to describe the attach point motion. This actuator model is experimentally verified in Chapter 4 (see Section 4.1.5). Therefore, the differential equation which describes the motion of the attach point can be written as follows:

$$\tau \dot{x} + x = x_d, \tag{3.94}$$

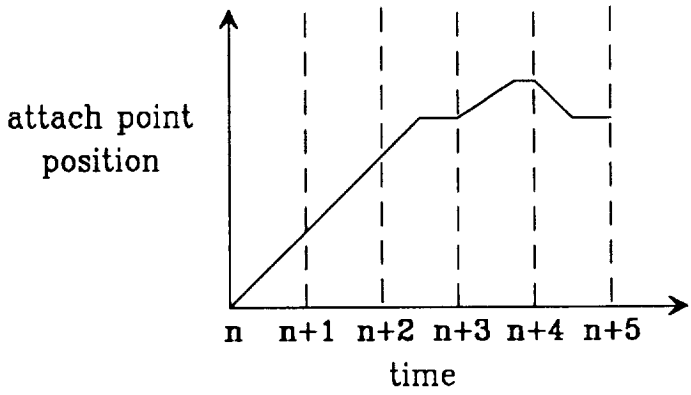

Figure 3.7: Attach Point Time History

where τ is the time constant of the lag model, x is the previously discussed attach point position with respect to the assumed mass center, and x_d is the desired attach point position as calculated by the control law.

As was the case with the large angle slew control law, in order to reject unmodeled disturbances, it will become advantageous to include integral control in the control algorithm. To that end, the state vector can be augmented with the integral of the angular orientation of the sub-satellite. A differential equation describing this integral state takes the following form:

$$\dot{e} = q, \tag{3.95}$$

where e is the error integral in the measurement of the angular orientation of the sub-satellite, q.

Equations 3.84, 3.94, and 3.95 can be combined to form four first-order, linear, coupled, differential equations of the form:

$$\begin{aligned} \dot{\mathbf{x}} &= \mathbf{F}\mathbf{x} + \mathbf{G}u, \\ y &= \mathbf{H}\mathbf{x}, \end{aligned} \tag{3.96}$$

where $\mathbf{x} = [q\ \dot{q}\ e\ x]^T$,

$$\mathbf{F} = \begin{bmatrix} 0 & 1 & 0 & 0 \\ 0 & 0 & 0 & \frac{F_0}{I} \\ 1 & 0 & 0 & 0 \\ 0 & 0 & 0 & -\frac{1}{\tau} \end{bmatrix},$$

$\mathbf{G} = [0\ 0\ 0\ \frac{1}{\tau}]^T$, $u = x_d$, and $\mathbf{H} = [1\ 0\ 0\ 0]$. The values of the system parameters for the laboratory simulator have been previously discussed (see Section 2.3). Based on the previous results, the value of F_0/I can be shown to equal $\frac{1}{15}$ $\mathrm{m}^{-1}\mathrm{sec}^{-2}$. The control law was derived using a Linear Quadratic Gaussian (LQG) formulation, which yields a full-state feedback control calculation. The real-time control law calculation takes the following form:

$$u_n = -K\mathbf{x}_n, \tag{3.97}$$

where u_n is the calculated control input at sample time n, $\mathbf{x}_n$ is the value of the above state vector at sample time n, and K is a 1x4 vector of constant control gains. In order to perform the optimal control calculation, a standard quadratic performance index must be specified. The index takes the following form:

$$J = \int_0^\infty [\mathbf{x}^T A\mathbf{x} + Bu^2]\, dt, \tag{3.98}$$

where A and B are standard weighting matrices for the system state and control input, respectively. The feedback gains were calculated by converting the analog system model and performance index to a digital system using MATRIXx. Then, the standard routine for calculating digital feedback gains was invoked to perform the gain calculation. After a few iterations (see Chapter 4), it was found that $\tau = .2$ sec, $B = 1$ m^{-2}, and

$$A = \begin{bmatrix} 100 & 0 & 0 & 0 \\ 0 & 1 & 0 & 0 \\ 0 & 0 & 5 & 0 \\ 0 & 0 & 0 & 1 \end{bmatrix}$$

(where the units of the diagonal elements of A are rad^{-2}, $(\mathrm{rad/sec})^{-2}$, $(\mathrm{rad{\cdot}sec})^{-2}$, and m^{-2}, respectively) produced the best closed-loop performance (as judged by the smallest experimentally achieved RMS value of the measured angular orientation and from necessary bandwidth considerations) for the given system model and sensor noise characteristics. The above gain calculation yields the following feedback gain vector:

$$K = [9.0820\ 20.4182\ 1.2521\ 0.3003], \tag{3.99}$$

with the dimensions of the elements equal to m/rad, m/rad/sec, m/rad·sec, and m/m, respectively. This value of the gain corresponds to closed-loop root locations which are located at $z = 0.76 \pm 0.2j$, 0.89, -0.02.

3.2.3 State Estimator

In order to implement the digital control law shown in Equation 3.97, accurate knowledge of the values of all of the state variables must be available. Instead of separately measuring each of the states with a sensor, a single measurement, in addition to an accurate system model, can yield the value of the state vector at each sample time (hence the phrase state estimation).

Three of the states, however, can be determined without estimation. The error, e, is calculated using the simple digital equivalent of Equation 3.95 and is given by:

$$e_n = e_{n-1} + Ty_n, \tag{3.100}$$

where e_n is the error and y_n is the angle measurement, respectively, at sample number n, and T is the sample period. The position and velocity of the attach point at each sample period are also available without estimation. The stepper motor is a digital device which receives shaft position commands limited to the maximum rotation it can achieve during a single time period. Therefore, at the beginning of the next sample period, the velocity is zero, and the position is equal to the commanded position at the previous sample time. The remaining states (q_n and $\dot{q}_n$) of the state vector are reconstructed with the measurement, y_n, of the angular orientation and the model of the system rotational dynamics.

In order to accurately estimate the angular position and velocity of the vehicle, it was found to be necessary to estimate the vehicle center of mass as well. A priori knowledge of the location of the vehicle mass center is necessarily limited by our ability to accurately measure this mass property. Figure 3.8 shows the effect of imprecise knowledge of the location of the center of mass. If the control algorithm assumes the mass center to be located at a point which does not coincide with the actual mass center, the algorithm will calculate a desired position of the tether attach point (and will locate the attach point) with respect to the incorrect center of mass. After the

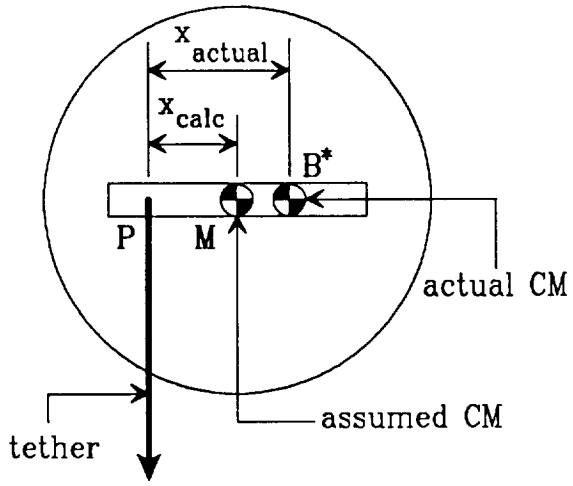

Figure 3.8: The Effect of Mass Center Knowledge

tether is moved to that point, the actual torque applied to the vehicle will be different from the calculated (desired) value. The magnitude of this difference is equal to the tether tension force multiplied by the difference between the actual and assumed mass center locations. Thus, it is clear that the assumption shown in Equation 3.80 cannot be considered valid. As a result, for the design of the state estimator, the equation describing the rotational dynamics of the vehicle should read:

$$\ddot{q} = \frac{F_0}{I}(x + d), \tag{3.101}$$

where d is the difference between the actual center of mass and the assumed mass center. Therefore, three states (i.e., angular position, angular rate, and mass center location) must be estimated based upon the single angular position measurement.

A convenient methodology to implement the state estimator is known as the Kalman Filter (see Franklin and Powell [50], Bryson and Ho [51], and Powell [52]). The discrete system model used to perform the Kalman Filter design can be formed by writing the Zero-Order-Hold model of the vehicle. The model takes the following form:

$$\mathbf{x}(n+1) = \Phi\mathbf{x}(n) + w_d(n), \tag{3.102}$$

$$y(n) = \mathcal{H}\mathbf{x}(n) + \nu_d(n), \tag{3.103}$$

where $\mathbf{x}(n) = [q(n)\ \dot{q}(n)\ d(n)]^T$ (is that part of the state to be estimated at sample

number n), $\mathbf{\Phi}$ is the state transition matrix, $y(n)$ is the measurement at sample number n, $\mathcal{H} = [1\ 0\ 0]$, and $w_d(n)$ and $\nu_d(n)$ are purely random sequences with covariance matrices Q_d and R_d, respectively. The values of $w_d(n)$ correspond to process noise which effects the dynamic behavior of the system and the values of $\nu_d(n)$ correspond to measurement noise. Equation 3.102 is derived from the following continuous model:

$$\dot{\mathbf{x}} = \mathbf{F_e x} + \mathbf{G_d} w, \tag{3.104}$$

where $\mathbf{x}$ is that part of the state vector to be estimated (i.e., $[q\ \dot{q}\ d]^T$),

$$\mathbf{F_e} = \begin{bmatrix} 0 & 1 & 0 \\ 0 & 0 & -\frac{F_0}{I} \\ 0 & 0 & 0 \end{bmatrix},$$

and $\mathbf{G_d}$ is the 3x1 disturbance input influence vector. The disturbance input, w, is modeled as a zero-mean, white noise process with spectral density Q. It can be shown that:

$$\mathbf{\Phi} = e^{\mathbf{F_e} T} \tag{3.105}$$

and

$$Q_d = \int_0^T \mathbf{\Phi} \cdot \mathbf{G_d} \cdot Q \cdot \mathbf{G_d}^T \cdot \mathbf{\Phi}^T \, dt. \tag{3.106}$$

The result of the Kalman Filter calculation is a 3x1 vector of gains, L, which form a *software* feedback system. The equations which are implemented are time update and measurement update difference equations. The time update equations are:

$$\bar{\mathbf{x}}(n+1) = \mathbf{\Phi}\hat{\mathbf{x}}(n) + \mathbf{\Gamma u_t}(n) \tag{3.107}$$

and the measurement update equations are:

$$\hat{\mathbf{x}}(n) = \bar{\mathbf{x}}(n) + L[y(n) - \mathcal{H}\bar{\mathbf{x}}(n)], \tag{3.108}$$

where $\bar{\mathbf{x}}(n)$ and $\hat{\mathbf{x}}(n)$ are the values of the states before the measurement and after the measurement, respectively, $\mathbf{u_t}(n) = [x(n-1)\ x(n)]^T$, and $\mathbf{\Gamma}$ is the control influence vector. For the current system, it can be shown that (using the values of physical

parameters discussed above):

$$\Phi = \begin{bmatrix} 1 & .5 & -.0083 \\ 0 & 1 & -.0333 \\ 0 & 0 & 1 \end{bmatrix},$$

and

$$\Gamma = \begin{bmatrix} .0042 & .0041 & 0 \\ .0122 & .0211 & 0 \end{bmatrix}^T.$$

In order to obtain some insight into the behavior of the estimator in the presence of varying process and measurement noise magnitudes, a reciprocal root locus was drawn numerically. This was accomplished by setting the value of Q to be unity, varying the value of R_d, and performing the gain calculation and determining the system pole locations for each value of R_d. After a few iterations, it was found that the best estimator behavior could be realized by making the disturbance influence vector take the following value:

$$\mathbf{G_d} = [0 \ 1 \ 4]^T. \tag{3.109}$$

The stable part of the previously discussed reciprocal root locus is shown in Figure 3.9. This figure shows that the three estimator roots start at $z = 1$, and approach the approximate values of $z = 0, \ -0.27, \ 0.88$. The pole locations which afforded the best combined controller-estimator performance correspond to a value of R_d/Q of .5 which yields estimator poles at $z = 0.88, \ 0.66 \pm 0.25j$, and the following estimator gain matrix:

$$L = [.5632 \ .4566 \ -1.3218]^T. \tag{3.110}$$

Combined Estimator and Control Laws

In order to obtain a better understanding of the action of the above control algorithm, the estimator and control law can be combined to form a discrete transfer function from the system output (i.e., the angular orientation of the air-bearing vehicle) and the control input to the system (i.e., the position of the tether attach point) [50]. With

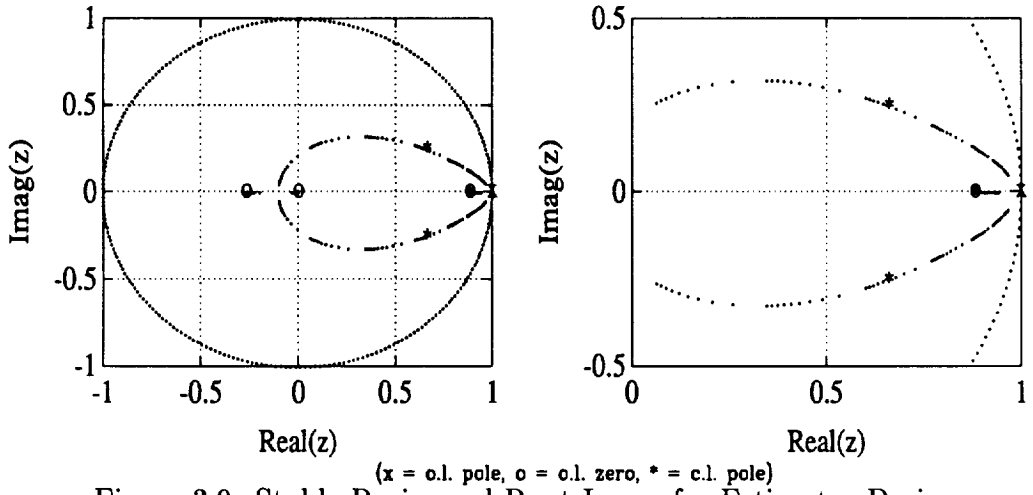

Figure 3.9: Stable Reciprocal Root Locus for Estimator Design

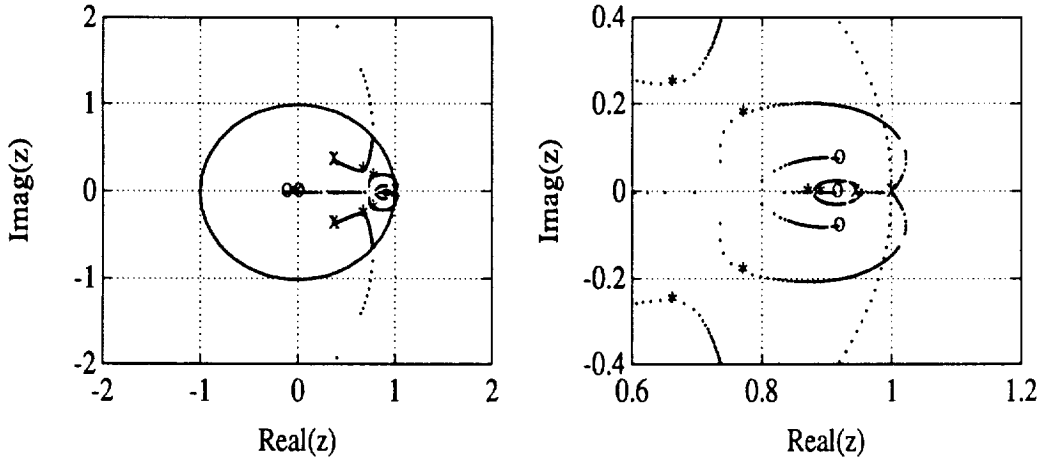

Figure 3.10: Fine Pointing Root Locus

the transfer function relating the control input to the system output, a traditional root locus of the closed-loop poles and an open-loop Bode plot can be drawn, allowing a classical interpretation of the results of the LQG control law and Kalman Filter.

The root locus of the closed-loop poles of the system is shown in Figure 3.10. This locus shows that the closed-loop poles begin at the open-loop poles of the system, $z = 1,\ 1,\ 1,\ 0.94,\ 0.36 \pm 0.36j$, and approach the open-loop zeros, $z = 0,\ -0.13,\ 0.91,\ 0.92 \pm 0.07j$. The closed-loop poles (shown as asterisks in the figure) are a combination of the estimator and control law poles, i.e., $z = 0.88,\ 0.66 \pm 0.25j$ from the estimator, and $z = -0.02,\ 0.89,\ 0.76 \pm 0.2j$ from the control law.

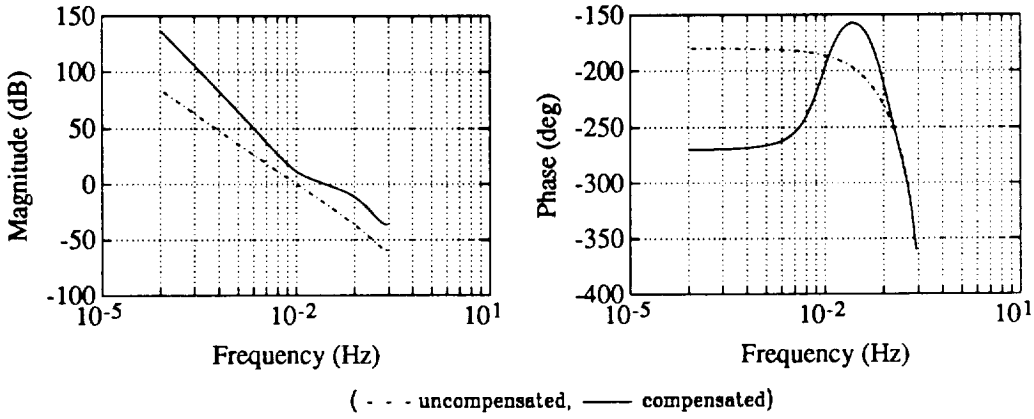

Figure 3.11: Fine Pointing Open-Loop Bode Plot

The open-loop Bode plots for the compensated and uncompensated systems are shown in Figure 3.11 (the uncompensated system is the dashed line). The magnitude plots show that the compensated system has a -60 dB per decade low frequency slope as opposed to the -40 dB per decade low frequency slope of the uncompensated system (which results from the integral control) and that the overall system DC gain is higher with the compensation. At crossover, the compensated system has a slope of approximately -20 dB per decade and the crossover frequency is approximately 0.0275 Hz. The phase plots show that the compensated system has a phase margin of approximately 25 deg. The compensator adds significant phase lead to the uncompensated system so that better system performance is achieved. The closed-loop bandwidth is approximately 0.03 Hz. The control system design is based on a sample rate of 5 Hz, which is greater than 50 times the closed-loop bandwidth. Based on the Bode plots, the compensated system can be expected to reject disturbances better and respond faster than the uncompensated system, which is the ultimate goal of any control scheme.

Chapter 4

Experimental Results

The previously described tethered satellite laboratory simulator has been used to perform an extensive study of the attitude control system which generates control torques by varying the tether attach point with respect to the satellite mass center. The purpose of the study was to test the theoretical results of the previous chapter and to determine the effect that hardware characteristics will have on the performance of the system. This includes determining the effects of estimation, stepper motor modeling, and linearity assumptions (as related to longitudinal and lateral tether dynamics). All of the experiments have been performed such that finite initial conditions were reduced to zero. Therefore, the digital control algorithm is started after the initial angle is adjusted to be a small, finite value, and the initial angular rate is made close to zero. The algorithm then attempts to regulate the vehicle attitude such that both the orientation and velocity are zero. Data are stored in the on-board computer during system operation and are transferred to the desk top host computer for data reduction. The rest of this chapter is divided into two sections: the first deals with experiments performed in a disturbance free environment while the second describes experiments performed with the inclusion of an external disturbance torque and the simulation of the effects of longitudinal and lateral tether dynamics. The first section, then, determines the best performance achievable given the current sensors and actuators and the second section determines the effects of realistic environmental disturbances which can be expected in the orbital configuration.

4.1 Disturbance-Free Experiments

Testing the simulator in a disturbance-free environment provides useful insight to the ultimate behavior of the closed-loop attitude control system. Understanding the necessary conditions in order to achieve the very best performance and then determining the degree to which each of the conditions affect the performance is useful for mission planners and system designers. The disturbance-free experiments were performed in a laboratory environment which minimized unmodeled forces external to the laboratory simulator. That is, the experiments were performed in a very quiet room, with the ventilation system turned off (in order to minimize room air currents). In addition, the tether dynamics simulator was deactivated so that only the natural mass-spring and pendular motions of the tether were present as the mechanism to generate tension variations within the tether (which tend to be small and damp out rapidly in the quiet environment). The disturbance free experiments were performed to investigate the large angle slew and fine pointing behavior, to determine the effects of varying estimator gains, to determine the extent to which the mass center estimator is necessary, and to determine the effect of varying the physical parameter assumed for the stepper motor model. The following sections treat the results of each of these experiments separately.

4.1.1 Large Angle Slew

Large angle slew capability is very important for a satellite which is to serve as an astrophysical pointing platform. Changing orientation from one target to another relatively quickly is necessary to make as much of the orbit as possible useful for mission purposes. In order to study the large angle slew capability of the tethered satellite and control system described previously, experiments were performed where the initial vehicle angular displacement was made relatively large (approximately 20-25 deg) before the control algorithm was initiated. The control algorithm was discussed in Section 3.2.1 and consists of a lead-lag compensator and integral control. The lead-lag compensator adds the necessary phase lead in order to stabilize the open-loop system while attenuating sensor noise at higher frequencies. The integral

control term was added to reject the effect of constant disturbances (i.e., steady gas leaks, steady room air currents, etc.) by increasing the gain at low frequencies. The sensor for the large angle slew maneuver is the phototransistor angle measurement device (or coarse sensor) discussed in Section 2.1.5.

The results of a typical large angle slew maneuver are shown in Figure 4.1. The figure shows the closed-loop orientation of the laboratory simulator (4.1(a) and 4.1(b)), the attach point time history which results from a typical maneuver (4.1(c)), and the power spectral density of the orientation measurement (4.1(d)). Figures 4.1(a) and (b) show that the initial angular displacement (approximately 19 deg) was reduced to a narrow band of values (with an RMS value of 0.1 deg) about the 0 deg measure. The peak time is 13 seconds and the overshoot is approximately 18 percent. This corresponds to a closed-loop system natural frequency of approximately 0.04 Hz. These results compare well with the results of the control system analysis presented in Section 3.2.1. Based on that discussion, for a second order system, the closed-loop bandwidth would be expected to be 0.036 Hz and the open-loop phase margin would correspond to approximately 30 percent overshoot. The attach point time history in Figure 4.1(c) shows that after an initial displacement to provide a control moment to initiate motion and a displacement in the opposite direction to stop the rotation, the attach point begins to randomly oscillate about the 0 cm displacement measure and the average value of the attach point position is approximately 0 cm. The random oscillations are a result of the control system reacting to the relatively large amount of noise present in the measurement. The graph of the power spectral density of the vehicle orientation in Figure 4.1(d) shows a relatively flat function for low frequencies (below the bandwidth) and significant attenuation for frequencies above the bandwidth.

The physical system responds with transient characteristics which are slightly better than those expected from the theoretical analysis. This situation likely arises because the physical system is not a second order system, but rather a fourth order system which possesses a more complicated transient response, and air-bearing support forces were ignored in the analysis (which would tend to increase the expected value of damping). Also, simulations performed with MATRIXx (see Figures 4.1(a)

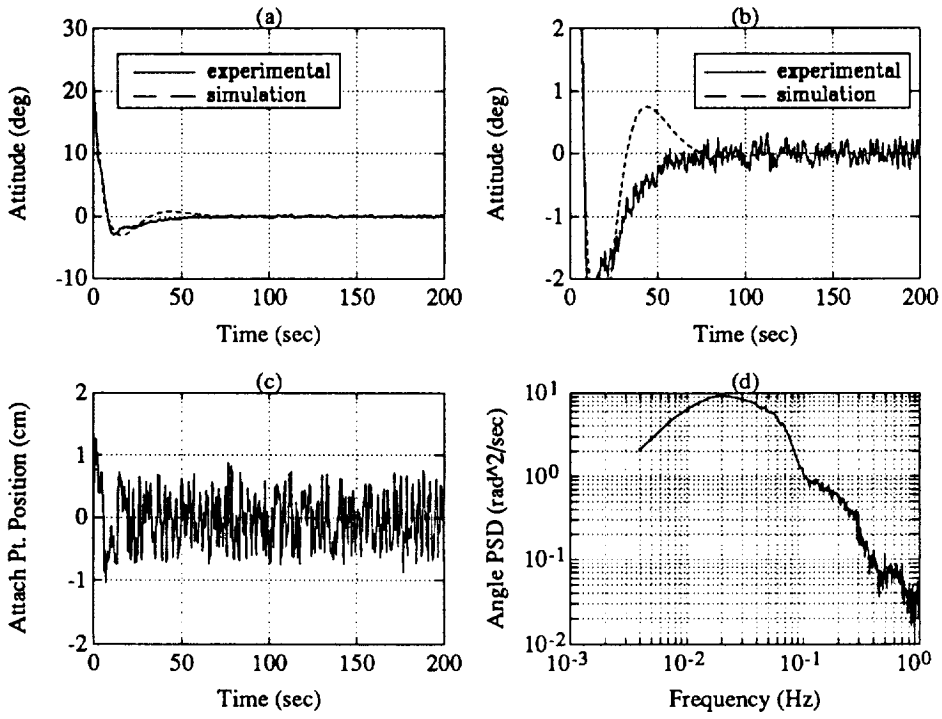

Figure 4.1: Typical Large Angle Slew Results

and (b)) show that for sensor noise modeled as a white process with a normal distribution and an RMS value equal to the actual sensor, the behavior is virtually identical as that obtained for the physical system (i.e., approximately equal peak times, overshoot percentages, and steady state RMS values). In addition, since the linear model is the result of a series of approximations, the model is not an *exact* representation of the system dynamics. The approximations can certainly be responsible for any of the small discrepancies between the results of the theoretical analysis and the physical experiment.

4.1.2 Fine Pointing

In order for a satellite to serve as a useful astrophysical pointing platform, it must provide a very stable base from which observations can be made. Lemke [42] discusses the requirements for a modern space-based telescope and concludes that an observational platform for such a telescope must provide stability on the order of 1 arcsec in order to fulfill the mission requirements. A series of experiments were performed to test the ability of the control algorithm, as implemented on the laboratory simulator, to provide a long term, high accuracy pointing platform as a base for astrophysical observations. The goal of these initial tests was to determine the best possible behavior in the most disturbance free environment possible. These results will serve as the basis from which observed behavior in the presence of realistic disturbance forces can be judged. The control algorithm which was implemented for the fine pointing experiments was described in Section 3.2.2 and the autocollimator described in Section 2.1.5 was used to make the real-time angle measurements. The control gains used in the algorithm are given by Equation 3.99. The estimator gains were based on a noise covariance ratio (R_d/Q) of 0.5 and resulted in the values given in Equation 3.110.

Results of a typical fine pointing attitude control experiment are shown in Figure 4.2. This figure shows the time histories of the estimate of the vehicle orientation, $\bar{q}(n)$, the attach point position (with respect to the assumed mass center), the error in the time update estimate of the angle, $m(n) = q(n) - \bar{q}(n)$, and the power spectral

density of the estimated attitude. The time history of the estimated vehicle orientation (Figure 4.2(a)) shows that the initial orientation (approximately 80 arcsec) is reduced to a narrow band of values about the 0 arcsec measure in 100 seconds. The peak time is 25 seconds and the overshoot is approximately 5 percent. This corresponds to a closed-loop bandwidth of approximately 0.03 Hz. The RMS value of the measured attitude from 200-500 seconds is 0.60 arcsec and the average value over that time period is 6.6×10^{-3} arcsec. The attach point time history (Figure 4.2(b)) shows that after an initial large step to start the angular motion, the position returns to a narrow band of values about the -0.6 mm measure. The random motion of the position is a result of the control algorithm reacting to sensor noise and the non-zero steady-state average value is the result of a difference between the assumed and actual mass center locations (as is calculated by the mass center estimator). The error in the time update estimate of the angle (Figure 4.2(c)) shows that after the first 100 seconds, the estimate converged to the measured value (within sensor limitations). The RMS value of the error for the time between 200-500 seconds can be calculated to be 0.75 arcsec and the average value during that time period is 7.5×10^{-4} arcsec. The power spectral density of the angle estimate (Figure 4.2(d)) shows a flat function for frequencies below the bandwidth and attenuation for frequencies above the bandwidth. Also, the mass-spring mode of the air-bearing vehicle and tether/spring system is clearly evident through the relatively large spike at 0.3 Hz, which is the previously calculated laboratory mass-spring mode natural frequency (see Table 2.1).

These observed results compare quite well with the theoretical results obtained in Section 3.2.2. In addition, a FORTRAN simulation of the dynamic behavior (based on the subroutine shown in Appendix A.2) of the closed-loop system yielded results which were virtually identical to the observed behavior of the laboratory simulator. The peak times, the overshoot, and the steady-state RMS values were all within 10% of the measured values for the laboratory simulator.

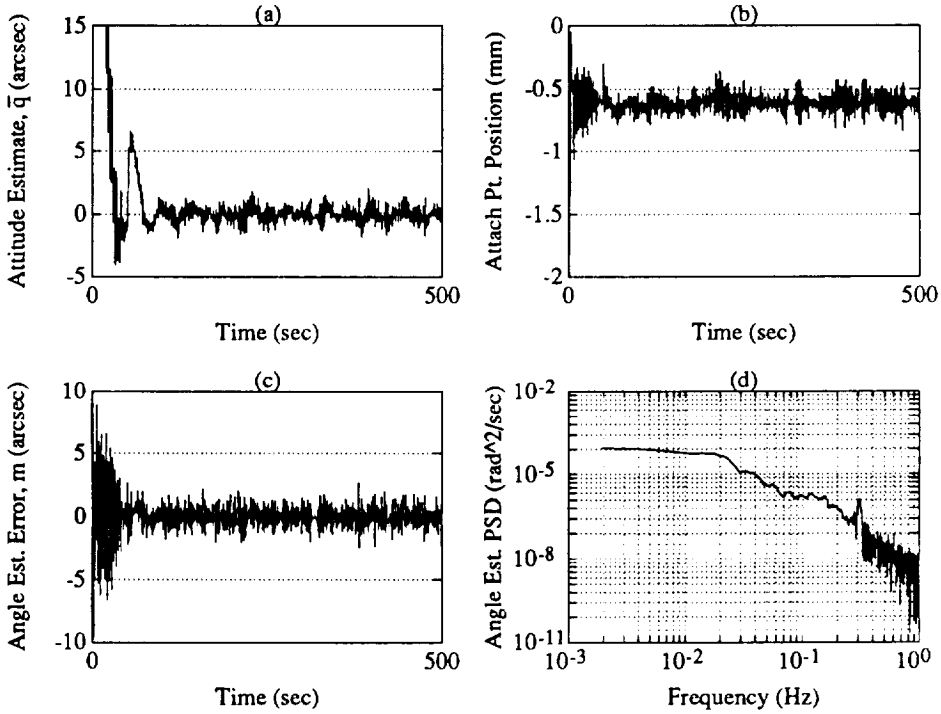

Figure 4.2: Typical Fine Pointing Results

4.1.3 Effect of Estimator Gains

The discussion of the derivation of the state estimator (see Section 3.2.2) showed how the process and sensor noise models played a key role in determining the numerical values of the estimator feedback gains. In fact, Figure 3.9 presents a root locus of the estimator roots as a function of the ratio of the sensor and process noise covariances. To determine the effect that different assumed values for the ratios of the sensor to process noise covariances would have on the closed-loop system performance, a series of tests were performed where the noise covariance ratio (i.e., R_d/Q) was varied for purposes of computing the estimator gains. Increasing this ratio moves the root locations along the root locus shown in Figure 3.9 from the open-loop poles (in this case three roots at $z = 1$) towards the open-loop zeros (calculated to be $z = 0, -.27, .88$). Increasing the covariance ratio causes the estimator to converge to the actual state value more rapidly, but the faster convergence can amplify the sensor noise unnecessarily. The goal, then, is to choose estimator root locations which allow timely state convergence yet maintain reasonable sensor noise filtering. This balancing is most easily performed with an extremely accurate system model and was the motivation behind the mass center estimator discussed previously.

Results of the different tests performed with the experimental system and varying values of estimator gains are summarized in Table 4.1. This table shows the ratio of sensor noise covariance to process noise covariance (R_d/Q) used in the estimator gain calculation, the RMS value of the steady state estimate of angular orientation ($\bar{q}(n)$), and the RMS value of the error in the estimate of angular orientation before the measurement ($m(n) = q(n) - \bar{q}(n)$). The estimate of the angular orientation gives a quantitative measure of the performance of the closed-loop system (i.e., control law and estimator) and the error in the estimate of the angular orientation before the measurement provides a quantitative measure of the performance of the estimator implementation. The results shown in the table support the thesis that varying sensor and process noise models will effect the behavior of the estimator and closed-loop system. Small values of the covariance ratio result in relatively poor estimator and closed-loop system performance. This results from the slow (sluggish) response time of the estimator and too great a reliance on a model which may not be 100% accurate.

R_d/Q	$\bar{q}(n)$ (arcsec)	$m(n)$ (arcsec)
0.01	1.11	1.07
0.05	0.86	0.75
0.10	0.71	0.74
0.50	0.60	0.75
1.00	0.70	0.94
5.00	0.78	1.58
10.0	0.84	1.98

Table 4.1: Effect of Estimator Gains on RMS Performance (nominal $R_d/Q = 0.5$)

Large values of the covariance ratio also result in relatively degraded performance. This results because of the small amount of sensor noise filtering provided by an estimator with a relatively fast (quick) response time. The mid-range values of those shown result in fairly equal estimator performance, but slightly different closed-loop system behavior. The performance of the estimators are all basically equivalent because they filter sensor noise roughly equally. The closed-loop system behavior is different because of the location of the estimator roots with respect to the controller root locations. For the 0.01, 0.05, and 0.10 values of R_d/Q, the estimator root locations correspond to an estimator which is slower than the controller roots, whereas when $R_d/Q \geq 0.50$, the estimator roots correspond to an estimator which is faster than the controller. An estimator which is slower than the controller can cause slightly degraded closed-loop performance in the response to step commands and unmodeled disturbances because the control calculation will be based on a state estimate which does not respond as quickly as the controller responds.

4.1.4 Effect of Mass Center Estimation

The derivation of the state estimator in Section 3.2.2 includes a qualitative argument justifying the need for estimation of the center of mass of the sub-satellite in order to perform long term, high accuracy pointing. In order to determine, quantitatively, the effect of the mass center estimator, a series of tests were performed without the implementation of the mass center estimator. The center of mass of the vehicle

was accurately located (to within 0.05 mm) with respect to the center of the vehicle base plate using the results of the mass center estimator implemented in Section 4.1.2. Then, for purposes of this study, the mass center location was assumed to be different from the known location. Two tests were performed, one with an intentional mass center misalignment of approximately 0.10 mm and the other with the misalignment intentionally set to 0.40 mm. The control gains were made the same as those discussed in Section 3.2.2. The estimator, without mass center estimation, can be derived by changing the value of the disturbance influence vector given in Equation 3.109 to equal the following value instead:

$$\mathbf{G_d} = [0\ 1\ 0]^T. \tag{4.1}$$

The effect of this change on the estimator is that since there is no model of process noise disturbing the location of the mass center, the Kalman Filter will assume that the initial location is, in fact, the actual mass center location (effectively an oblivious filter) and the estimator gain associated with this state will be zero. The reciprocal root locus for the current system can be drawn in the same manner as that shown in Figure 3.9. The result will be almost identical to the root locus shown in that figure. The one difference will be that the root which travels left along the real axis in the figure will remain located at the $z = 1$ point for all covariance ratios. The remaining two roots traverse the same locus as shown previously, although locations along the locus correspond to different noise covariance ratios. Experiments were performed with estimator gains calculated from various covariance ratios in an effort to judge the effect of estimator speed of response in addition to the mass center estimation.

Results of these tests are summarized in Figures 4.3 and 4.4. Figure 4.3(a) shows the closed-loop attitude angle estimate before the measurement ($\bar{q}(n)$) and Figure 4.3(b) shows the error in the estimate before the measurement ($m(n) = (q(n) - \bar{q}(n))$) as a function of time for the experiment with an intentional mass center misalignment (d) equal to 0.40 mm and a value of R_d/Q equal to 5.0. As expected, the mass center misalignment caused the control algorithm to calculate attach point locations which did not provide the necessary control torques to zero the attitude of the vehicle. For the time between 200 and 500 seconds, the average

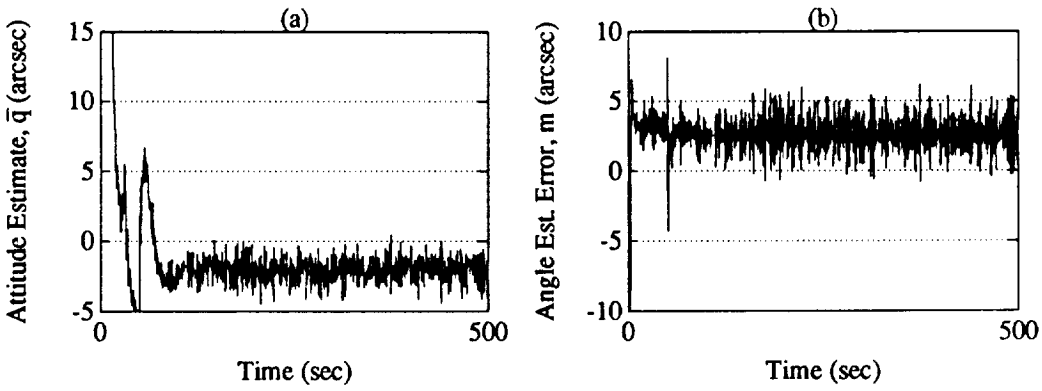

Figure 4.3: Results Without Mass Center Estimation (with CM error of 0.4 mm)

value of the attitude estimate is -2.05 arcsec, the RMS value of the attitude estimate is 2.21 arcsec, and the RMS value of the error in the angle estimate is 2.86 arcsec. This is in sharp contrast to the comparable values obtained for the case with the mass center estimator. The degradation in performance results from the effect discussed in Section 3.2.2 and summarized in Figure 3.8. That is, the actual control torque applied to the vehicle differs from the desired value because of the mass center misalignment.

Figures 4.4(a) and (b) show the absolute value of the angle estimate before the measurement, $\bar{q}(n)$, as a function of mass center misalignment for various values of the noise covariance ratio, R_d/Q, and the RMS value of the attitude estimate before the measurement, $\bar{q}(n)$, as a function of noise covariance ratio for two values of mass center error, d. The values shown in the figures make physical sense. The tests performed with a smaller mass center misalignment would be expected to show better behavior than the case where the center of mass misalignment was larger. The smaller the misalignment, the smaller the difference between the actual and desired control torques, the smaller the error in estimating the state. This should yield smaller mean square and average values of the attitude error. In addition, higher estimator gains (which correspond to a higher noise covariance ratio) force the Kalman Filter to rely less on the system model and more on the given measurement. A deemphasis of the model will produce smaller estimator errors, translating into better performance. It should be noted, however, that blindly increasing the gains of the

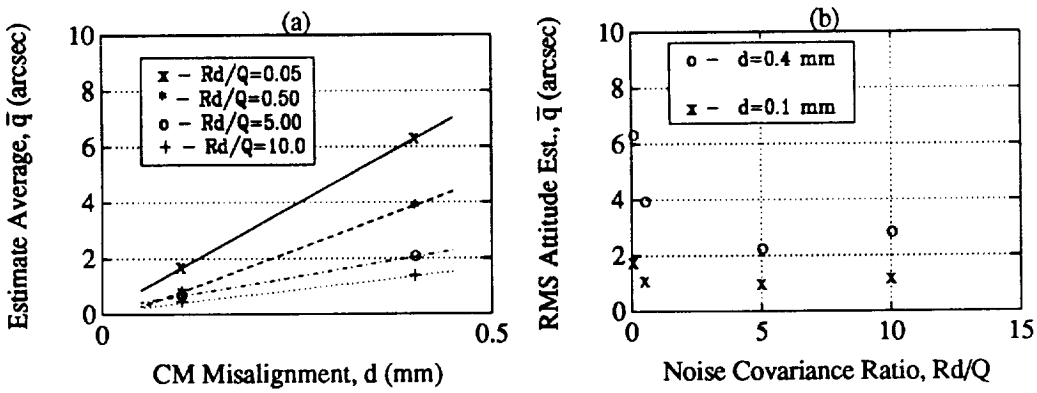

Figure 4.4: Summary of Results Without CM Estimation

estimator can have detrimental effects, as can be seen in Figure 4.4(b). Increasing the covariance ratio benefits the operation of the control system until the ratio approaches a value of approximately 5. At this point, the estimator is amplifying the noise in the measurement unnecessarily. The purpose of low estimator gains is to filter the noise of the measurement by balancing the knowledge gained from each measurement with a priori knowledge of the system (i.e., the system model). A very accurate system model allows lower gains and, therefore, more filtering of the measurement. A good estimator will possess the lowest possible gains (the highest possible filtering) and the most accurate model available.

It should be noted, that the mass center misalignments measured in the laboratory are quite small with respect to a characteristic dimension of the vehicle (on the order of 0.01% and 0.04%, respectively). For a realistic satellite implementation, a 1% of a characteristic dimension misalignment would not be unexpected. As a result, the effect of mass center misalignment in a practical application can be on the order of 100 times greater than the effect measured in the laboratory (i.e., on the order of 100 arcsec). Clearly, mass center estimation should be an integral part of a high accuracy tethered satellite attitude control system which generates control torques by varying the attachment of the tether with respect to the mass center of the vehicle.

τ (sec)	$\bar{q}(n)_{rms}$ (arcsec)	$m(n)_{rms}$ (arcsec)
0	1.59	1.26
0.01	0.75	1.06
0.02	0.73	0.98
0.20	0.60	0.75
2.00	0.66	1.24
4.00	0.70	1.32

Table 4.2: Summary of Tests Varying Motor Time Constant

4.1.5 Effect Of Stepper Motor Model

The linear model of the stepper motor was discussed previously in Section 3.2.2. Figure 3.7 qualitatively summarizes the need for attach point motion modeling. The linear model chosen to represent the dynamics of stepper motor motion is shown in Equation 3.94 to be a simple first order lag which is characterized by the time constant, τ. In an effort to determine the quantitative effects of varying the model of the stepper motor dynamics, a series of tests were performed with compensators designed by assuming various values of the time constant. When designing a compensator, the value of τ effects both the feedback control gains, K, and the control influence vector, Γ. The feedback gains were calculated with the same state and control weighting matrices (A and B, respectively) as the nominal case discussed in Section 3.2.2. In addition, the estimator gains were identical to those shown in Equation 3.110.

The results of these tests are shown in Table 4.2. The table shows that varying the time constant of the stepper motor does indeed affect the behavior of the closed-loop system and the performance of the state estimator. The best response is obtained when $\tau = 0.2$ seconds, which corresponds to the vehicle attitude time history shown in Figure 4.2. The worst response, as can be expected, corresponds to the case where the dynamics of the stepper motor are ignored (i.e., $\tau = 0$ seconds). All other values of τ which were tested resulted in closed-loop systems with measured angle RMS values that are less than 1 arcsec. However, the estimator performance, as judged by the RMS value of the error in the angle estimate before the measurement, was affected

to a greater extent. The increase in sensitivity of the estimator is due to the fact that varying the model varies how well the model represents the physical mechanism and since the angle estimate before the measurement was used to compare the model performance, the sensitivity is heightened. The control input, on the other hand, is calculated based on the state estimate after the measurement, which is the less model sensitive (because of the fresh state information contained in the measurement) of the time and measurement update state vectors.

Figures 4.5(a)-(d) provide a visual representation of the physical significance of modeling the nonlinear stepper motor with a linear differential equation. The figures show the actual motion of the attach point and the attach point motion modeled as a low pass filter (with $\tau = 0.2$ seconds) for cases when the desired motion during one sample period takes on the values of 1 in (a), 0.5 in (b), 0.1 in (c), and 0.02 in (d). The figures show that the model is not an exact representation of the attach point motion, and that the differences between the actual and modeled motion depends on the size of the desired motion. This tendency arises due to the strong dependency of the actual motion on the size of the input. The results and discussion emphasize the fact that care must be taken when modeling nonlinear devices with linear differential equations.

4.2 Fine Pointing With Disturbance Torques

While the disturbance-free experiments provide important insight into the design of a system employing the previously discussed attitude control concept, a complete investigation must study the effect of disturbances applied to the sub-satellite from the parent spacecraft through the tether. He [31] discusses simulation results obtained by modeling the three dimensional deployed configuration of a tethered satellite which implements an attitude control system based on a movable tether attach point. An important conclusion from these simulations is that the yaw axis control device (most likely a momentum wheel) can create an offset between the vehicle mass center and the steady-state tether attach point. This offset, in conjunction with magnitude and direction variations in the tether tension, is responsible for the largest disturbance

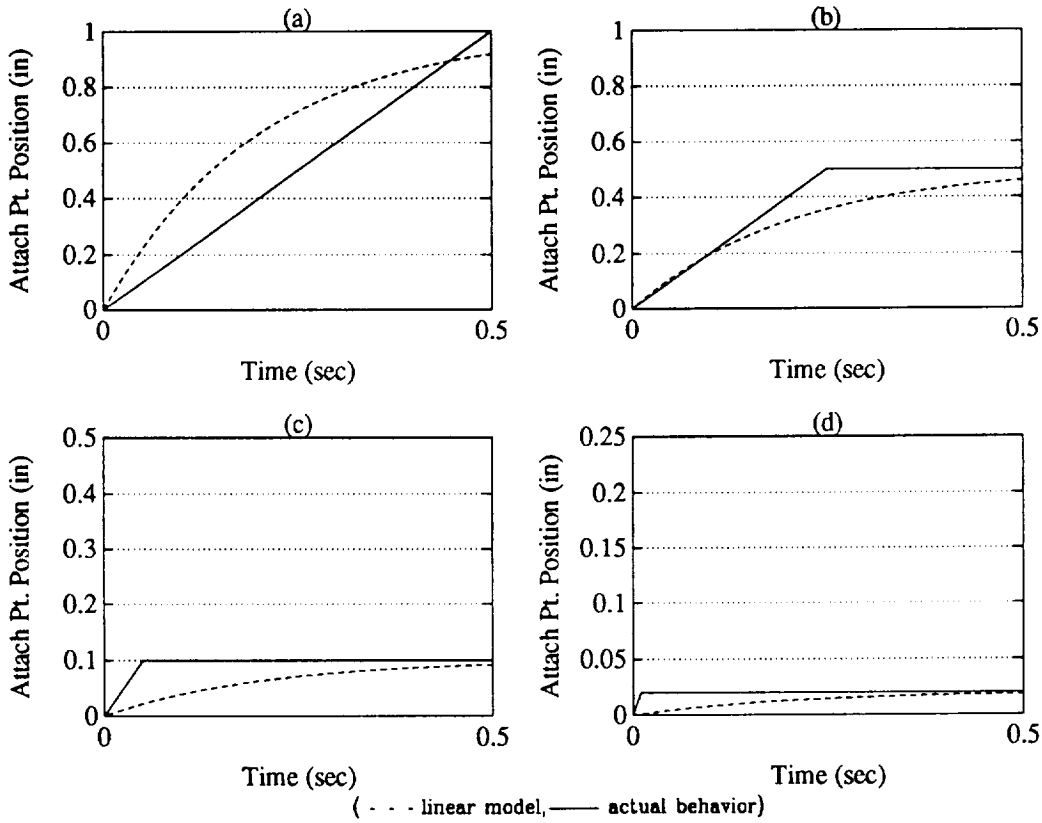

Figure 4.5: Comparison of Stepper Motion to Linear Model

torque applied to the vehicle. As secular yaw disturbances are controlled with the momentum wheel, the wheel will store a significant amount of momentum in the orbit plane. This momentum, when rotated in the orbit plane, induces a torque about the roll axis of the sub-satellite. The magnitude of the roll torque builds up as the momentum stored in the momentum wheel increases, and will only decrease if a momentum dump maneuver is instigated. He [31] also describes a method to dump the momentum when the wheel saturates or when it is deemed appropriate for system performance.

In the current laboratory work, the primary concern is to determine the effects of both the lowest order longitudinal oscillation (mass-spring mode) and the lowest order lateral oscillation (first string mode) on attitude errors of the tethered spacecraft. These tether dynamics, in essence, effect the satellite in the form of a complicated combination of tether tension variations (in both magnitude and direction). The combination of these tension variations can be calculated with the mathematical models developed by He [31]. Therefore, the method employed in the current work, will be to verify the behavior of the attitude control system in the presence of tether tension magnitude and direction variations. Then, these variations can be combined in the proper ratio (as determined by He's model) to predict behavior of the proposed orbital mission.

The following sections separately discuss the analytic description of the disturbance torque generation, the effect of a constant disturbance torque on the performance of the closed-loop system, the simulation of tether tension magnitude and direction variations and their effect on the attitude control algorithm, the effect of the combined tether dynamics on the attitude control performance, the effect of the mass center estimation on performance in the face of disturbances, and the implementation of a variable tension scaling scheme (as proposed by Lemke [42]).

4.2.1 Disturbance Torque Generation

For spacecraft with an altitude less than 400 km, the aerodynamic torque is the dominant environmental disturbance torque applied to the vehicle [49]. A simplified model of the aerodynamic surfaces of a tethered spacecraft is shown in Figure 4.6.

This figure shows a six sided rectangular solid with dimensions as shown. The $\underline{\mathbf{b}}_1$, $\underline{\mathbf{b}}_2$, and $\underline{\mathbf{b}}_3$ vectors are a right handed set of mutually orthogonal reference axes fixed in body **B**. $\underline{\mathbf{b}}_1$ points in the nominal tether direction (yaw axis), $\underline{\mathbf{b}}_2$ points in the direction of travel of the mass center of **B** (roll axis), and $\underline{\mathbf{b}}_3$ is perpendicular to the orbit plane (pitch axis). The magnitude of the aerodynamic force applied to the body in the $\underline{\mathbf{b}}_2$ direction, F_{aero}, is given by (assuming the rotation rate of the vehicle with respect to the tether is sufficiently small):

$$F_{aero} = \frac{1}{2} C_D A_2 \rho |\underline{v}^{B^*}|^2, \tag{4.2}$$

where C_D is the drag coefficient of the vehicle moving along $\underline{\mathbf{b}}_2$, A_2 is the area of the surface perpendicular to the $\underline{\mathbf{b}}_2$ axis, ρ is the atmospheric density through which the vehicle travels, and $\underline{v}^{B^*}$ is the relative velocity of the center of mass of the vehicle with respect to the on-coming air. With $C_D \approx 2$, $A_2 = 2.6$ m^2, $\rho \approx 10^{-13}$ kg-m^{-3}, and $|\underline{v}^{B^*}| \approx nR_0 \approx 6500$ m-sec^{-1} (where R_0 is the orbit radius and n is the orbit rate), $F_{aero} = 1.0 \times 10^{-5}$ N. The moment about the $\underline{\mathbf{b}}_1$ (yaw) axis, M_1, is given by:

$$M_1 = F_{aero} \delta_3, \tag{4.3}$$

where δ_3 is the point, relative to the center of mass of the vehicle, in the $\underline{\mathbf{b}}_3$ direction, through which the aerodynamic force acts. Assuming that δ_3 is 1% of the length of the vehicle side parallel to $\underline{\mathbf{b}}_3$, and substituting the value for F_{aero} shown above into Equation 4.3, it can be shown that $M_1 \approx 2.0 \times 10^{-7}$ N-m.

The magnitude of the momentum stored in the wheel parallel to the yaw axis, h_1, is given by the following differential equation,

$$\dot{h}_1 = M_1. \tag{4.4}$$

Since M_1 is assumed constant,

$$h_1 = M_1 t, \tag{4.5}$$

where t is the time measured in seconds. The torque due to the momentum wheel about the $\underline{\mathbf{b}}_2$ axis, T_2, is the product of the orbital rate and the momentum stored in the wheel, and is given by:

$$T_2 = M_1 n t. \tag{4.6}$$

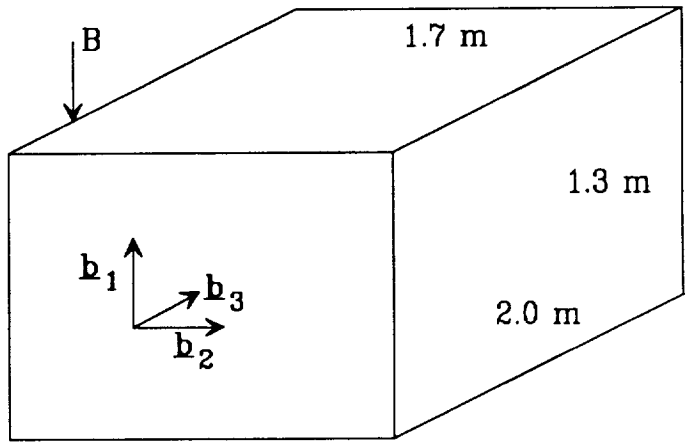

Figure 4.6: Simplified Aerodynamic Model of Sub-Satellite

Figure 4.7 is a graphical representation of Equation 4.6 with respect to time (measured in the number of orbits). This figure shows that the roll torque grows linearly from a zero value at zero time to slightly less than 3×10^{-4} N-m after 200 orbits. Figure 4.7 also provides a simple guide to the timing of momentum wheel desaturation maneuvers. For each value of roll torque, the momentum can be dumped after an easily calculated number of orbits. For example, if 5.5×10^{-5} N-m is the largest tolerable disturbance torque, a maneuver to dump the momentum stored in the wheel after every 40 orbits (approximately once every other day) will ensure that the disturbance torque never exceeds this threshold value.

4.2.2 Effect of Constant Disturbance Torques

In order to observe the behavior of the tethered satellite attitude control system based on a movable tether attach point in the presence of a constant disturbance torque, the air-bearing simulator was outfitted with a small fan. The fan is mounted approximately 0.5 m from the center of mass, so that when it is turned on, a constant torque is applied to the vehicle. The results of these tests are expected to show that the closed-loop attitude response of the vehicle will be unchanged from the

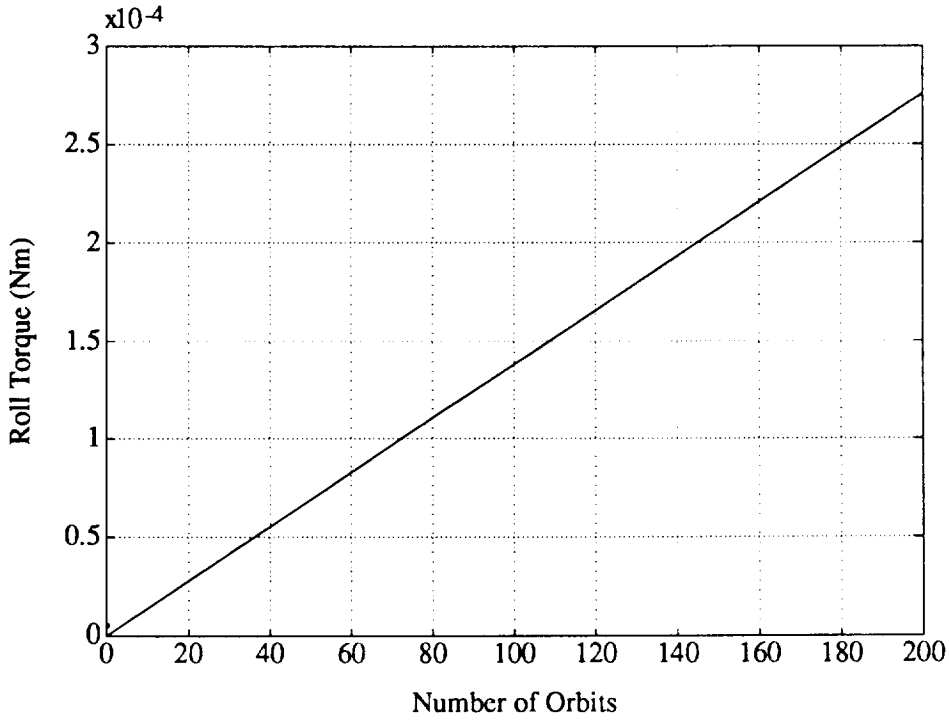

Figure 4.7: Total Roll Disturbance Torque

results obtained in the disturbance free environment. A number of experiments were performed with the fan blowing in such a manner that it applied a constant torque of magnitude 5×10^{-4} N-m to the vehicle. The initial state of the system was configured such that the angle and angular rate was made as small as possible and the fan was running (i.e., applying a force to the simulator). Figure 4.8 shows the typical results of a test performed with the fan blowing and the tether dynamics simulator deactivated. The figure shows the time histories of the estimated attitude of the vehicle ($\bar{q}$), the attach point position with respect to the assumed mass center location, the error in the estimate of the angle before the measurement (m), and the power spectral density of the estimated orientation. The figure shows that the response of this system is virtually identical to the case where no external disturbance was applied to the vehicle (see Figure 4.2). This result is completely consistent with expectations of the system behavior and will be explained below. The initial small angle error is reduced to a random fluctuation about the 0 arcsec measure in 100 seconds. The peak time is approximately 25 seconds and the overshoot is 25 percent. The RMS

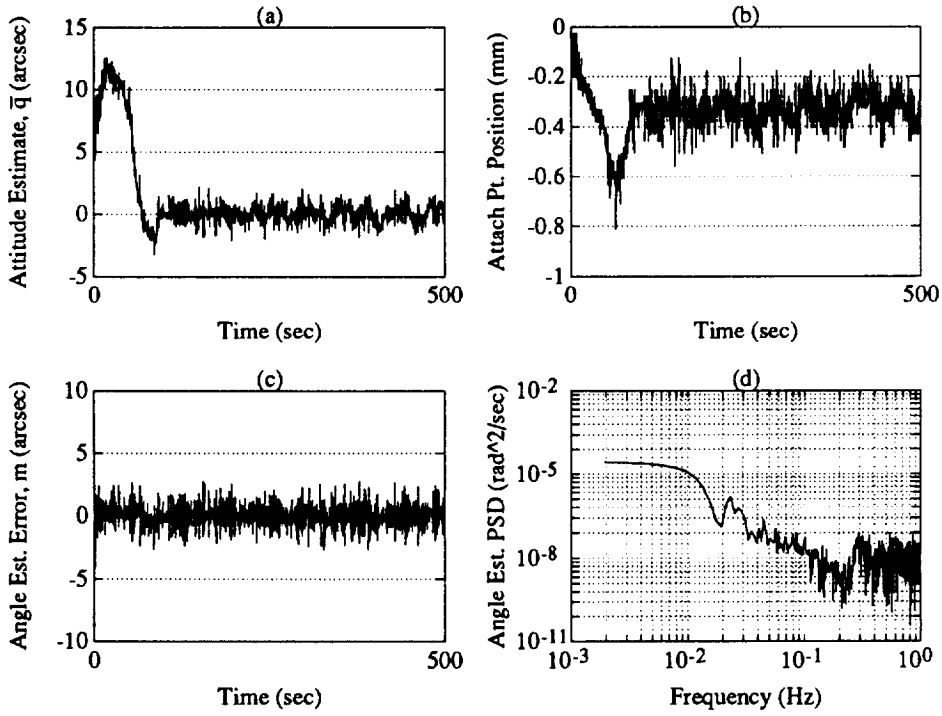

Figure 4.8: Closed-Loop Results with Constant Disturbance Torque

(1-2

value of the attitude measurement from 200-500 seconds is 0.71 arcsec and the average value over that time period is 0.017 arcsec. The time history of the error in the angle estimate before the measurement is very similar to the case with no disturbance torque. The estimate converges to the measured value in less than 75 seconds and for the period between 200-500 seconds, the RMS value is 0.88 arcsec, and the average value over that period of time is 0.0021 arcsec. The tether attach point time history is slightly different than the result obtained without an external disturbance. The steady state average value is approximately -0.35 mm (which is smaller than the disturbance-free result because of a smaller initial mass center misalignment) and the transient response shows a clear convergence to the steady-state value (which was absent in the disturbance-free case). The finite convergence time is the result of the mass center estimator calculating an 'effective' mass center location, one that is the combination of the initial mass center misalignment (as in the disturbance-free case) and the effect of the constant disturbance. Essentially, the constant disturbance torque is modeled as a mass center misalignment in the Kalman Filter equations and the estimator must converge to the correct 'effective' mass center. This can be seen by modifying the differential equation used to model the rotational dynamics of the vehicle (see Equation 3.101) to include a disturbance torque term. Therefore, the equation of motion for the rotational system will read:

$$\ddot{q} = \frac{F_0}{I}(x + d) + M_d, \tag{4.7}$$

where M_d is the disturbance torque applied to the vehicle. This disturbance torque can be represented as a force multiplied by the appropriate distance to keep the torque magnitude constant. If we choose the force to be equal to F_0, the disturbance torque can be expressed as:

$$M_d = F_0 d_d, \tag{4.8}$$

where d_d is the 'effective' offset from the mass center of the tether needed to generate the necessary disturbance torque. Combining Equations 4.7 and 4.8 directly yields the following equation:

$$\ddot{q} = \frac{F_0}{I}[x + (d + d_d)]. \tag{4.9}$$

In this form, it is clear that the disturbance torque can be modeled exactly as a mass center misalignment. As a result, the fact that the attitude response should be the same both with and without a disturbance torque follows because the mass center estimator provides integral action which behaves precisely the same, independent of whether the disturbance is a mass center error (as in Figure 4.2) or a constant disturbing force (as in Figure 4.8). The power spectral density of the angle measurement shows the characteristic flat response at low frequencies (below the bandwidth) and attenuation at frequencies above the bandwidth. In addition, the small spike at 0.03 Hz can be attributed to the convergence time of the mass center estimator. Also, the mass-spring mode of the satellite and tether/spring system is also visible through the small rise at 0.3 Hz.

4.2.3 Tether Force Magnitude Variations

As discussed previously, the introduction of natural tether dynamics into the laboratory simulation is quite important in determining the ultimate effectiveness of a tethered satellite attitude control system based on a movable tether attach point. The goal of the following sections is to determine the behavior of the attitude control system when the force applied to the simulator by the tether varies in magnitude only. In order to introduce the type of tether force magnitude variations (that would be expected in orbit) to the laboratory simulator, it is necessary to have a good model of the orbital tether and the interaction of the tether and movable attach point control system. To achieve this end, a detailed mathematical model of the orbital system was developed by He [31]. The model is based on a continuous beam description of the tether and it is used to implement a three dimensional (six degree of freedom) simulation of the complete tethered satellite system (including longitudinal, and in-plane and out-of-plane lateral tether dynamics) in MATRIXx. This mathematical model and computer simulation were used to determine the dominant frequencies of the tether tension magnitude variations which can be expected in the orbital configuration.

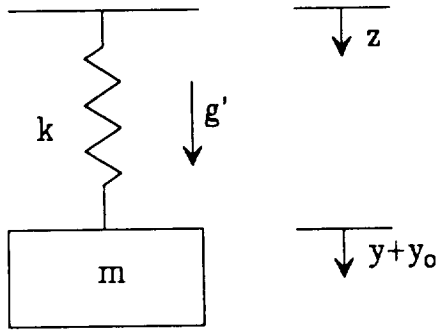

Figure 4.9: Simplified Longitudinal Tether Model for Simulations

Laboratory Simulation

With knowledge of the dominant frequencies of variations in tether tension magnitude, the tether dynamics simulator discussed in Section 2.2 can be used to implement the expected tension variations in the laboratory. The tether dynamics simulator will be configured such that the wall attach point will follow an oscillatory path in the nominal tether direction (i.e., along the local vertical). If we assume a fixed tether attach point on the sub-satellite, the configuration of the air-bearing vehicle suspended in the micro-gravity field with a tether/spring which is attached to a movable wall attach point can be modeled (ignoring the damping effects of the air-bearing and spring material) simply as the system shown in Figure 4.9, where $y_o = mg'/k$. The transfer function between motion at the wall and motion at the sub-satellite end, $H_{yz}(s)$, is simply:

$$H_{yz}(s) = \frac{\omega_m^2}{s^2 + \omega_m^2}, \tag{4.10}$$

where s is the Laplace Transform variable and $\omega_m = \sqrt{k/m}$ is the natural frequency of the mass-spring system. The transfer function between tension variations in the spring and wall motion, $H_{dFz}(s)$, is given by:

$$H_{dFz}(s) = k[H_{yz}(s) - 1] = \frac{-ks^2}{s^2 + \omega_m^2}. \tag{4.11}$$

A Bode magnitude plot of the above transfer function for the laboratory simulator is shown in Figure 4.10. This plot shows the correspondence between wall attach point

oscillations and tether tension variations. Wall attach point motions will generate tension magnitude variations in the tether/spring which are of the same frequency as the wall motion and the magnitude will be scaled, dependent on the wall motion frequency (i.e., as is shown in the Bode diagram). The natural frequency of the mass-spring mode can be seen to be 0.3 Hz. The spring constant was chosen so that the laboratory natural frequency would be approximately one order of magnitude greater than the orbital case (see Section 2.3). This was done so that when the wall attach point is used to generate tension variations, the motion of the air-bearing simulator would be well behaved. If the laboratory mass-spring frequency were made very close to the desired experimental tension magnitude variation frequency (which is determined from the orbital system model) the simulator would undergo extremely large motions for very small wall attach point motions. This is undesirable for two reasons. First, the simulator motions would be so large that the edge of the vehicle would pass the edge of the granite support table, which would introduce significant unmodeled dynamic behavior. Second, when a mass/spring system is excited at it's natural frequency, the resulting behavior is largely determined by the damping in the system (i.e., in the spring and in the air-bearing suspension system), a quantity which is very difficult to determine accurately.

Finally, the discussion in Section 2.3 called attention to the fact that the characteristic response time (bandwidth) of the orbital case is somewhat different than that for the laboratory simulator. Therefore, it will be necessary to correlate the frequencies of the disturbances expected in orbit to properly scaled values in the laboratory configuration. In order to make this correlation, it is important to realize that the spacing, in the frequency domain, between the system bandwidth and the tether tension variation frequencies are important quantities. As a result, in order to translate the orbital disturbance frequencies to laboratory frequencies, the ratio of bandwidth to disturbance frequency was made invariant. Therefore, the procedure to determine the frequency at which to oscillate the wall attach point motion is as follows:

1. Determine the dominant orbital tension magnitude variation frequency from the mathematical model and computer simulation developed by He [31].

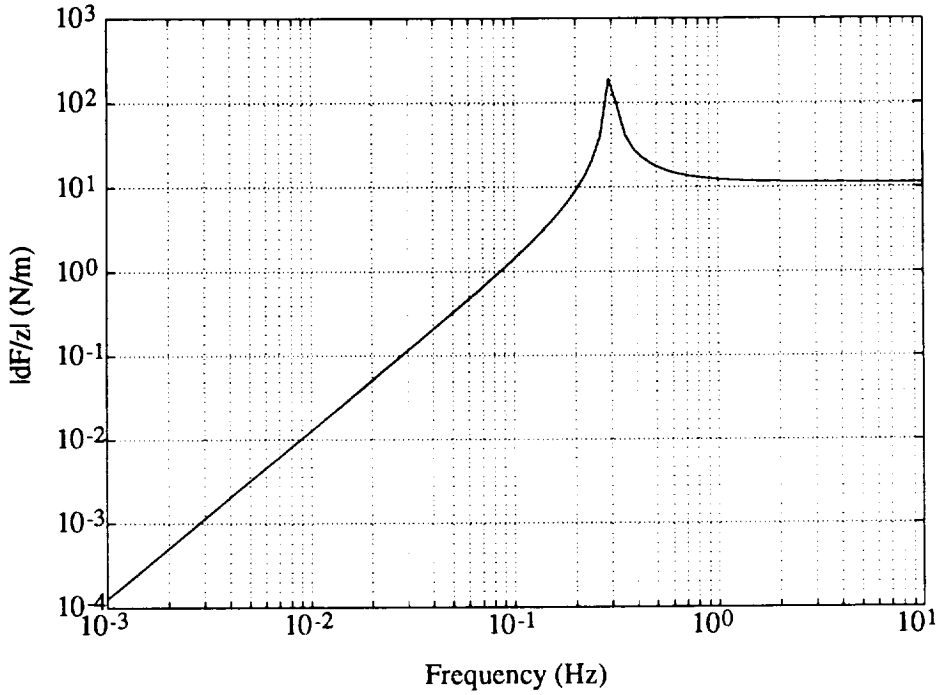

Figure 4.10: Bode Magnitude of Longitudinal Tension Variations to Wall Attach Point Motion

2. Determine the frequency at which the wall attach point mechanism should be oscillated. This is determined by scaling the frequency derived in Step 1 by the ratio of the laboratory bandwidth to the orbital bandwidth.

The result of this procedure for tension magnitude variations yields a frequency of 0.025 Hz in the orbital case, which translates to a frequency of 0.033 Hz for the necessary tension magnitude variations in the laboratory case.

Frequency Response

The effects of tension magnitude variations of the tether on the performance of the attitude control system based on a movable tether attach point can be summarized by considering the frequency response between tension magnitude variations and the ability to control the sub-satellite orientation. The differential equation which describes the rotational motion of a tethered sub-satellite was derived previously in

Equation 3.74 and reads as follows:

$$\dot{u}_3 = \frac{1}{I_3}\left[|\underline{F}_t|(x+d)(c_\mu c_3 + s_\mu s_3) - b_r u_3\right]. \tag{4.12}$$

Recalling that $\dot{q}_3 = u_3$ and making the substitutions $q \equiv q_3$ and $I \equiv I_3$ to simplify notation, Equation 4.12 can be rewritten as:

$$I\ddot{q} = |\underline{F}_t|(x+d)(c_\mu c_q + s_\mu s_q) - b_r \dot{q}. \tag{4.13}$$

To perform high accuracy orientation control while simulating tether tension variations, it can be observed that μ, q, and $\dot{q}$ will all be small. In addition, since the control system will calculate the actual mass center location, d will also be small. Finally, the magnitude of the tether tension, $|\underline{F}_t|$, can be written as in Equation 3.78 to emphasize the steady component and zero mean variation superimposed on the nominal tension value (which arises from the micro-gravity acceleration). As a result, Equation 4.13 can be simplified to read:

$$I\ddot{q} = (F_0 + dF)x, \tag{4.14}$$

where $F_0 = m_B g'$, dF is the zero mean randomly oscillatory component of the tether tension (i.e., magnitude variation), and x is the position of the tether attach point with respect to the vehicle mass center. For the situation where a constant disturbance torque will be applied to the sub-satellite, the steady-state position of the attach point can be described by a nominal constant value and a small, zero mean oscillation about the nominal value. The nominal value will be a function of the disturbance torque magnitude and nominal tether tension value (F_0). Therefore, the attach point position with respect to the sub-satellite mass center can be written as:

$$x = x_0 + \delta x, \tag{4.15}$$

$$x_0 = \frac{T_2}{F_0}, \tag{4.16}$$

where T_2 is the magnitude of the roll torque induced by the momentum stored in the momentum wheel used for yaw control and $\delta x / x_0 \ll 1$. Further, Equations 4.14 and 4.15 can be combined and simplified (ignoring products of small terms) to yield:

$$I\ddot{q} = (F_0 + dF)(x_0 + \delta x) \approx F_0 x + dF\, x_0. \tag{4.17}$$

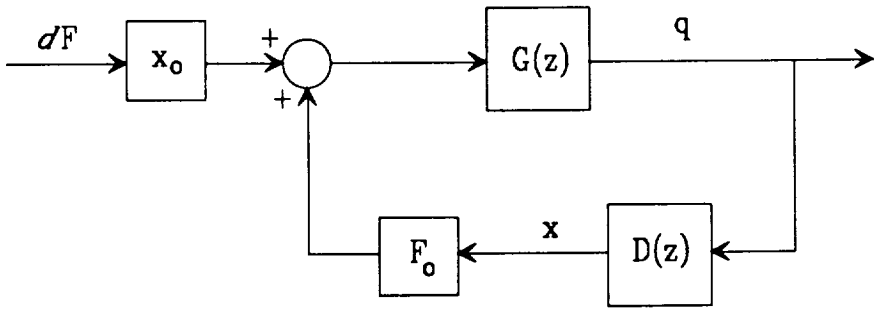

Figure 4.11: Block Diagram of Vehicle Orientation Related to Tether Tension Magnitude Variations

For the regulator case, a compensator transfer function, $D(z)$, between the measured orientation of the vehicle and the attach point position of the tether with respect to the mass center can be derived. Given that compensator transfer function, a transfer function between tension magnitude variations and vehicle orientation can be derived. A block diagram of this system is shown in Figure 4.11. $G(z)$, is the Z-transform transfer function from applied control torque to vehicle orientation. A Bode magnitude plot of the transfer function between q and dF is shown in Figure 4.12 for $G(z)$ given in Equation 3.87, F_0 equal to 2 N (as discussed in Section 2.3), T_2 is 5.5×10^{-5} N-m (as discussed in Section 4.2.1), x_0 can be calculated from Equation 4.16 to be 2.75×10^{-5} m, and $D(z)$ is discussed in Sections 3.2.2 and 3.2.3 and can be expressed approximately as:

$$D(z) = \frac{z(z-0.91)[(z-0.92)^2+(0.07)^2]}{(z-1)(z-0.94)[(z-0.36)^2+(0.36)^2]}. \tag{4.18}$$

The Bode plot shows that for all frequencies, a significant amount of attenuation of tension magnitude variations can be expected. The least amount of attenuation occurs at frequencies very near the closed-loop bandwidth and high levels of attenuation should occur at both high and low frequencies (with respect to the system bandwidth).

A series of experiments were performed to verify the previous analysis and to determine the applicability of the Bode magnitude plot shown in Figure 4.12. The attitude control system was set to respond in the regulator mode, the fan on-board

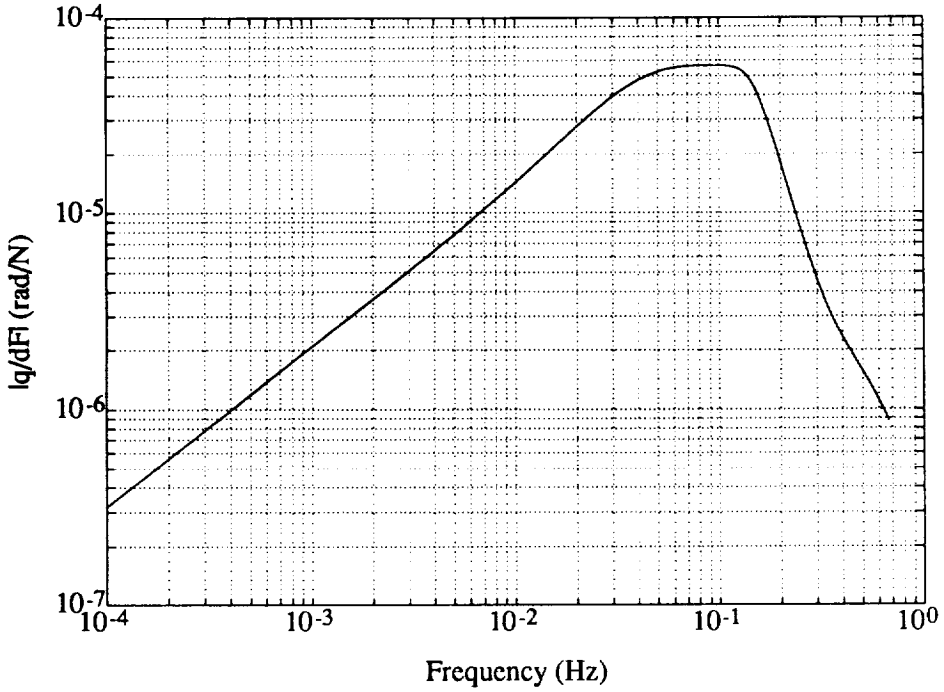

Figure 4.12: Bode Magnitude of Transfer Function Between Tension Magnitude Variations and Vehicle Orientation

the air-bearing vehicle was turned on, and the tether dynamics simulator was used to shake the wall attach point at a specified frequency and amplitude. This procedure was repeated for three different wall motion amplitudes and three different wall motion frequencies. The results were then scaled to reflect the maximum level of disturbance torque expected in the orbital case (i.e., 5.5×10^{-5} N-m) and scaled to be represented as a percentage tension variation as can be calculated from the Bode magnitude plot shown in Figure 4.10. Simultaneously, the load cell on the air-bearing vehicle was employed to verify the Bode magnitude of the transfer function relating tether tension variations to wall attach point motion.

The results of the experiments are summarized in Figure 4.13. Figure 4.13(a) shows three separate frequencies of the wall oscillation: the x and solid line correspond to a wall frequency of 0.017 Hz, the o and dash-dot line correspond to a wall frequency of 0.033 Hz, and the + and dashed line correspond to a wall frequency of 0.067 Hz. The symbols (x, o, and +) correspond to the measured data and the lines (solid, dash-dot, and dashed) correspond to lines fit to the measured data in a

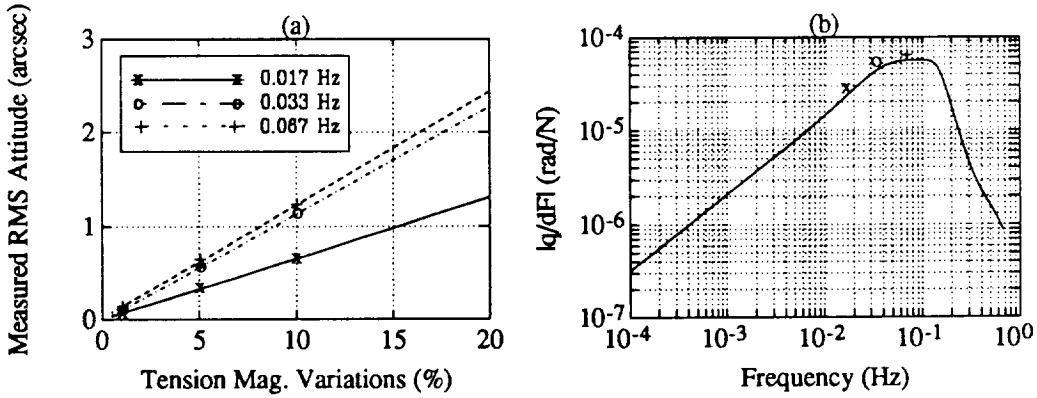

Figure 4.13: Results of Tests With Tension Magnitude Variations and a Disturbance Torque of 5.5×10^{-5} N-m

least squares sense. These three frequencies were chosen with the following reasoning: since the tension magnitude variation frequency for the orbital case, scaled to reflect the difference between the orbital and laboratory bandwidths, is 0.033 Hz, the behavior of the transfer function model at and near this frequency is of greatest interest. Therefore, experiments were performed at that frequency and at frequencies a factor of two both above and below that frequency. This will provide confidence in the transfer function model of the closed-loop system between vehicle angular orientation and tension magnitude variations. In addition, higher frequencies were not chosen be cause of the effect summarized in Figure 4.10. That is, as the oscillation frequency approaches the mass-spring frequency of the laboratory simulator, undesirable behavior will result yielding useless data. Figure 4.13(a) shows that the measured RMS attitude increases linearly with increasing tension variation. The vehicle orientation is affected by torques generated by the product of tension variations and the steady-state attach point offset. As the tension variations increase, it is expected that the attitude errors will also increase. The values of the measured RMS attitude are less than 1 arcsec for tension variations less than about 7.5% of the nominal tether tension.

Further, these data have been superimposed on the same frequency domain plot as is shown in Figure 4.12. This representation is shown as Figure 4.13(b). The solid line corresponds to the Bode magnitude shown in Figure 4.12. The symbols (x, o, and

+) correspond to average values of each of the data taken at the different frequencies. The x, o, and + symbols correspond to the results obtained for wall attach point frequencies 0.017, 0.033, and 0.067 Hz, respectively. The frequency domain plot shows that the experimental data lie within 10% of the theoretical predictions. The data all lie uniformly above the theoretical values which suggests that there is a small discrepancy between the actual DC gain and the calculated DC gain for the transfer function. This discrepancy can arise from any one of a number of sources, including a difference in the value of a calculated physical parameter or a finite effect due to the linearization of a nonlinear process.

Torque Magnitude

As discussed previously, in the orbital case, the magnitude of the disturbance torque applied to the sub-satellite will increase linearly with time (see Section 4.2.1). The frequency response results previously presented all assumed that the disturbance torque was limited to a threshold value (5.5×10^{-5} N-m) by occasionally instigating a maneuver to dump the momentum stored in the yaw axis control momentum wheel. In terms of mission planning, it is very important to understand the effect of allowing various disturbance torque values to persist and to understand the effect that these torque values will have on the long term, fine pointing ability of a tethered sub-satellite. A series of tests were performed with varying torque levels to determine the correlation between the disturbance torque magnitude and steady-state accuracy in the face of tension magnitude variations.

The experiments were performed in the regulator mode, with the on-board fan set to generate the desired torque level, and the tether dynamics simulator configured such that it would generate laboratory tether tension magnitude variations with a frequency equal to the scaled, expected orbital tether natural frequency and with an amplitude equal to 5% of the nominal tension value. The applied torque values were scaled to fit the expected orbital parameters and ranged from 5.5×10^{-5} N-m to 5.5×10^{-4} N-m. The results of these experiments are summarized in Figure 4.14. In the figure, the points marked with an x correspond to actual data points and the solid line represents a line fit to the data in a least squares sense. As would be expected, these

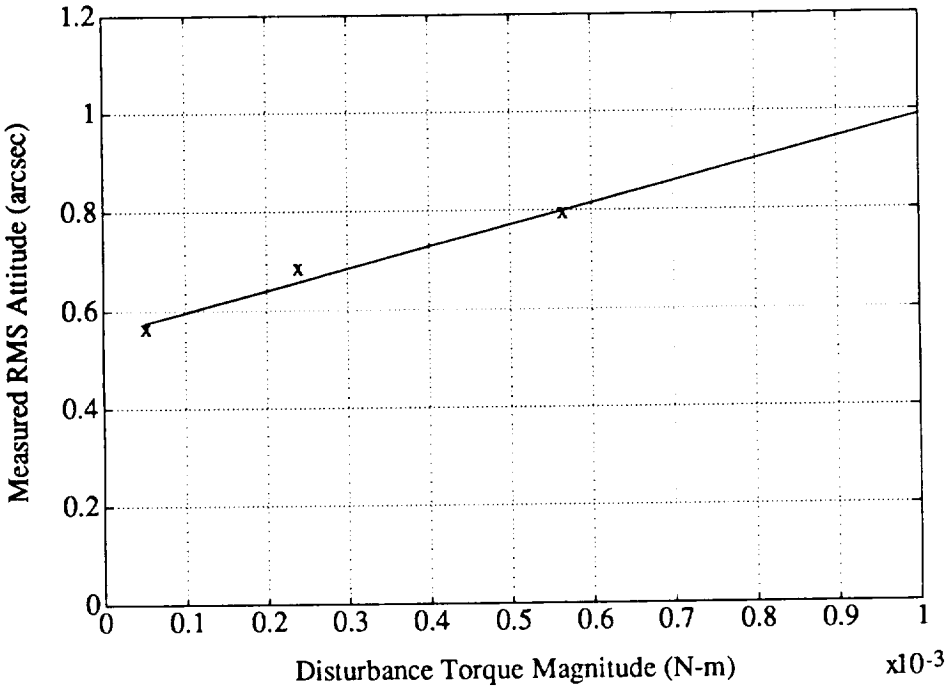

Figure 4.14: Results of Experiments with Varying Levels of Disturbance Torque and 5% Longitudinal Disturbance

data show that the steady-state orientation error due to increased torque values tends to increase. The increase in measured RMS attitude is a result of the fact that with increasing environmental disturbance torques, the moment arm through which tension magnitude variations will generate attitude errors, also increases. The moment arm is essentially the steady-state value of the displacement of the attach point with respect to the vehicle mass center and, as shown in Equation 4.16, it is linearly dependent on the magnitude of the disturbance torque. In addition, Figure 4.14 provides a convenient method for determining the direct effect of various levels of disturbance torque on steady-state orientation control. It shows that for disturbance torque magnitudes less than about 1×10^{-3} N-m, the expected steady-state attitude regulation will be less than 1 arcsec.

4.2.4 Tether Force Direction Variations

Much of the introductory discussion of tether force magnitude variations in Section 4.2.3 holds for direction variations as well, with a few notable modifications. The goal of the following sections is to determine the behavior of the tethered satellite attitude control system when the force applied to the sub-satellite simulator varies in direction only. Once again, the model developed by He [31] has been employed to determine the dominant frequencies of tether tension direction variations expected in the orbital configuration and these frequencies were used to determine the appropriate laboratory wall attach point oscillation frequencies. With this information available, the tether dynamics simulator discussed in Section 2.2 can be employed to vary the tether tension direction in a manner consistent with the expected orbital behavior. The tether dynamics simulator will be configured such that the wall attach point will oscillate in the direction perpendicular to the nominal tether direction, thereby forcing pendular motions of the laboratory simulator.

Laboratory Simulation

The simulation of tether force direction variations proceeds much the same way as for the simulation of tether magnitude variations. The goal is to make the short laboratory tether apply lateral variations which are the same as those expected from a 2 km long space-based tether. For the simulation of tether force direction variations, the laboratory configuration can be modeled simply as a pendulum which possesses significant rotational inertia (by ignoring the compliance of the tether and any forces exerted on the air-bearing vehicle due to the flotation system). A diagram of this model is shown in Figure 4.15. In the figure, L_l is the tether length, m is the vehicle mass, I is the principal moment of inertia of $\mathbf{B}$ for the mass center, g' is the micro-gravity acceleration, μ is the angle between the tether and the local vertical, and w is the motion of the tether dynamics simulator in a direction perpendicular to the nominal micro-gravity field. A simple dynamic analysis will reveal that the transfer function, $H_{\mu w}(s)$, between wall motions (w) and the angle of the tether with respect

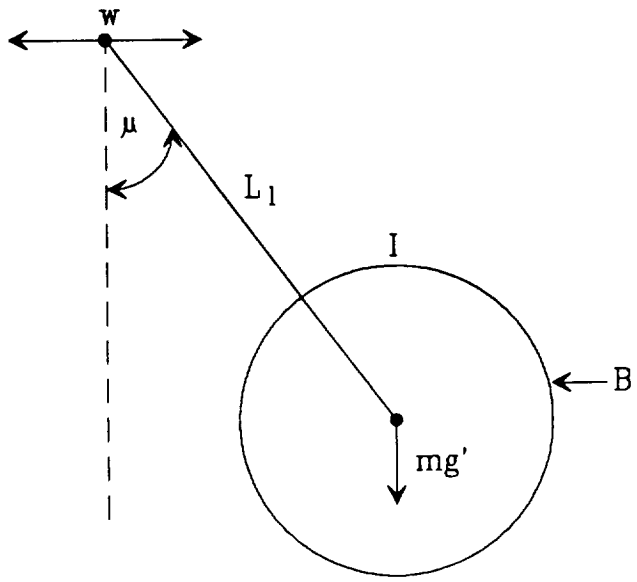

Figure 4.15: Simplified Lateral Tether Model for Simulations

to local vertical (μ) is given by:

$$H_{\mu w}(s) = \frac{-mL_l^2 s^2}{(mL_l^2 + I)s^2 + mg'L_l}, \tag{4.19}$$

where s is the Laplace Transform variable. After substituting the appropriate values for the physical parameters (i.e., I = 30 kg-m^2, g' = 0.008 m/s^{-2}, m = 250 kg, L_l = 2 m), a Bode magnitude plot can be drawn which relates the magnitude of the angle μ to the magnitude of the wall motion w, versus frequency. Figure 4.16 shows the Bode magnitude plot of the transfer function shown in Equation 4.19. The magnitude of the angle between the tether and the local vertical is dependent on the magnitude of the input motion at the wall and the frequency of oscillation of the attach point. For low wall motion frequencies (i.e., less than the pendular natural frequency), the angle between the tether and the local vertical is approximately zero. For high frequencies (above the natural pendular frequency), the tether angle with respect to local vertical is constant (and is approximately equal to w/L_l). In the actual laboratory implementation, this claim is not strictly true. There will be a small angle variation due to the motion of the attach point on the sub-satellite, which is on

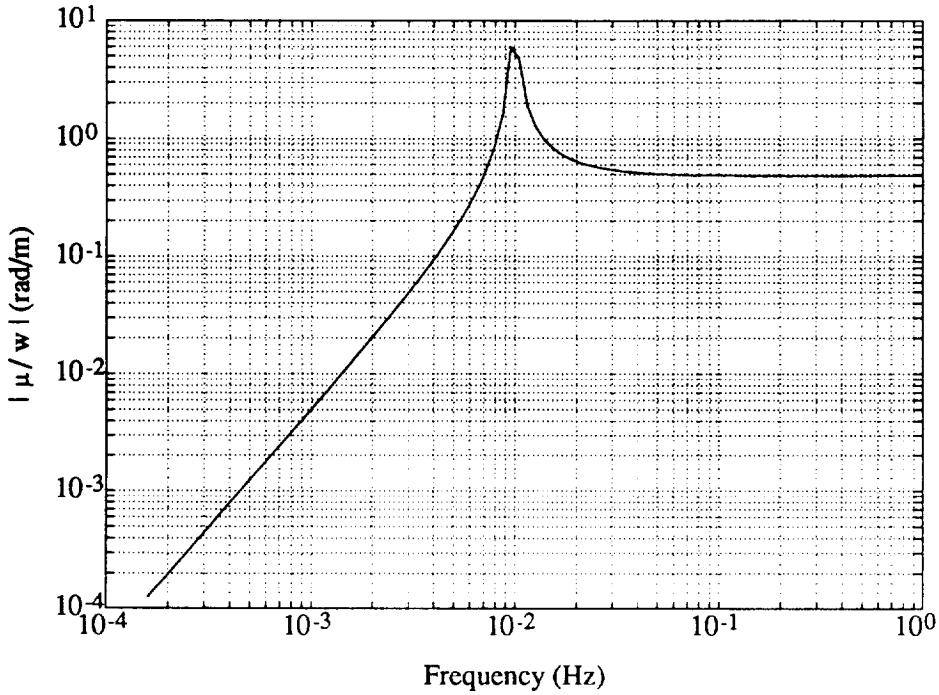

Figure 4.16: Bode Magnitude of Tension Direction Variations to Wall Input Motion

the order of 10^{-4} rad for a typical fine pointing maneuver. At the pendular natural frequency, the tether angle grows to be very large for very small wall motions. This Bode plot allows the derivation of the necessary tether dynamics simulator motion in order to simulate tether force direction variations as would be expected in a long, space-based tether as follows:

1. By using the mathematical and computer model developed by He [31], determine the lowest frequency of tether force direction variations which result from the natural behavior of the space-based tether.

2. Scale this frequency appropriately to determine the necessary wall attach point oscillation frequency in order to simulate the expected orbital tether force direction variations. The appropriate scaling is determined (as was the case for simulating tether tension magnitude variations) by forming the ratio of laboratory bandwidth and orbital configuration bandwidth. This serves to freeze the separation, in the frequency domain, between the variation frequency and the system bandwidth.

3. Use the Bode diagram shown in Figure 4.16 to determine the relationship between the wall attach point amplitude and the tether tension direction variation (μ). Then, given a desired variation magnitude, it is a simple matter to determine the necessary wall attach point motion to achieve the desired tension direction variation.

The results of this procedure for the systems of interest yields a wall attach point oscillation frequency of 0.01 Hz. Since this is the natural frequency of the pendular system, very small wall attach point motions will be necessary in order to achieve the proper angular variations in tether direction. While this is not the ideal case, it is still reasonable to expect acceptable behavior of the magnitude of the angular variations of the tether force. To maintain the necessary accuracy, however, the actual angle variation to wall motion was measured so that the unmodeled viscous effects of the air-bearing, which will become significant in this case, could be quantified.

Frequency Response

As was the case for the consideration of tether force magnitude variations, the effect of tether tension direction variations on the performance of an attitude control system based on a movable sub-satellite attach point can be summarized by quantifying a transfer function between tension direction variations and measured attitude stability. With this transfer function available, a model of the tether dynamics can be used to determine the performance of the system by calculating the expected in-plane lateral behavior of the tether and applying those results to the transfer functions relating attitude performance to lateral and longitudinal tether disturbances (see Section 4.2.5). The following section describes the experimental results obtained by introducing tether force direction variations at various frequencies to the laboratory simulator attitude control system.

The differential equation of rotational motion of the sub-satellite was derived previously and is repeated in Equation 4.13. While performing high accuracy attitude regulation in addition to simulating tether force direction variations, it can be seen that q and $\dot{q}$ are both small and that, with the mass center estimator operational, d

will be zero. In this case, the differential equation can be simplified to yield (using the trigonometric identity $\cos(a-b) = c_a c_b + s_a s_b$):

$$I\ddot{q} = |\underline{F}_t| x \cos(\mu - q). \tag{4.20}$$

While simulating tether tension direction variations, it can be assumed (with reference to Equation 3.78) that the tether tension magnitude is approximately constant (i.e., $|\underline{F}_t| \approx F_0$). Also, x can be written as in Equations 4.15 and 4.16 to emphasize the steady component and a zero mean value superimposed on the nominal value. In addition, the following approximation can be made:

$$\cos(\mu - q) \approx \cos d\mu \approx 1 - \frac{d\mu^2}{2}, \tag{4.21}$$

where $d\mu$ is the (small) tether tension direction variation. With these three approximations, the equation of rotational motion of the laboratory simulator for tether tension direction variations can be written as:

$$I\ddot{q} = F_0(x_0 + \delta x)(1 - \frac{d\mu^2}{2}). \tag{4.22}$$

This equation can be simplified (by ignoring small terms raised to the third power) and can be approximated to be:

$$I\ddot{q} = F_0 x - F_0 x_0 \frac{d\mu^2}{2}. \tag{4.23}$$

For the regulator case, a transfer function (of the compensator) between the measured vehicle orientation and the attach point position, $D(z)$, can be calculated and is shown in Equation 4.18. With this compensator transfer function, a nonlinear relationship between tether tension direction variations and vehicle orientation can be derived. A block diagram of this system is shown in Figure 4.17. A Bode magnitude plot of the transfer function between q and ν is shown in Figure 4.18 (ν was chosen as the input because it allows a linear transfer function to be drawn). The values of $G(z)$, F_0, T_2, and x_0 are the same as those used for the tension magnitude variation transfer function. The Bode plot shows that for all frequencies, a significant amount of attenuation of tension direction variations can be expected (for sufficiently small

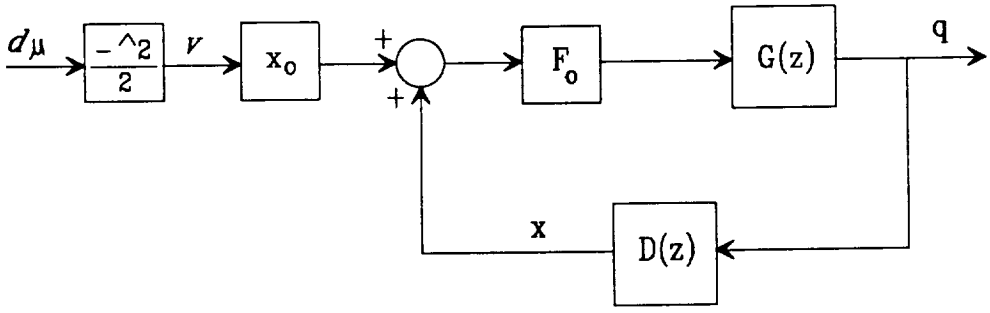

Figure 4.17: Block Diagram of Vehicle Orientation Related to Tether Tension Direction Variations

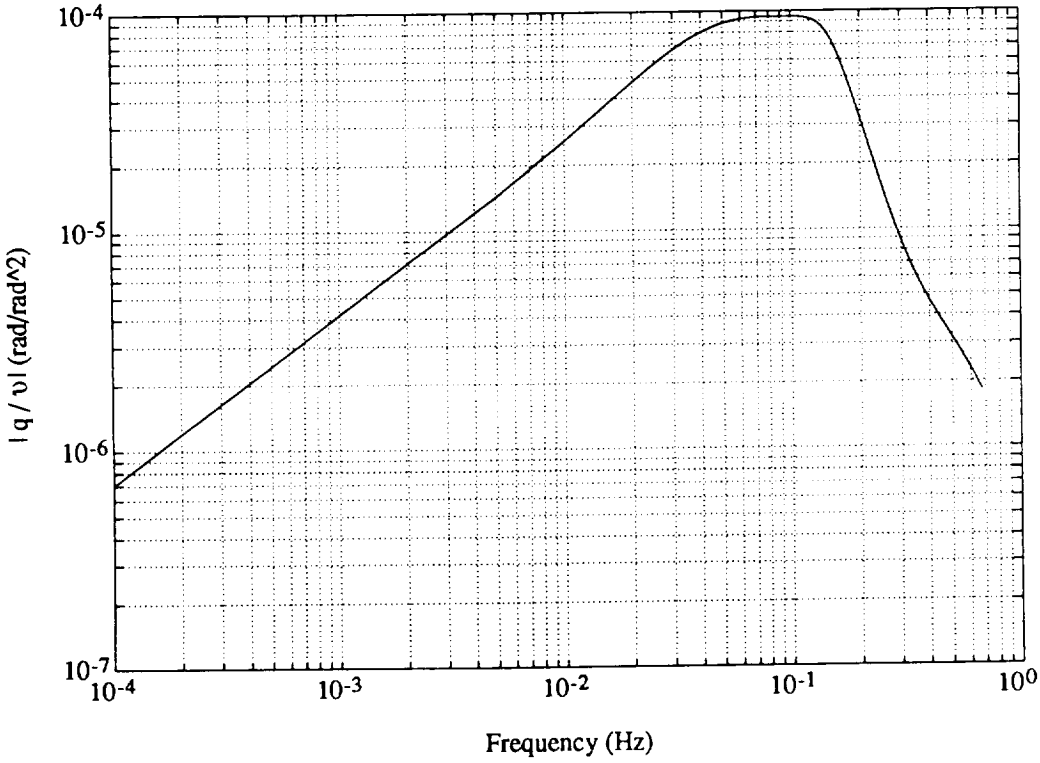

Figure 4.18: Bode Magnitude of Transfer Function Between Tension Direction Variations and Vehicle Orientation

values). The least amount of attenuation occurs at frequencies near the closed-loop bandwidth and high levels of attenuation occur at frequencies both above and below the bandwidth.

Experiments were performed to provide experimental verification of the above analysis so that the applicability of the frequency response plot of Figure 4.18 could be determined. The experiments were performed with the control system in regulator mode, turning on the on-board fan, and using the tether dynamics simulator to force oscillatory direction variations of the tether tension. In order to provide results which are independent of the expected orbital KITE configuration (i.e., only dependent upon dimensionless quantities), the correspondence between the laboratory simulation and the expected on orbit tether behavior is summarized in Figure 4.19. Due to the short tether in the laboratory and, therefore, the very high frequencies of the natural laboratory lateral tether dynamics, it is assumed that significant tension direction variations occur as a result of the forced (by the tether dynamics simulator) pendular motion. As a result, the entire laboratory tether is used to simulate the 2 m of the space tether which is immediately adjacent to the sub-satellite (i.e., the actual curvature is approximated as a straight line). In order to nondimensionalize the lateral behavior, the amplitude of the wall motion is related to the amplitude of the corresponding orbital lateral mode shape (assumed to be a half sine wave), and scaled by a characteristic length of the given configuration. Mathematically, this can be described by the following ratio:

$$\frac{w}{L_l} = \frac{W}{L_o}, \tag{4.24}$$

where w is the transverse wall attach point motion, W is the maximum amplitude of the lateral mode shape for the orbital tether, and L_l and $2L_o$ are the lengths of the laboratory and orbital tethers, respectively. Therefore, the tether direction variations can be expressed as a percentage of orbital tether half-length (because the tension direction variation, $d\mu$, can be related to a specific orbital lateral mode shape amplitude, W, which can be determined from the percentage of tether half-length for any length tether).

The results of the experiments with a constant disturbance torque (scaled to the

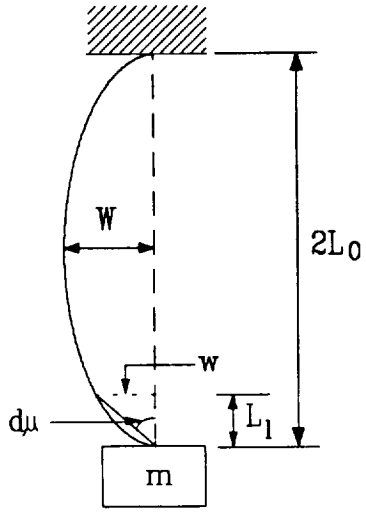

Figure 4.19: Correspondence Between Laboratory and Orbital Tension Direction Variations

maximum expected orbital disturbance torque of 5.5×10^{-5} N-m) and various levels of tension direction variations as judged by the percent of tether half-length are shown in Figure 4.20. In the figure, the x, o, and + represent actual, scaled (to reflect the orbital conditions) measured data points, and the lines (solid, dashed, and dash-dot) are the straight line fits to these data in the least squares sense. Each line and symbol represents data for a different wall oscillation frequency: the x and solid line correspond to 0.01 Hz, the o and dashed line correspond to 0.02 Hz, and the + and dash-dot line correspond to 0.03 Hz. These three frequencies were chosen because the lowest frequency corresponds to the scaled, lowest order lateral frequency as is calculated from the methodology developed by He [31] for the nominal KITE configuration. The other frequencies were chosen as corresponding to the second and third lateral modes of the KITE orbital configuration. Since the lowest modes will have the greatest contribution to the overall response, this section of the frequency response shown in Figure 4.18 is most critical to verify accurately. The results summarized, in Figure 4.20(a), show that the value of measured, steady-state orientation increased with increased tension direction variations. This result is fully expected, since, for a constant disturbance torque, the steady-state offset of the attach point from the

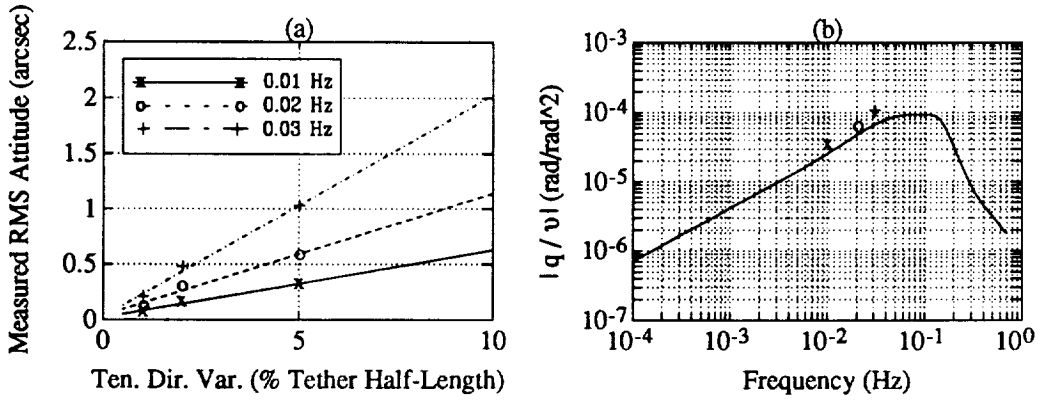

Figure 4.20: Results of Tests with Tension Direction Variations

actual mass center location will be a constant. This constant value is the moment arm through which tension variations will generate attitude errors. As a result, increased tension variations will increase the values of the measured steady-state orientation. Figure 4.20(a) also indicates that there is a correlation between tension direction variation disturbance frequency and level of orientation error. This same phenomenon was observed in the case of tension magnitude variations. As the tether disturbance frequency (either magnitude or direction) approaches the closed-loop bandwidth of the system, tether tension disturbances have a greater effect.

In addition, these data have been superimposed on the frequency response curve presented in Figure 4.18. The result is shown in Figure 4.20(b). In the figure, the solid curve represents the theoretical frequency response calculated above and the symbols, x, o, and +, correspond to average values of the data measured at each of the experimental frequencies. The figure shows that the laboratory results do confirm the theoretical analysis. Each of the data points is within 10% of the theoretical curve and they all lie uniformly above the expected solid curve. This suggests that there is a gain mismatch between the system model and the laboratory hardware (which was also observed in the results of the tension magnitude variations).

Torque Magnitude

It is convenient, for mission planning purposes, to determine the effect of various levels of persistent disturbance torques applied to the vehicle with closed-loop attitude

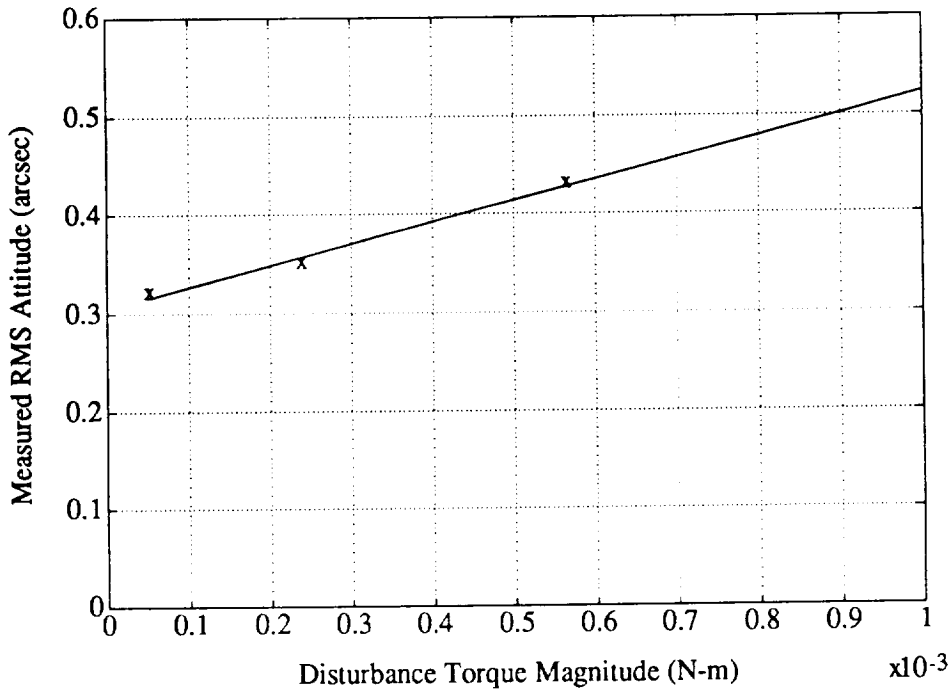

Figure 4.21: Results of Experiments with Varying Levels of Disturbance Torque and 5% Tether Half-Length Tension Direction Variations

regulation. This information is useful in the timing of momentum wheel desaturation maneuvers and the attitude regulation requirements for different phases of the total mission. The previous experiments were performed with one, constant level of disturbance torque applied to the sub-satellite. As was derived in Section 4.2.1, the actual level of external disturbance torque applied to a tethered vehicle sub-satellite will increase linearly with time. In designing the previous experiments, it was assumed that the magnitude of the external disturbance torque could be limited by performing a momentum dump maneuver for the yaw momentum wheel. The level of the disturbance was assumed to be a reasonable value given typical mission requirements. However, to provide a complete description of the effect of lateral tether dynamics, it is desirable to investigate and quantify the ramifications of various levels of external disturbance torque. This knowledge will provide mission planners with a good idea of the necessity and timing of momentum dump maneuvers and will give them the flexibility to vary the specific torque levels during the course of a mission.

The experiments were performed with the control system in the regulator mode,

with the on-board fan blowing such that it generated the desired disturbance torque level, and the tether dynamics simulator was set to provide a tension direction variation amplitude scaled to a value which corresponds to a lateral modal amplitude of 5% of the tether half-length. The scaled values of the disturbance torque ranged from 5.5×10^{-5} N-m to 5.5×10^{-4} N-m. Figure 4.21 shows the results of these experiments. In the figure, the x symbols correspond to actual, measured data points, and the solid line corresponds to the straight line fit, in the least squares sense, of the data. As would be expected, the measured RMS attitude increases with increased disturbance torque. The moment arm through which tether disturbances act to generate attitude errors is proportional to the level of external disturbance applied to the vehicle. Therefore, greater levels of disturbance torque can be expected to generate greater levels of measured attitude errors when the tether tension direction introduces variations in the amount of force useful (and modeled) for attitude control purposes. As mentioned previously, Figure 4.21 also provides a convenient guide to determine the direct effect of persistent levels of external disturbances applied to the vehicle. The figure shows that for disturbance torque levels less than 0.8×10^{-3} N-m, the effect of lateral tether disturbances will not effect the ability of the attitude control system to regulate the orientation to less than 0.5 arcsec.

4.2.5 Effect of Longitudinal and Lateral Tether Dynamics

The previous two sections discussed the theoretical development and experimental program which serves to describe the behavior of the closed-loop tethered satellite attitude control system based on a movable tether attach point when tether tension (magnitude and direction) variations are considered. The purpose of these sections (i.e., Sections 4.2.3 and 4.2.4) is to provide the necessary background in order to consider the effect of realistic tether dynamics on the performance of the control system. The tether dynamics of interest include the orbital lowest order (mass-spring mode) longitudinal oscillations and the lowest order lateral (vibrating string) mode. These dynamics dominate the variations in tether tension as was concluded by He [31]. This section will combine the theoretical development of the tether dynamics model derived by He [31], with the experimental results that were presented in Sections 4.2.3

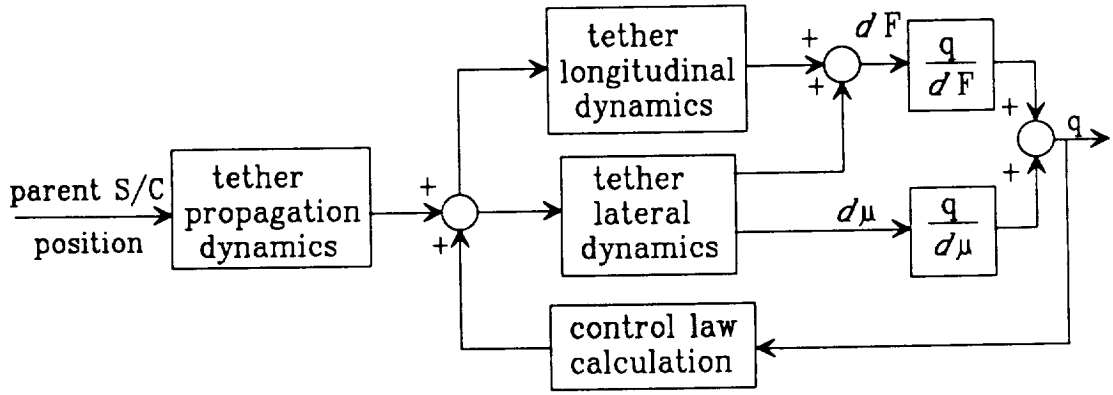

Figure 4.22: Block Diagram of Longitudinal and Lateral Tether Dynamics

and 4.2.4 above.

Tether longitudinal dynamics are wholly described by tension magnitude variations and tether lateral dynamics are described by a combination of tension direction variations (which result from the swinging motion of the vibrating string mode) and tension magnitude variations (which result from the stretching of the tether present when it vibrates like a string). Figure 4.22 shows a block diagram representation of the effects of longitudinal and lateral tether dynamics on tethered satellite pointing errors. The figure shows that the parent spacecraft inertial position (filtered by the propagation dynamics of the tether) added to the inertial tether attach point position (generated from the control law calculation and the sub-satellite translational dynamics) are combined to form the input to both the longitudinal and lateral tether dynamics. These tether dynamics convert the end body motions to tether tension variations. The longitudinal dynamics generate solely tension magnitude variations and the lateral dynamics create tension direction and magnitude variations. The total magnitude variation (from the sum of longitudinal and lateral dynamics), dF, and the total direction variation, $d\mu$, are inputs to the transfer functions (derived in the previous sections) which relate attitude errors to variations in tension magnitude and direction, respectively. These errors can then be combined to determine the total expected attitude error due to tether dynamics.

The equations which should be put into the three tether dynamics boxes (propagation, longitudinal, and lateral) can be found in the dissertation by He [31]. In this work, Chapter 4 derives, in detail, the necessary transfer functions, and Appendix B shows a block diagram representation of the tether system. Due to the complexity of the relationships and in the interest of saving space, the relationships are not repeated here, and the reader is encouraged to review the material developed by He [31]. The transfer functions which relate tension magnitude variations and tension direction variations can be found in Sections 4.2.3 and 4.2.4 above, and are shown in frequency response form in Figures 4.12 and 4.18. With this information, any tethered satellite configuration can be described mathematically and the pointing errors can be predicted.

The immediate concern is to predict the behavior of the KITE configuration tethered satellite using the mathematical machinery described above. The tether model is based on the parameters of a TSS-1 (Tethered Satellite System 1, a proposed Space Shuttle flight test) tether and is described in detail by He [31]. Combining this information and performing the necessary computer simulation in MATRIXx yields the expected behavior of the tether dynamics. The results of the simulation show that in the orbital KITE configuration, the tether tension magnitude can be expected to vary with an amplitude which equals approximately 5% of the nominal tension value and at a frequency (scaled to reflect the lower bandwidth of the orbital case) equal to 0.033 Hz. Applying this level of tension magnitude variation (which is the result of both longitudinal and lateral tension magnitude variations) to the transfer function relating magnitude variations to attitude errors shows that at the given frequency and amplitude (see Figure 4.13(a)) the expected orientation errors due to the magnitude variations is less than 0.75 arcsec. In addition, the simulation also shows that the tether tension direction can be expected to vary with a frequency (scaled to reflect the lower bandwidth in the orbital case) of 0.01 Hz, with an amplitude equivalent to a vibrating string mode shape (assumed to be a half sine wave) which possesses an amplitude which will be less than 5% of the tether half-length. Applying this level of tension direction variation to the transfer function relating attitude errors to tension direction variations shows that, for the calculated amplitude and

frequency, expected attitude errors (see Figure 4.20(a)) are bounded by 1.0 arcsec. Therefore, the combination of tension magnitude and direction variations which result from tether longitudinal and lateral dynamics will be bounded by approximately 0.85 arcsec. As a result, it can be concluded that tether dynamics will not effect the ability of the control algorithm to perform tethered satellite attitude control with an accuracy greater then 1 arcsec.

4.2.6 Effect of Center of Mass Estimation

The previous sections discussed the case where orbital tether dynamics (in the form of tension magnitude and direction variations) were simulated with the tether dynamics simulator. The effect that these dynamics had on the steady-state attitude regulation of the closed-loop system was quantified. These studies provided insight to the effect of various external disturbance torque levels on the performance of the full attitude control scheme. For the case of fine pointing in a disturbance-free environment, a series of experiments were designed to determine just how effective and necessary the mass center estimate is in order to implement a useful tethered satellite attitude control system based on a movable attach point (see Section 4.1.4). While in orbit, such an orientation control system will be subjected to external disturbances, so it will prove useful to conduct a similar study for the situation where the tether dynamics are simulated.

The basic theory behind this question can be understood by modifying the two previously derived relations for the dynamic behavior of the expected attitude errors which result from tension magnitude and direction disturbances (see Equations 4.17 and 4.23). These differential equations can be modified to include the effect of turning off the mass center estimator as follows:

$$I\ddot{q} = F_0(x+d) + dF\,x_0, \tag{4.25}$$

$$I\ddot{q} = F_0(x+d) - F_0 x_0 \frac{d\mu^2}{2}, \tag{4.26}$$

where Equation 4.25 refers to the case with tension magnitude variations and Equation 4.26 refers to the case with tension direction variations. These two equations

can be recognized as possessing the same form as Equations 4.17 and 4.23, with the added complication of a second input, d, the mass center offset. The angular response, then, is the result of a combination of the tension variation (in magnitude or direction) and the steady mass center misalignment. It should be noted, that these equations (4.25 and 4.26) can be expressed in block diagram form similar to those shown in Figures 4.11 and 4.17, respectively (with a modified transfer function for $D(z)$ to reflect the compensator without mass center estimation). Once in that form, a simulation of the system can be performed with MATRIXx System Build for a given mass center offset and tension variation time history, and the results compared to the actual observed behavior in the laboratory. This procedure was followed for one set of tension variation time histories and four different mass center offsets for both cases (i.e., magnitude and direction variations).

The experiments to test the effectiveness of the mass center estimate in conjunction with an external disturbance and the simulation of tether dynamics were performed with the control system described in Section 4.1.4. The ratio of noise covariances (R_d/Q) was set equal to 5.0 in order to calculate the Kalman Filter gains. This ratio of noise to process covariances corresponded to the 'best' behavior observed in the disturbance-free experiments. The external disturbance torque was introduced with the on-board fan and calibrated such that the scaled torque generated by the fan would be 5.5×10^{-5} N-m (which is the previously discussed maximum disturbance torque limit). When simulating tension magnitude variations, the tether dynamics simulator was adjusted to vary the magnitude 5% of the nominal value at the expected orbital mass-spring frequency and when simulating tension direction variations, the simulator was set to correspond to an orbital lateral modal amplitude equivalent to 2% of the tether half-length with a frequency equivalent to the lowest order orbital string vibration frequency. The results of both the tension magnitude and direction variation cases of the experiments and simulations are shown in Figures 4.23(a) and (b), respectively. In the figures, the x symbols correspond to the measured results and the o symbols correspond to the results obtained from the MATRIXx simulation. The results show that for both types of tether tension variations, the effect of no mass center estimation on steady-state attitude regulation is to increase errors with increasing

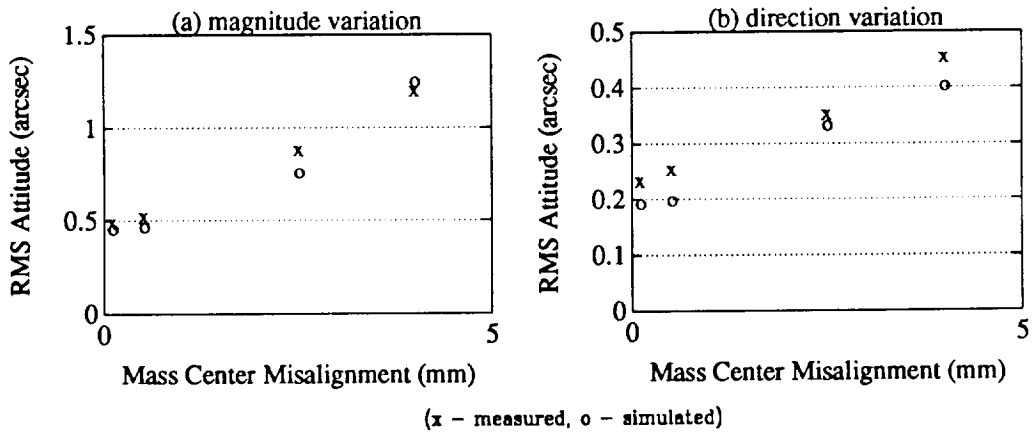

Figure 4.23: Experimental Results without Mass Center Estimation, with Tether Tension Variations, and with a Constant External Disturbance of 5.5×10^{-5} N-m

mass center misalignment. This result is shown for both the laboratory experiments and the computer simulations and is fully expected from the theoretical development. Physically, for values of misalignment (d) which are less than the nominal, steady-state offset of the attach point from the mass center (x_0), the largest pointing errors will be introduced by the tension variations (multiplied by the external disturbance generated offset, x_0). However, when the misalignment (d) is much greater than the steady-state, nominal value of the attach point (x_0), the largest pointing errors will be generated by the mass center misalignment, d, multiplied by the nominal tether tension value, F_0. Between these two situations, there is a transition region which shows the effects of both sources of pointing errors. The figures also show that, for cases where the mass center is in the plane of attach point motion, the tension magnitude variations have a greater effect on the performance than do the direction variations (as is exhibited by the larger values of pointing errors). This behavior is also to be expected. From Equation 4.13, it is clear that tension magnitude variations have a direct effect on the torque (control plus disturbance) applied to the vehicle, while tension direction variations effect the total torque through the cosine of the angle, and for relatively small angles (less than about 20 deg), there is very little change in the value of the cosine term.

Finally, it should be noted that for a typical space mission, the mass center uncertainty will be on the order of 1% of the spacecraft characteristic dimension. The laboratory tests have been performed with mass center misalignments between 0.01% and 0.4% of the simulator diameter. The results of the previous study show that even for center of mass misalignments as small as these, significant errors can be introduced by not estimating the mass center location. It is clear that larger mass center errors will only increase pointing errors unless mass center estimation is part of a attitude control algorithm based on a movable tether attach point.

4.2.7 Tension Feedback

The previous results suggest that for the sub-satellite attitude control system based on a movable tether attach point, the pointing errors introduced by the inclusion of longitudinal and lateral in-plane tether dynamics will be small enough that a 1 arcsec mission requirement can be met. The linearized equations of motion of a tethered sub-satellite were derived in Section 3.1.3. Near the end of that section, it was claimed (with reference to Lemke [42]) that for instances when either q (the vehicle orientation) is not small, or when dF (the tether tension variation) is on the same order of magnitude as the nominal tension value, F_0, the control algorithm could be modified to calculate the actual tether attach point offset by scaling the desired value by the expression shown in Equation 3.85. In an effort to determine the effect of such a scaling, a series of experiments were performed which judged and quantified the effect.

The experiments were performed with the on-board fan blowing, the tether dynamics simulator operational, and the long-term, high accuracy attitude control system in the regulator mode. The fan provided a scaled external disturbance torque equal to 5.5×10^{-5} N-m. For the tests with tension magnitude variations, the tether dynamics simulator was set to vary the tether tension 5% of the nominal value, and for the tests with tension direction variations, the tether dynamics simulator was set to vary the tension direction with an amplitude which would result from a lateral mode amplitude of 5% of the tether half-length. The same control algorithm as discussed previously was implemented, except that a real-time tension measurement (with the

load cell discussed in Section 2.1.5) was performed and that measurement was used to scale the calculated, desired tether attach point with respect to the vehicle mass center. The results of these tests are summarized in Figure 4.24. Figure 4.24(a) shows the results for the case with tension magnitude variations and Figure 4.24(b) shows the results for the case with tension direction variations. In each graph, the x symbols are the actual data points for the case without the tension scaling, and the o symbols correspond to the measured data for the tests with the previously discussed tension scaling. The figures show that the tension scaling had the effect of lowering the measured steady-state attitude. The results for the case with tension magnitude variations showed a some improvement (approximately 10%) while the results for the case with tension direction variations showed much less (less than 2.5%) improvement. This situation arises from the fact that the load cell measures normal loads only. Since the tension magnitude variations occur only normal to the tether attach point, the tension measurement will directly reflect the significant changes in the tether tension. The tension direction variations, on the other hand, occur parallel to the load cell and the measurement will only record a cosine of the angle change. As a result, it is fully expected that the results with magnitude variations would show much better improvement than those with direction variations. The results for the tension direction variations can likely be improved by including a direct measurement of the angle between the tether and the attach point plane of motion. This angle measurement, in conjunction with the normal load cell measurement and a good model of the tether (a state estimator), will provide even more detailed knowledge of the tether behavior to the control system. This knowledge can then be incorporated to design an attitude control system with long term pointing ability which is accurate to 1 arcsec in environments with greater disturbance torques than those postulated above.

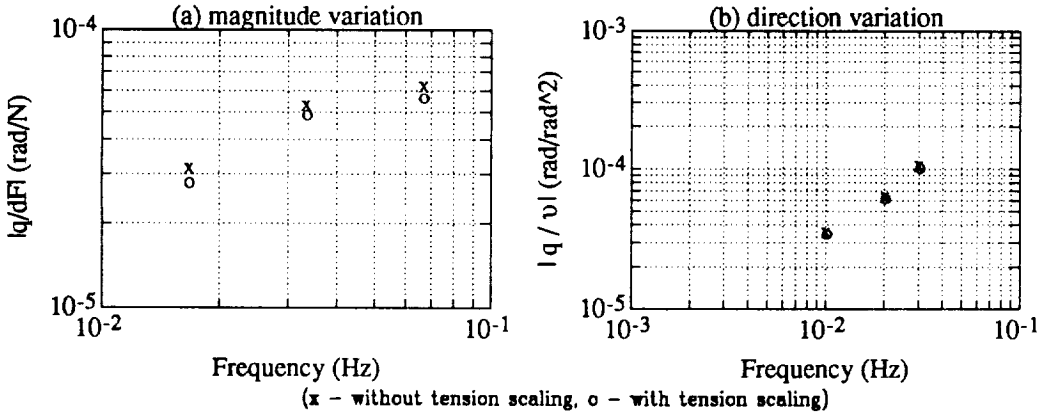

Figure 4.24: Results of Tests with Real-Time Tension Scaling for (a) Tension Magnitude Variation of 5% and (b) Tension Direction Variation Equivalent to a Lateral Mode Amplitude of 5% of Tether Half-Length

Chapter 5

Conclusions

The unique dynamic characteristics of tethered spacecraft make them well suited to serve as isolation platforms for space-based observatories. For missions requiring better than 1 deg long term stability, conventional means of performing the orientation control of a tethered sub-satellite are ineffective because of the relatively large tension force applied to the satellite by the tether. It has previously been shown that generating control torques by varying the tether attach point with respect to the sub-satellite mass center is not only effective, but also necessary for missions with attitude stability requirements on the order of 1 arcsec. This dissertation describes experimental results from a laboratory simulation of a proposed Space Shuttle flight test of a tethered observation platform and relates the results to the orbital configuration to predict attitude stability.

The flight test mission is to consist of a demonstration of a large angle slew maneuver (to exhibit the ability to reorient between multiple targets) and long term, precision attitude control (to exhibit the necessary steady-state attitude stability for observational purposes). These large dynamic range requirements led to the design of separate large angle slew and fine pointing control algorithms. Each of the control schemes generates control moments by varying the sub-satellite tether attach point with respect to the satellite mass center. The large angle slew controller consists of a lead-lag compensator with integral control. The fine pointing control algorithm is a Linear Quadratic Gaussian, full-state feedback control law in conjunction with a

multi-variable Kalman Filter. The control law includes the integral of the vehicle orientation angle as an augmented state and an approximation of the dynamics of the nonlinear actuator (used to position the tether attach point). The Kalman Filter includes the rotational dynamics of the satellite, plus a mass center estimator which is used to calculate, in real time, the actual position of the sub-satellite center of mass.

In order to test each of the control algorithms, a laboratory simulator of a tethered sub-satellite has been designed and constructed. The simulator consists of an air-bearing vehicle upon which all of the necessary hardware to implement the attitude control algorithms has been mounted. The hardware consists of a flotation system, a self-contained power system, a positioning table and stepper motor which serve as the actuator, a computer and communication system, and a system of sensors. The air-bearing is suspended in a micro-gravity field (by tilting the table upon which it floats with respect to local gravity) and connected with a tether to a nearby wall.

An experimental program using the laboratory simulator was designed to test each of the control algorithms. All of the tests were performed in the regulator mode (i.e., the zeroing of initial conditions). The experimental results for the large angle slew maneuver showed that the control law reduced an initial angular displacement of 21 deg to an RMS value of 0.1 deg. The closed-loop system exhibited 18 percent overshoot and a natural frequency of approximately 0.04 Hz. Each of these results compare well with the expected behavior as determined from analysis and computer simulation. The fine pointing experimental results showed that the initial angular displacement was reduced to 0.60 arc-sec RMS in less than 100 sec. The closed-loop bandwidth is approximately 0.03 Hz with overshoot on the order of 5 percent. The state estimator functioned in such a way that the estimate of the angular orientation had an RMS value of 0.75 arc-sec, which is sensor limited. These results again agree quite well with both the theoretical analysis and computer simulation of the closed-loop system.

Further tests were performed to judge the effect of the magnitude of the estimator gains, the need for the mass center estimator, and the effect that various actuator models had on the steady-state control algorithm behavior. The results show that the magnitude of the estimator gains (i.e., the ratio of sensor and process noise models)

do have an effect on the system performance. Relatively poor estimator and system performance were observed for estimator gains which corresponded to too great a reliance on the measurement or too great a reliance on the model. Estimator gains based on a proper balance between sensor and process noise exhibited acceptable estimator performance. In addition, if the estimator root locations corresponded to faster response times than the control root locations, the closed-loop system behaved quite well. The results of the tests of the mass center estimator showed that mass center estimation is necessary for a precision tethered satellite attitude control system based on a movable tether attach point. The magnitude of the effect of not estimating the mass center location was found to depend on the magnitude of the estimator gains and the misalignment between the assumed and the actual mass center locations. The results related to the model of the nonlinear actuator emphasized the fact that care must be taken when modeling nonlinear devices with linear equations. All of the tests verified that closed-loop behavior could be predicted analytically, however, the estimator performance varied considerably.

In the orbital configuration, control moments can be generated by varying the tether attach point for the pitch and roll axes only. It has been proposed that secular yaw disturbance torques can be controlled with the aide of a momentum wheel mounted parallel to the tether axis. As the speed of the momentum wheel increases, the wheel angular momentum will generate a roll disturbance torque which needs to be balanced by a steady-state offset of the tether attach point with respect to the mass center. As the natural dynamics of the tether induce tension magnitude and direction variations, disturbance torques can be generated. To test the ability of the fine pointing control law to reject these disturbances, a tether dynamics simulator was designed and constructed. A fan is used to apply a constant disturbance to the satellite simulator (which is the magnitude of the orbital roll torque limited by a periodic desaturation maneuver) and tension magnitude and direction variations are generated with the tether dynamics simulator.

In the steady-state, longitudinal tether dynamics will converge to the mass-spring mode of the tether/sub-satellite system and can be characterized by tension magnitude variations. For the case of lateral tether dynamics, the steady-state behavior of

the tether will approach the lowest natural frequency and mode shape of a vibrating string connected between two fixed end points. This behavior can be characterized by variations of the tether tension magnitude and direction. As a result, the tether dynamics simulator was employed to generate tension magnitude and direction variations of the force applied by the tether to the air-bearing vehicle. Experimental data show that if the tension magnitude variations are less than about 7.5% of the nominal tension value, the measured RMS attitude of the sub-satellite is less than 1 arcsec. Results of additional experiments show that for tension directional variations which correspond to a lateral modal amplitude which is less than about 5% of the tether half-length, the control algorithm can regulate the orientation to less than 1 arcsec RMS.

The complete effect of tether dynamics on the behavior of the tethered satellite attitude control system is the combination of the longitudinal and lateral motions of the tether. Mathematical models and computer simulations of the total tether dynamics show that steady-state tension variations in the orbital case are expected to be less than 5% of the nominal value (which results from the relatively large damping inherent in long, space tethers). Therefore, it can be concluded that the combination of longitudinal tether dynamics and that portion of the lateral dynamics which couples into tension magnitude variations should not effect the ability of the control algorithm to regulate the sub-satellite orientation with an accuracy better than 1 arcsec. Also, computer simulations show that the expected orbital tether behavior in the steady state will be characterized by direction variations which correspond to lateral modal amplitudes which are well under 1% of the tether half-length. Based on these observations, it can be concluded that lateral tether dynamics will not effect the ability of the control algorithm to regulate the vehicle orientation to less than 1 arcsec.

Further, additional experimental data show that, for tension magnitude variations of 5%, less than 1 arcsec orientation regulation can be achieved for disturbance torque levels less than about 1×10^{-3} N-m. On orbit, this roll disturbance torque level will be reached only after 800 orbits so that a momentum wheel desaturation maneuver will need to be initiated approximately every 40 days. In addition, for direction

variations which correspond to modal amplitudes equal to 5% of the tether half-length, roll disturbance torque magnitudes less than about 1×10^{-3} N-m did not degrade performance above about 0.5 arcsec. Once again, in orbit, this level of disturbance torque is generated after about 800 orbits. Hence, limiting the wheel speed after 40 days of flight will ensure that both tether tension and direction variations will have a small enough effect that 1 arcsec accuracy can easily be achieved.

Additional experiments were performed to judge the need for mass center estimation and the effect of tension scaling for the cases with roll disturbance torques and tether tension variations active. Experimental results show that mass center estimation is necessary for arcsec regulation for the following cases: 5% tension magnitude variations in addition to mass center misalignment greater than 3 mm, and 2% tether half-length direction variations coupled with 10 mm misalignment in the mass center. Data from the experiments which tested the effectiveness of tension measurement and feedback show that for magnitude variations, tension feedback can achieve approximately 10% improvement in the steady-state performance, while for direction variations, feedback of tension will yield less than 2.5% improvement in steady-state accuracy. If even better results are desired, an estimator can be designed (in conjunction with a load cell measurement and a measurement of the relative angle between the tether and sub-satellite) to determine the state of the tether. With this additional state information, the effect of tether dynamics can be accounted for in the control algorithm with the aim of achieving better performance. Based on the laboratory experience with tension feedback, it appears that only a relatively small improvement will result. These findings suggest that the added complexity and cost of the modified control algorithm and additional measurement devices are not warranted.

Appendix A

FORTRAN Programs

A.1 Fine Pointing Control Program

```
      integer*2 isamp,ich1,istep
      character name*10,formt*20
      integer img,nrows,ncols,maxt
      double precision data(1100,4),l1,l2,l3,k1,k2,k3,k4,xb1,xb2,xb3
      double precision volts,pos,e,sum
      common /cons/itime,ich1,volts
      common /gains/l1,l2,l3,xb1,xb2,xb3,k1,k2,k3,k4
      common /dat/data,pos,e,sum
      external cloop

C     CONSTANT DEFINITIONS
21    k1= 9.082*39.37*1000.
      k2=20.4182*39.37*1000.
      k3=1.2521*39.37*1000.
      k4=0.3003
      l1=0.5632
      l2=0.4566
      l3=-1.3218
      isamp=500
```

```
      itime=0
      xb1=0.0
      xb2=0.0
      xb3=0.0
      e=0.0
      ich1=1
      volts=20./4096.
      pos=0.0

C     INPUT TIME FOR RUN
      write(*,3)
3     format(5x,'Input max time===>')
      read(*,*) maxt
      maxt=(maxt*1000/isamp)+1

C     INITIALIZE STEPPER MOTOR
      call init

C     USE 80130 TO RUN INTERRUPT DRIVEN CONTROL LOOP
      call clock(isamp,cloop)

C     LOOP UNTIL SPECIFIED TIME HAS ELAPSED
10    continue
      if(itime.ge.maxt) goto 15
      goto 10

C     STOP CLOCK AND RETURN STEPPER MOTOR TO ZERO POSITION
15    call clock(0,cloop)
      istep=nint(-pos*1000)
      call step(istep)
```

```
C     STORE DATA ON DISK
      do 101 i=1,itime
      data(i,1)=data(i,1)
      data(i,2)=3600.*57.3*data(i,2)
      data(i,3)=3600.*57.3*data(i,3)
      data(i,4)=data(i,4)
101   continue
      ncols=4
      nrows=i
      img=0
      name='r'
      formt='(4f15.5)'
      open(4,file=name,status='new')
      write(4,'(a10,3i5,a20)') name,nrows,ncols,img,formt
      write(4,formt) ((data(i,j),i=1,nrows),j=1,ncols)
      close(4)
C
      end


      subroutine cloop
      integer*2 ich1,adcon,iang,nstep,count
      double precision data(1100,4),l1,l2,l3,k1,k2,k3,k4
      double precision xb1,xb2,xb3,xh1,xh2,xh3,yn
      double precision volts,pos,e,un1,t
      common /cons/itime,ich1,volts
      common /gains/l1,l2,l3,xb1,xb2,xb3,k1,k2,k3,k4
      common /dat/data,pos,e


C     TAKE MEASUREMENT AND PERFORM MEASUREMENT UPDATE
      iang=adcon(ich1)
      yn=-.0004*(volts*float(iang)-10.)
      xh1=xb1+l1*(yn-xb1)
```

```
      xh2=xb2+l2*(yn-xb1)
      xh3=xb3+l3*(yn-xb1)


C     CALCULATE CONTROL AND MOVE STEPPER MOTOR
      istep=nint((-k1*xh1-k2*xh2-k3*e+k4*1000.*pos)-1000.*pos)
      if(istep.gt.1000) nstep=1000
      if(istep.lt.-1000) nstep=-1000
      if(istep.lt.1000.and.istep.gt.-1000) nstep=istep
      if(pos.ge.2.5.and.nstep.gt.0) nstep=0
      if(pos.le.-2.5.and.nstep.lt.0) nstep=0
      call step(nstep)


C     SAVE DATA
      un1=pos
      pos=pos+nstep*.001
      itime=itime+1
      data(itime,1)=pos
      data(itime,2)=yn
      data(itime,3)=xb1
      data(itime,4)=xh3


C     PERFORM TIME UPDATE
      xb1=xh1+.5*xh2-.0083*xh3+.0254*(.0041*pos+.0042*un1)
      xb2=xh2-.0333*xh3+.0254*(.0211*pos+.0122*un1)
      xb3=xh3
      e=.5*xh1+e
C
      end
```

A.2 Subroutine For Laboratory Simulator

```
      SUBROUTINE EQNS(T,Y,DY)
      IMPLICIT DOUBLE PRECISION (A-Z)
      DIMENSION Y(6),DY(6)
      COMMON/PLIST/MB,K,L,V1,V2,DV1,DV2,G,I,X,E,BL,BR,BT,DIST
C
C     MB = sub-satellite mass, K = tether spring constant, L = tether length,
C     V1 (V2) = longitudinal (lateral) displacement of tether suspension point,
C     DV1 (DV2) = longitudinal (lateral) velocity of tether suspension point,
C     G = micro-gravity acceleration, I = sub-satellite moment of inertia,
C     X = attach point displacement w.r.t. assumed mass center, E = misalignment
C     between assumed and actual mass center, BL (BR) = linear (rotational)
C     damping coefficient of air-bearing suspension, BT = coefficient of
C     damping for tether, DIST = external disturbance torque


C     Calculate tether forces
      S3=SIN(Y(3))
      C3=COS(Y(3))
      P1=Y(1)-V1-(X+E)*S3
      P2=Y(2)-V2+(X+E)*C3
      MP=SQRT(P1*P1+P2*P2)
      IF (MP.LE.0.000001) MP=0.000001
      DP1=Y(4)-DV1+(X+E)*C3*Y(6)
      DP2=Y(5)-DV2+(X+E)*S3*Y(6)
      FS=K*(L-MP)
      FD=-BT*(P1*DP1+P2*DP2)/MP


C     Calculate Generalized Forces
      F1=MB*G-(B*Y(4))+((FS+FD)*P1/MP)
      F2=-(B*Y(5))+((FS+FD)*P2/MP)
      F3=-(BR*Y(6))-((X+E)*(FS+FD)*(P1*C3+P2*S3)/MP)
```

```
C     Calculate state derivatives
      DY(1)=Y(4)
      DY(2)=Y(5)
      DY(3)=Y(6)
      DY(4)=F1/MB
      DY(5)=F2/MB
      DY(6)=(F3+DIST)/I
      RETURN
      END
```

Bibliography

[1] Bekey, I., "Historical Evolution of Tethers in Space", *Advances in the Astronautical Sciences*, Vol. 62, AAS 86-202, 1986.

[2] Sutton, G.W., and Diederich, F.W., "Synchronous Rotation of a Satellite at Less Than Synchronous Altitude", *AIAA Journal*, Vol. 5, No. 4, 1967.

[3] Bekey, I., "Tethers Open New Space Options", *Astronautics and Aeronautics*, Vol. 21, No. 4, 1983.

[4] Bekey, I., "Space Station Operations Enhancement Using Tethers", IAF-84-43, presented at the 35^{th} Congress of the International Aeronautics Federation, Lausanne, Switzerland, October, 1984.

[5] Lemke, L.G., "A Concept for Attitude Control of a Tethered Astrophysical Observatory Platform", AIAA-85-1942-CP, presented at the AIAA Guidance, Navigation, and Control Conference, Snowmass, Colorado, August, 1985.

[6] Lemke, L.G., Powell, J.D., and He, X., "Attitude Control of Tethered Spacecraft", *The Journal of the Astronautical Sciences*, Vol. 35, No. 1, 1987.

[7] Misra, A.K., and Modi, V.J.,, "A Survey on the Dynamics and Control of Tethered Satellite Systems", *Advances in the Astronautical Sciences*, Vol. 62, AAS 86-246, 1986.

[8] Stuiver, W., "Dynamics and Configuration Control of a Two-Body Satellite System", *Journal of Spacecraft and Rockets*, Vol. 11, No. 8, 1974.

[9] Bainum, P.M., and Kumar, V.K., "Optimal Control of the Shuttle-Tethered System", *Acta Astronautica*, Vol. 7, No. 12, 1980.

[10] Modi, V.J., Chang-Fu, G., Misra, A.K., and Xu, D.M., "On the Control of the Space Shuttle Based Tether System", *Acta Astronautica*, Vol. 9, No. 6-7, 1982.

[11] Modi, V.J., Chang-Fu, G., and Misra, A.K., "Effects of Damping on the Control Dynamics of the Space Shuttle Based Tether System", *Journal of the Astronautical Sciences*, Vol. 31, No. 1, 1983.

[12] Paul, B., "Planar Librations of an Extensible Dumbbell Satellite", *AIAA Journal*, Vol. 1, No. 2, 1963.

[13] Schaechter, H.B., "Planar Librations in Elliptic Orbits", *AIAA Journal*, Vol. 2, No. 6, 1964.

[14] Pringle, R., "Exploration of Nonlinear Resonance in Damping an Elastic Dumb-Bell Satellite", *AIAA Journal*, Vol. 6, No. 7, 1968.

[15] Bainum, P.M., Harkness, R.E., and Stuiver, W., "Attitude Stability and Damping of a Tethered Orbiting Interferometer Satellite System", *The Journal of the Astronautical Sciences*, Vol. 19, No. 5, 1972.

[16] Stuiver, W., and Bainum, P.W., "A Study of Planar Deployment Control and Libration Damping of a Tethered Orbiting Interferometer Satellite", *Journal of Spacecraft and Rockets*, Vol. 20, No, 6, 1973.

[17] Singh, R.B., "Three Dimensional Motion of a System of Two Cable-Connected Satellites in Orbit", *Astronautica Acta*, Vol. 18, No. 5, 1973.

[18] Modi, V.J., and Misra, A.K., "Orbital Perturbations of Tethered Satellite Systems", *The Journal of the Astronautical Sciences*, Vol. 25, No. 3, 1977.

[19] Arnold, D.A., "The Behavior of Long Tethers in Space", *The Journal of the Astronautical Sciences*, Vol. 35, No. 1, 1987.

[20] Fan, D.N., and McGarvey, J.F., "Nonlinear Stress Waves in a Perfectly Flexible String", *The Journal of the Astronautical Sciences*, Vol. 25, No. 1, 1977.

[21] Modi, V.J., and Misra, A.K., "On the Deployment Dynamics of Tether Connected Two-Body Systems", *Acta Astronautica*, Vol. 6, No. 9, 1979.

[22] Bschorr, O., "Controlling Short-Tethered Satellites", *Acta Astronautica*, Vol. 7, No. 4-5, 1980.

[23] Beletskii, V.V., and Levin, E.M., "Dynamics of the Orbital Cable System", *Acta Astronautica*, Vol. 12, No. 5, 1985.

[24] Bainum, P.M., Diarra, C.M., and Kumar, V.K., "Shuttle-Tethered Subsatellite System Stability with a Flexible Massive Tether", *AIAA J. Guidance, Control, and Dynamics*, Vol. 8, No. 2, 1985.

[25] Misra, A.K., and Modi, V.J., "The Influence of Satellite Flexibilty on Orbital Motion", *Celestial Mechanics*, Vol. 17, No. 2, 1978.

[26] Lips, K.W., Modi, V.J., "Transient Attitude Dynamics of Satellites with Deploying Flexible Appendages", *Acta Astronautica*, Vol. 5, No. 10, 1980.

[27] Lips, K.W., and Modi, V.J., "General Dynamics of a Large Class of Flexible Satellite Systems", *Acta Astronautica*, Vol. 7, No. 12, 1980.

[28] Breakwell, J. and Gearhart, J., "Pumping a Tethered Configuration to Boost its Orbit Around an Oblate Planet", *The Journal of the Astronautical Sciences*, Vol. 35, No. 1, 1987.

[29] Bergamaschi, S., "Dynamical Effects of Tether Structural Damping: A Preliminary Model", *Advances in the Astronautical Sciences*, Vol. 62, AAS 86-218, 1986.

[30] He, X., and Powell, J.D., "Tether Damping in Space", *Journal of Guidance, Control and Dynamics*, Vol. 13, No. 1, 1990.

[31] He, X., "Attitude Control of Tethered Satellites", Ph.D. Thesis, Department of Aeronautics and Astronautics, Stanford University, Stanford, California, 1990.

[32] Kane, T.R., and Levinson, D.A., "Deployment of a Cable-Supported Payload from an Orbiting Spacecraft", *Journal of Spacecraft and Rockets*, Vol. 14, No. 7, 1977.

[33] Banerjee, A.K., and Kane, T.R., "Tether Deployment Dynamics", *Journal of the Astronautical Sciences*, Vol. 30, No. 4, 1982.

[34] Boschitsch, A., and Bendiksen, O.O., "Nonlinear Control Laws for Tethered Satellites", *Advances in the Astronautical Sciences*, Vol. 62, AAS 86-219, 1986.

[35] Banerjee, A.K., and Kane, T.R., "Tethered Satellite Retrieval with Thruster Augmented Control", *Journal of Guidance, Control, and Dynamics*, Vol. 7, No. 1, 1984.

[36] Xu, D.M., Misra, A.K., and Modi, V.J., "Thruster Augmented Active Control of a Tethered Sub-Satellite During It's Retrieval", *Journal of Guidance, Control, and Dynamics*, Vol. 9, No. 6, 1986.

[37] Kane, T.R., "A New Method for the Retrieval of the Shuttle-Based Tethered Satellite", *Journal of the Astronautical Sciences*, Vol. 32, No. 3, 1984.

[38] Rupp, C.C., and Laue, J.H., "Shuttle/Tethered Satellite System", *Journal of the Astronautical Sciences*, Vol. 26, No. 1, 1978.

[39] Austin, F., and Bauer, E., "Scaled Dynamic Model of a Free Rotating Cable-Connected Space Station", *Journal of Spacecraft and Rockets*, Vol. 7, No. 10, 1970.

[40] Baracat, W.A., and Butner, C.L., " Tethers in Space Handbook", Submitted to the Office of Space Flight, Advanced Programs, NASA Headquarters, Washington, D.C., 1986.

[41] Penzo, P.A., and Ammann, P.W., "Tethers in Space Handbook, Second Edition", Submitted to the Office of Space Flight, Advanced Programs, NASA Headquarters, Washington, D.C., 1989.

[42] Lemke, L.G., "Attitude Control of Tethered Satellites", Engineers Thesis, Department of Aeronautics and Astronautics, Stanford University, Stanford, California, 1989.

[43] Powell, J.D., Lemke, L.G, and He, X., "Final Report on an Investigation of the Kinetic Isolation Tether Experiment", Submitted to NASA Ames Research Center, NASA Ames University Consortium Interchange No. NCA2-54, Moffett Field, California, 1986.

[44] Powell, J.D., He, X., and Schoder R., "Annual Report of the Kinetic Isolation Tether Experiment", Submitted to NASA Ames Research Center under Grant No. NCC 2-389, Moffett Field, California, 1987.

[45] Stephenson, M.W., "Dynamics and Control of the Space Shuttle-Based Kinetic Isolation Tether Experiment", Master of Science and Engineers Thesis, Department of Aeronautics and Astronautics, The Massachusetts Institute of Technology, Cambridge, Massachusetts, 1988.

[46] Kane, T.R., and Levinson, D.A., *Dynamics: Theory and Applications*, McGraw-Hill Book Company, New York, New York, 1985.

[47] Kane, T.R., Likins, P.W., and Levinson, D.A., *Spacecraft Dynamics*, McGraw-Hill Book Company, New York, New York, 1984.

[48] Rehsteiner, F.H., "Static and Dynamic Properties of Hydrostatic Thrust Gas Bearings with Curved Surfaces", Ph.D. Thesis, Department of Aeronautics and Astronautics, Stanford University, Stanford, California, 1968.

[49] Wertz, J.R., *Spacecraft Attitude Determination and Control*, Reidel Publishing Company, Boston, Massachusetts, 1986.

[50] Franklin, G.F. and Powell, J.D., *Digital Control of Dynamic Systems*, Addison-Wesley Publishing Company, Reading, Massachusetts, 1981.

[51] Bryson, A.E., and Ho, Y.C., *Applied Optimal Control*, Hemisphere Publishing Company, Washington, D.C., 1975.

[52] Powell, J.D., "Mass Center Estimation in Spinning Drag-Free Satellites", *Journal of Spacecraft and Rockets*, Vol. 9, No. 6, 1972.

[53] Majumdar, B.C., "Externally Pressurized Gas Bearings: A Review", *Wear*, vol. 62, 1980, pp. 299-314.

[54] Grassam, N.S., and Powell, J.W., *Gas Lubricated Bearings*, Butterworth and Company, London, England, 1964.

[55] Design Components, Inc., *Positioning Tables*, Design Components Incorporated, Franklin, Massachusetts, 1984.

[56] Sigma Instruments, Inc., *Stepper Motor Selection Guide*, Sigma Motion Control, Braintree, Massachusetts, 1984.

[57] Entran Devices, Inc., *Entran Sensors*, Entran Devices Incorporated, Fairfield, New Jersey, 1987.

[58] Alexander, H.L., "Experiments in Control of Satellite Manipulators", Ph.D. Thesis, Department of Aeronautics and Astronautics, Stanford University, Stanford, California, 1988.

[59] Lorell, K., "Precision Attitude Control of Symmetric Spinning Bodies", Ph.D. Thesis, Department of Aeronautics and Astronautics, Stanford University, Stanford, California, 1971.